

ASSEMBLY OF COLLOIDAL MESOPHASES AND SUBSTITUTIONALLY  
DISORDERED PHASES FOR PHOTONICS

A Dissertation

Presented to the Faculty of the Graduate School

of Cornell University

In Partial Fulfillment of the Requirements for the Degree of

Doctor of Philosophy

by

Kullachate Muangnapoh

August 2017

© 2017 Kullachate Muangnapoh

# ASSEMBLY OF COLLOIDAL MESOPHASES AND SUBSTITUTIONALLY DISORDERED PHASES FOR PHOTONICS

Kullachate Muangnapoh, Pd.D.

Cornell University 2017

Colloidal mesophases are materials that exhibit spontaneous ordering with characteristics between those of crystalline and glassy photonic solids. The study of these partial order *photonic mesophases* is critical to advancing a new paradigm for photonic structures, with large photonic band gap and negative refraction properties that can be realized via low cost self-assembly. It is well known that *photonic crystals* dramatically alter the dispersion relations and the spatial power distribution of electromagnetic modes in dielectric materials with a periodic refractive index. *Photonic glasses* provide control over light diffusion via the optical resonances of building blocks with short-range positional order.

New concepts suggest certain types of disorder support photonic band gap properties. This behavior has been predicted in arrangements whose structure factor  $S(k)$  tends toward zero as  $|k|$  approaches zero including hyperuniform disordered, quasicrystals, and semi-regular tilings. The substitutionally disordered shape-binary phases and single component mesophases, which are the subject of this work, satisfy the structure factor criteria for bandgap formation and their study lies at the frontier of manipulating disorder for colloid-based photonics.

Shape-binary mixtures of spheres and peanut-shaped particles (spheres and cut-spheres) are self-organized into substitutionally disordered phases using wedge-cell confinement. The particles are compatible with lobes sizes within ten percent of each other. Particle shape templates are sacrificed to obtain hollow silica shells. This design minimizes segregation between the two particle shape populations by reducing density mismatch. Using fast confocal microscopy, five distinct phases are found between one and two integral layers for the mixture of spheres and peanut-shaped particles:  $1\Delta$ (hexagonal)  $\rightarrow$   $1\beta$  (buckled)  $\rightarrow$   $2\Box$ (square)  $\rightarrow$   $2\Delta_I$  (hexagonal)  $\rightarrow$   $2\Delta_{II}$  (hexagonal). This sequence is similar to that of single component hard spheres and hard dimers with the addition of major axis orientations for the dimers. For the mixture of spheres and cut-spheres, eight distinct phases are observed:  $1\Delta_r$ (hexagonal)  $\rightarrow$   $1S_I$ (side)  $\rightarrow$   $1S_{II}$  (rotator)  $\rightarrow$   $1B$  (buckled)  $\rightarrow$   $2\Box$  (square)  $\rightarrow$   $2\Delta_r$ (hexagonal)  $\rightarrow$   $2S_I$ (side)  $\rightarrow$   $2S_{II}$  (rotator). The descriptive sequence is similar to that of pure cut-spheres. The substitutional disorder follows from the Hume-Rothery rules for atomic isomorphous phases. Monte Carlo simulations establish the ideal phases and the phase diagram for the pure dimers and shape mixtures.

## BIOGRAPHICAL SKETCH

Kullachate Muangnapoh was born and raised in Bangkok, Thailand. He was always been fascinated by science and math, especially applied to information technology and the environment. During high school, he was a part of a small team that won the Thailand national science contest. He also qualified as top 25 in the nation to attend the mathematics camp sponsored by Thailand's Department of Promotion of Science and Technology. In 2005, Kullachate received the Thai government scholarship to study Material Science in the United States. As an undergraduate student, he majored in Material Science and Engineering at Northwestern University. During that time, he interned in Thailand Center of Material Research for one summer where he worked on materials for dental implants. He also worked in the Barnett lab for two years where he studied the effect of firing temperature on LSM-YSZ composite cathodes. Kullachate graduated in 2010 and continued his studies at Cornell University in the Department of Materials Science and Engineering under supervision of Professor Chekesha M. Liddell Watson. His works focus on the binary self-assembly of anisotropic colloids. Kullachate earned his M.S. degree in 2013, and completed his doctoral work in the summer of 2017.

To my family

## ACKNOWLEDGMENTS

I would like to acknowledge the many people who have had a great impact on my development. First, I would like to thank my family for all of their support. At Cornell University, I would like to thank Dr. Chekesha Liddell Watson for her support and encouragement during my years here. I would also want to thank my committee members, Prof. Fernando Escobedo and Prof. Giannelis for their assistance in reaching this goal. Many thanks to members of Liddell Watson group who are always willing to help with ideas and have been great friends in the lab. To my collaborators for their ideas, discussions, lab equipment and help with publications. Additional thanks to the research funding agencies; the National Science Foundation and the Department of Energy for making this research possible. Additional thanks to the staff of NBTC, CCMR and the Material Science and Engineering for their prompt assistance with the equipment. Finally, I would like to thank my friends who play sports, travel and keep me focused on my work. Each of you have helped shaped me into the person I am today.

## TABLE OF CONTENTS

Biographical Sketch.....	iii
Dedication.....	iv
Acknowledgements.....	v
Table of Contents .....	vi
List of Tables .....	viii
List of Figures .....	ix
1. Introduction .....	1
References .....	8
2. Degenerate Crystals From Colloidal Dimers Under Confinement .....	12
2.1 Abstract .....	12
2.2 Introduction .....	13
2.3 Experimental Section.....	15
2.3.1 Synthesis .....	15
2.3.2 Sample preparation .....	16
2.3.3 MC simulations .....	17
2.4 Results and Discussion .....	18
2.5 Conclusion .....	33
Reference .....	34
3. Substitutionally Disordered Phases from Binary Shape Colloids Under Confinement .....	40
3.1 Abstract .....	40
3.2 Introduction .....	41
3.3 Experimental Method .....	43
3.3.1 Anisotropic particle synthesis .....	43
3.3.2 Spherical particle synthesis .....	45
3.3.3 Shape-binary assembly .....	46
3.3.4 Structure analysis .....	47
3.3.5 Monte Carlo simulation .....	47
3.4 Results and discussion .....	49
3.5 Conclusion .....	65
References .....	67
4. Substitutionally Disordered Phases From Binary Sphere And Cut-Sphere Mixtures Under Confinement .....	72
4.1 Abstract .....	72
4.2 Introduction .....	74
4.3 Method.....	77
4.3.1 Particle synthesis .....	77
4.3.2 Deposition of rhodamine-dyed hollow silica shells .....	79
4.3.3 Particle assembly .....	80

4.3.4	Photonic simulation .....	80
4.4	Results and discussion .....	81
4.5	Conclusion .....	95
References	.....	97

## LIST OF FIGURES

1.1	Schematic of wedge- confinement cell .....	7
2.1	Self-assembly of peanut particles with increasing gap size in confinement wedge cell .....	19
2.2	Histograms of dimer particle orientations from confocal microscopy experiments .....	22
2.3	Monte Carlo simulation results for the equation of state (EoS) for hard dimers under confinements .....	24
2.4	Lobe pair correlation functions, $g(r)$ , for monolayer and bilayer degenerate crystals .....	26
2.5	Voronoi construction in the x-y plane for the experimental structures ....	27
2.6	$H^*-\phi$ phase diagram of hard dimers (symmetric-lobed) under confinement obtained from Monte Carlo simulations .....	28
2.7	Representative configurations of the stable phases observed in the phase diagram of hard dimers .....	31
3.1	Confocal images for the binary self-assembly of spheres and peanuts in confinement cells .....	51
3.2	Monte Carlo simulation results for the equation of state (EoS) for hard peanuts and spheres confined between parallel hard walls at a distance of $H/\sigma$ .....	56
3.3	Lobe-based pair distribution functions, $g(r)$ , for shape-binary structures ..	57
3.4	Simulated Voronoi constructions for the binary system of hard peanuts and spheres .....	58
3.5	Voronoi constructions for the shape-binary structures .....	59
3.6	$H^*-\phi$ Phase diagram of binary hard peanuts and sphere from Monte Carlo simulations .....	60

3.7	Representative areas of stable phase configurations observed in the phase diagram for the binary system of hard peanuts and spheres .....	61
3.8	Simulated structure factors for the binary system of peanuts and spheres	63
3.9	$H^*$ - $\phi$ Phase diagram of binary hard peanuts and sphere from Monte Carlo simulations .....	64
4.1	Transverse magnetic (TM) photonic bandgaps in systems of random binary mixtures of circular rods and cut-rods decorating a hexagonal lattice .....	77
4.2	Scanning Electron Microscopy images of cut-spheres cores prepared by using dynamic controls in seeded emulsion polymerization .....	81
4.3	Confocal Microscopy images for the binary self-assembly of spheres and cut-spheres in confinement cells .....	84
4.4	Fast Fourier Transforms (FFTs) and autocorrelation images showing the symmetry of the binary phases .....	88
4.5	Pair Distribution Functions for shape-binary phases indicating the correlation distance of positional order .....	89
4.6	Voronoi constructions for shape-binary phases of spheres and cut-spheres	90
4.7	Hexagonal bond orientational order parameter as a function of composition for the side monolayer phase $1S_1$ .....	91
4.8	Confocal images for binary phases of spheres and cut-spheres with larger size mismatch .....	93
4.9	Voronoi constructions for shape-binary phases of spheres and cut-spheres with larger size mismatch .....	95

## LIST OF TABLES

2.1	Bond orientational order parameters for experimental phases .....	25
3.1	Lobe-based order parameters for experimental shape-binary phase .....	53
4.1	Shape-binary phase composition and bond-orientational order parameters .....	83
4.2	Shape-binary phase composition and bond-orientational order parameters .....	94



## CHAPTER 1

### Introduction

Photonic crystals (photonic band gap materials) offer an unprecedented control of light by dramatically altering the dispersion relations and the spatial power distribution of electromagnetic modes within dielectric materials.<sup>1</sup> Visible and Infrared (IR) photonic crystals are materials whose refractive index varies periodically on the length scale from 450 nm to 2 microns such that the crystal accepts or rejects light transmission according to the frequency and direction of the light. Based on these features, enhanced electrooptic properties have been demonstrated including photonic band gaps<sup>1</sup>, inhibition of spontaneous emission, light localization,<sup>2</sup> negative refraction,<sup>3-4</sup> self-collimation<sup>5</sup> and slow light (i.e., vanishingly low group velocity).<sup>6</sup> These material properties lead to a host of novel applications including low loss waveguiding<sup>3,7</sup>, low threshold lasing,<sup>8-9</sup> coherent LED emission<sup>10</sup>, superprism effects<sup>11</sup>, super lenses (sub-diffraction limit planar lenses)<sup>12</sup>, photovoltaics,<sup>13-14</sup> etc.

The periodic structures required for photonic band gap behavior are quite difficult to fabricate at the nano- and micrometer length scales necessary because several design parameters need to be optimized. Calculations of the optical properties of photonic crystals has revealed that the favorable characteristics include a submicron lattice constant, high refractive index contrast between dielectric materials and low volume filling fraction of high index material.<sup>15</sup> The standard processing approaches include expensive and time-consuming serial

writing of features by electron beam lithography, direct laser writing, and micromachining by focused ion beam milling. The latter is not versatile for arbitrary design geometry, though it can be fast. Interference lithography (holography) and nanoimprint lithography have been demonstrated for large area, parallel processing of patterns. Registry of functional layers upon stacking into a third dimension reduces throughput and remains a significant issue for the methods.<sup>16</sup>

Relative to lithographic approaches, colloid-based solutions for the fabrication challenge are highly attractive due to the low cost, large area, parallel processing and ease of building up to three dimensions. Spherical colloids are commercially available and are the most common motifs for colloidal assembly. The assemblies are infiltrated with high refractive index material and etched to remove the original sphere template. This process produces structures with inverse face-centered cubic (FCC) morphology that exhibit a complete photonic band gap between the eighth and ninth photonic bands when the refractive index contrast is greater than 2.7-2.8.<sup>17</sup> However, variations in the radii of spheres or random displacements from lattice sites which occur during self-assembly, can greatly reduce the band gap size for these high frequency bands. The direct FCC structure does not support a complete band gap because of symmetry induced degeneracy at points of high symmetry.<sup>10</sup> These degeneracies can be lifted in structures with complex bases (i.e, more than one 'atom' per unit cell and/or shape-anisotropic 'atoms').<sup>10</sup> Anisotropic particle shapes have been prepared in recent years using synthetic methods and microfabrication including

boomerangs,<sup>18</sup> blood cell shapes,<sup>19</sup> ellipsoids<sup>20-21</sup>, rods,<sup>22</sup> polygons,<sup>23</sup> gear-shapes,<sup>24</sup> etc. The self-organization of such colloidal building blocks can be performed using electric-field (dipolar and dielectrophoretic forces); shear ordering (shear forces), evaporation-induced assembly (capillary forces), spin coating (centripetal forces), etc.<sup>25</sup> In the former approaches, removing the external field destroys the particle organization, while for the latter techniques care must be taken to prevent meniscus dewetting and incomplete films.<sup>26</sup>

For spheres interacting through a hard potential, crystallization occurs from the colloidal liquid to the hexagonal closed-packed(HCP), random hexagonal closed-packed (RHCP) or face-centered cubic (FCC) lattices in the volume fraction range from 0.494-0.545.<sup>27-28</sup> Monte Carlo simulations on hard space-filling polyhedra<sup>29</sup> have shown that translational and orientational excluded volume fields can also lead to purely entropy-driven assembly, but with richer phase behavior. A range of crystallographic groups and mesophases were predicted to form spontaneously at high and moderate volume fractions, respectively. The combination of high rotational symmetry with low particle anisotropy favors rotator solids. Intermediate particle anisotropy favors liquid crystals that are orientationally ordered (i.e., cubatic and smectic). In addition, sphere-derivatives have shown order-order phase transitions in simulations leading to columnar phases<sup>27-28</sup> for bowl-shapes (i.e., solid of revolution for a crescent); smectic and rotator phases for spherocylinders at low aspect ratios;<sup>30</sup> rotator and degenerate crystal phases for dimers.<sup>31-32</sup> In degenerate crystals (DCs), the centers of the individual dimer lobes lie on a lattice, but the center of mass and orientations of

the dimers lack periodicity.<sup>33-37</sup> Other novel phases have been found such as parquet for tetragonal parallelepipeds at aspect ratios, 0.54-3.2<sup>38</sup> where the particles arrange in perpendicular stacks with their axes aligned along three common directors.

Recently, new concepts have emerged that suggest certain types of structural disorder support photonic band gap properties. This behavior has been predicted in arrangements whose structure factor  $S(\mathbf{k})$  tends toward zero as  $|\mathbf{k}|$  approaches zero including continuous random networks,<sup>39</sup> hyperuniform disordered,<sup>40-41</sup> icosahedral quasicrystals,<sup>42</sup> and rotator mesophases.<sup>43</sup> The substitutionally disordered shape-binary phases and single component DCs, which are the subject of the current work, satisfy the structure factor criteria for bandgap formation and their study lies at the frontier of manipulating disorder for colloid-based photonics.

In this dissertation, we seek strategies to extend the concepts that create complex materials at the atomic (molecular) scale to the assembly of objects at the submicron and micron scales. Essential to this idea is the ability to impart specific assembly instructions to the colloidal building blocks so that materials with enhanced functional properties can be made. The approach herein involves increasing the complexity of the colloidal systems by introducing symmetry-breaking features in the particle shape and by using binary mixtures of particle shapes. The self-organization of these building blocks is performed using the confinement-assisted assembly method. When particle suspensions are confined

between hard plates having spacing incommensurate with that of bulk layers, particles form intermediate structures not found in the bulk.

Chapter 2 describes the self-assembly of degenerate crystals from peanut-shaped particles using confinement-assisted assembly (figure 1.1). Using fast confocal microscopy, five distinct phases were observed as a function of gap height in descriptive sequence  $1\Delta$  (hexagonal)  $\rightarrow$   $1B$  (buckled)  $\rightarrow$   $2\Box$  (square)  $\rightarrow$   $2\Delta_I$  (hexagonal)  $\rightarrow$   $2\Delta_{II}$  (hexagonal), with respect to the dimer lobes. The bilayer hexagonal states are distinguished based on the degree of out-of-plane tilt of the dimer bond i.e., in the  $2\Delta_I$  phase, dimers lie predominantly out-of-plane and transition to in plane orientation for the  $2\Delta_{II}$  phase. These structures can be predicted from closest packing arguments at each gap height. Monte Carlo (MC) simulations are used to prepare phase diagrams and for comparison with ideal structural characteristics.

Chapter 3 describes the self-assembly of shape-binary mixtures of spheres and peanut-shaped into substitutionally disordered phases using wedge-cell confinement. The particles are compatible with lobes sizes within ten percent of each other. Particle shape templates with core-shell morphology are sacrificed to obtain hollow silica shells. This design minimizes segregation between the two particle shape populations by reducing density mismatch. The five distinct phases found between one and two integral layers are similar to that of the single component hard dimer and hard spheres. The assemblies show substitutional disorder on the lattices and degeneracy in the dimer orientation. Monte Carlo

simulations establish the ideal phases and the phase diagram for the shape mixtures.

Chapter 4 describes the self-assembly of shape-binary mixtures of lattice-compatible spheres and cut-spheres into substitutionally disordered phases using wedge-cell confinement. The studies are motivated by our recent photonic band calculations for sphere and cut sphere motifs, which show isotropic photonic band gaps for rotator phases with substitutional disorder. Using fast confocal microscopy, eight distinct phases are found  $1\Delta_r$  (hexagonal)  $\rightarrow 1S_I$  (side)  $\rightarrow 1S_{II}$  (rotator)  $\rightarrow 1B$  (buckled)  $\rightarrow 2\Box$  (square)  $\rightarrow 2\Delta_r$  (hexagonal)  $\rightarrow 2S_I$  (side)  $\rightarrow 2S_{II}$  (rotator). The descriptive sequence is similar to that of pure cut-spheres with the addition of substitutional disorder on the lattices.

The substitutional disorder of the shape-binary phases discussed in Chapters 3-4 follows from the Hume-Rothery rules for atomic isomorphous phases (solid solutions). Namely, the size mismatch between the shape populations is less than 15%, the particle interactions are similar, and spheres and cut spheres (spheres and peanut-shaped particles) tile many of the same phases with gap height.

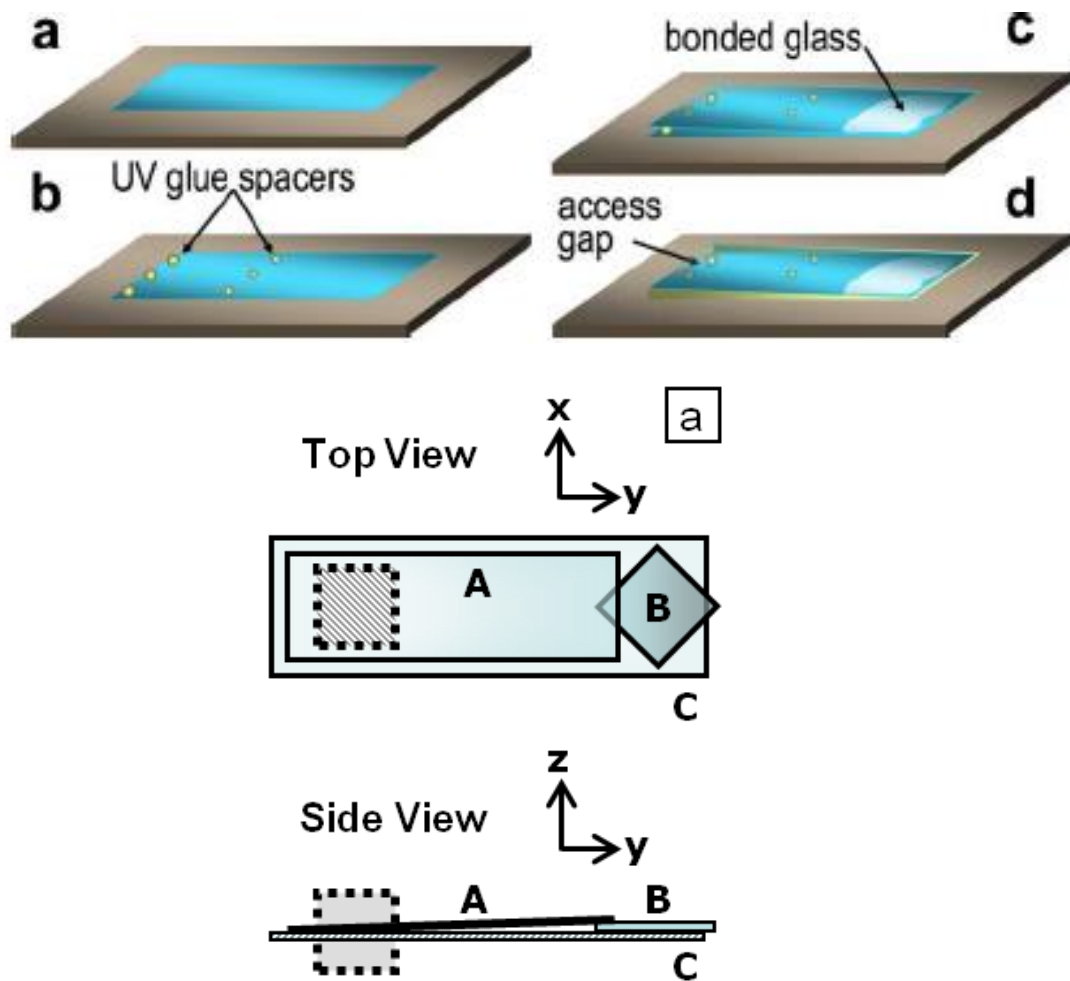


**Figure 1.1** Schematic of wedge- confinement cell

## REFERENCES

1. R. D. Joannopoulos, John D., Johnson, Stephen G., Winn, Joshua N., Meade, Molding the Flow of Light, Princeton University Press, 2008.
2. S. Fan, J. D. Joannopoulos, J. N. Winn, A. Devenyi, J. C. Chen, R. D. Meade, J. *Opt. Soc. Am. B*, 1995, **12**, 1267.
3. E. Cubukcu, K. Aydin, E. Ozbay, S. Foteinopoulou, and C. M. Soukoulis. *Nature*, 2003, **423**, 604.
4. C. M. Soukoulis, M. Kafesaki, and E. N. Economou. *Adv. Mater.*, 2006, **18**, 1941.
5. H. Kosaka, T. Kawashima, A. Tomita, M. Notomi, T. Tamamura, T. Sato, and S. Kawakami. *Appl. Phys. Lett.*, 1999, **74**, 1212.
6. T. F. Krauss, *J. Phys. D. Appl. Phys.* 2007, **40**, 2666.
7. R. R. N. Simons, Coplanar Waveguide Circuits, Components, and Systems, 2001.
8. T. F. Krauss, and R. M. De la Rue, *Prog. Quant. Electron.* 1999, **23**, 51.
9. H. Hirayama, T. Hamano, and Y. Aoyagi, *Appl. Phys. Lett.* 1996, **69**, 791.
10. M. Boroditsky, T. F. Krauss, R. Coccioli, R. Vrijen, R. Bhat, and E. Yablonovitch, *Appl. Phys. Lett.* 1999, **75**, 1036.
11. J. J. Baumberg, N. M. B. Perney, M. C. Netti, M. D. C. Charlton, M. Zoorob, and G. J. Parker, *Appl. Phys. Lett.*, 2004, **85**, 354.
12. R. Moussa, S. Foteinopoulou, L. Zhang, G. Tuttle, K. Guven, E. Ozbay, and C. M. Soukoulis, *Phys. Rev. B - Condens. Matter Mater. Phys.*, 2005, **71**, 1.

13. S. B. Mallick, P. S. Nicholas, M. Agrawal, J. Y. Lee, and P. Peumans. *MRS Bull.*, 2011, **36**, 453.
14. K. A. Arpin, A. Mihi, H. T. Johnson, A. J. Baca, J. A. Rogers, J. A. Lewis, and P. V. Braun. *Adv. Mater.*, 2010, **22**, 1084.
15. C. López, *Adv. Mater.*, 2003, **15**, 1679.
16. A. Boltasseva, Fabrication of Optical Metamaterials, Fabrication of Optical Metamaterials, Chapter 3 in *Tutorials in Metamaterials* by M. A. Noginov and V. A. Podolskiy (Eds.) CRC Press: Taylor and Francis, 2010
17. A. Blanco, E. Chomski, S. Grabtchak, M. Ibisate, S. John, S. W. Leonard, C. Lopez, F. Meseguer, H. Miguez, J. P. Mondia, and G. A. Ozin, *Nature*, 2000, **405**, 437.
18. K. P. Herlihy, J. Nunes, and J. M. Desimone. *Langmuir* 2008, **24**, 8421.
19. M. Okubo, H. Minami, and K. Morikawa, *Colloid Polym. Sci.* 2001, **279**, 931.
20. K. M. Ho, C. T. Chan, and Costas M. Soukoulis. *Phys. Rev. Lett.*, 1990, **65**, 3152.
21. A. C. Stelson, C. Avendano, and C. M. L. Watson. *J. Appl. Phys.*, 2016, **119**, 023110.
22. A. Kuijk, T. Troppenz, L. Fillion, A. Imhof, R. Van Roij, M. Dijkstra, and A. Van Blaaderen, *Soft Matter*, 2014, **10**, 6249.
23. K. Zhao, and T. G. Mason. *Phys. Rev. Lett.*, 2009, **103**, 208302.
24. S. J. Penterman, A. Singh, W. R. Zipfel, and C. M. L. Watson, *Adv. Opt. Mater.*, 2014, **2**, 1024.

25. G. von Freymann, V. Kitaev, B. V. Lotsch, and G. A. Ozin, *Chem. Soc. Rev.*, 2013, **42**, 2528.
26. I. D. Hosein, B. S. John, S. H. Lee, F. A. Escobedo, and C. M. Liddell, *J. Mater. Chem.*, 2009, **19**, 344.
27. P. N. Pusey, and W. van Megan, *Nature*, 1986, **320**, 340.
28. M. Marechal, and M. Dijkstra, *Phys. Rev. E*, 2010, **82**, 031405-1.
29. U. Agarwal, and F. A. Escobedo, *Nature Mater.*, 2011, **10**, 230.
30. P. Bolhuis, and D. Frenkel, *J. Chem. Phys.*, 1997, **106**, 666.
31. M. Marechal, and M. Dijkstra, *Phys. Rev. E*, 2008, **77**, 061405-1.
32. K. W. Wojciechowski, *Phys. Lett. A*, 1987, **122**, 377.
33. S. J. Gerbode, S. H. Lee, C. M. Liddell, I. Cohen, *Phys. Rev. Lett.*, 2008, **101**, 058302-1.
34. S. H. Lee, E. Y. Fung, E. K. Riley, C. M. Liddell, *Langmuir*, 2009, **25**, 7193.
35. K. W. Wojciechowski, *Phys. Rev. B*, 1992, **46**, 26.
36. K. W. Wojciechowski, D. Frenkel, A. C. Branka, *Phys. Rev. Lett.*, 1991, **122**, 3168.
37. M. Kowalik, K. W. Wojciechowski, *J. Non-Cryst. Solids*, 2006, **352**, 4269.
38. B. S. John, C. Juhlin, F. A. Escobedo, *J. Chem. Phys.*, **2008**, *128*, 044909-1.
39. K. Edagawa, S. Kanoko, and M. Notomi, *Phys. Rev. Lett.*, 2008, **100**, 013901.

40. W. Man, M. Florescu, E. P. Williamson, Y. He, S. R. Hashemizad, B. Y. C. Leung, D. R. Liner, S. Torquato, P. M. Chaikin, P. J. Steinhardt, *Proc. Natl. Acad. Sci.* 2013, **110**, 15886.
41. W. Man, M. Florescu, K. Matsuyama, P. Yadak, G. Nahal, S. Hashemizad, E. Williamson, P. Steinhardt, S. Torquato, P. Chaikin, *Opt. Express* 2013, **21**, 19972.
42. A. C. Stelson, C. Avendano, C. M. Liddell Watson, *J. Appl. Phys.* 2016, **119**, 23110.
43. M. Marechal and M. Dijkstra, *Phys. Rev E*, 2008, **77**, 061405.

## CHAPTER 2

### Degenerate crystals from colloidal dimers under confinement

#### 2.1 Abstract

Colloidal aperiodic phases (*i.e.*, entropy stabilized degenerate crystals, DCs) are realized *via* self-assembly of hollow fluorescent silica dimers under wedge-cell confinement. The dimer building blocks approximate two tangent spheres and their arrangements are studied *via* laser scanning confocal microscopy. In the DCs, the individual lobes tile a lattice and five distinct DC arrangements with square, triangular or rectangular layer symmetry are determined as a function of confinement height. Moreover, Monte Carlo simulations are used to construct the phase diagram for DCs up to two layer confinements and to analyze structural order in detail. Just as for spheres, the DC structural transitions under confinement are attributed to the ability or frustration to accommodate an integral number of particle layers between hard walls. Unlike spheres, dimers can also experience transitions involving changes in orientation. DCs are among the unconventional structures (*e.g.*, semi-regular tilings, quasicrystals, plastic crystals) expected to enhance the properties of photonic solids.

---

\*Reproduced with permission from: Muangnapoh, K., Avendaño, C., Escobedo, F. A. and Watson, C. M. L., "Degenerate crystals from colloidal dimers under confinement." *Soft matter* 10, no. 48 (2014): 9729-9738. Copyright 2014 Royal Society of Chemistry.

## 2.2 Introduction

Self-assembly strategies in supramolecular chemistry have been actively pursued to build materials through the ‘programmable’ organization of objects at the submicron and micron scales.<sup>1</sup> In particular, particle shaping and interparticle interactions defined by surface or volume functionality have spurred progress towards complex crystallographic arrangements and mesophases from relatively simple building blocks.<sup>2-8</sup> Such colloidal films may be applied towards the challenge of creating diverse structures for photonic slabs that control light in plane through a modulated refractive index pattern and out-of-plane by index guiding. Symmetry reduction strategies have been suggested to manipulate dispersion relations, lifting the degeneracy of photonic bands (*i.e.*, full photonic band gaps in the guided modes) and promoting frequency regimes with all angle negative refraction.

With regard to the processing science that underlies film formation, confinement- or interface directed assembly has a rich history for a range of materials including films of diblock copolymers (BCPs), low molecular weight molecules and colloidal particles. For example, confining geometry that is incommensurate with the bulk domain spacing dramatically expands the induced morphologies of BCPs.<sup>9,10</sup> As well, two-dimensional (2D) surface physisorbed layers of diatomic molecules undergo phase transitions as a function of coverage or area fraction from registered square to non-registered hexagonal and centered-rectangular (or centered-parallelogram) symmetric arrangements (*e.g.*, CO on Ni<sup>11</sup>). Striking high pressure crystal to aperiodic crystal transitions (*e.g.*, in I<sub>2</sub> (ref. 12)) have been rationalized from 2D molecular simulations for dimers of tangentially bonded hard spheres. At high densities, dimers

form a stable solid structure, in which the centers of the individual dimer lobes lie on a triangular lattice, but the center of mass and orientations of the dimers lack a regular repeating pattern. The free energy of this aperiodic solid is similar to that for the traditional crystalline solids, however, the entropy of the ground state is much larger due to the highly degenerate arrangements of the dimer bond.<sup>13-15</sup>

For colloids, geometric confinement investigations have roots in the observations of a simple sequence of crystal structures formed for spherical polystyrene particle suspensions between repulsive surfaces in wedge geometry.<sup>16</sup> The confinement causes colloidal fluid–solid phase changes in the cell gap for thermodynamic state points that predict a fluid in the bulk.<sup>17</sup> The progression of triangular (*i.e.*, hexagonal) and square symmetric arrangements determined as a function of gap height is represented as  $1\Delta \rightarrow 2\square \rightarrow 2\Delta \rightarrow 3\square \rightarrow \dots \rightarrow n\Delta \rightarrow (n+1)\square \rightarrow (n+1)\Delta$ , where  $n$  is the number of layers in the colloidal thin film.<sup>16,18-21</sup> However, the transitions between  $\Delta$  and  $\square$  layers can occur semi-continuously through the formation of intermediate solid structures such as buckled (B), rhombic (R) and prismatic phases.<sup>17,20,21</sup> In the case of the transformation  $1\Delta \rightarrow 2\square$ , colloidal crystals with rectangular buckled structure grow as in-plane rows in the  $1\Delta$  lattice are promoted and depressed alternately out-of-plane.<sup>19,22</sup>

In this work, wedge-cell confinement<sup>23,27,28</sup> was employed to study the spontaneous organization of peanut-shaped colloidal dimers as a function of confinement height using fast confocal microscopy and video-image analysis. Five distinct phases were discovered in the range from one to two layers. Specifically, each configuration is a degenerate crystal tiling of the corresponding sphere structure

along the descriptive order sequence  $1\Delta \rightarrow 1B \rightarrow 2\Box \rightarrow 2\Delta_I \rightarrow 2\Delta_{II}$ , with respect to the dimer lobes. Distinct  $2\Delta$  states were identified based on the degree of out-of-plane tilt of the dimer bond. Peanut-shaped dimers, oriented predominantly out-of-plane in the  $2\Delta_I$  phase, transition to bilayers of in-plane lying dimers for the  $2\Delta_{II}$  phase. These arrangements can be predicted from closest packing arguments for incommensurate layer heights and are in agreement with our predictions from Monte Carlo (MC) simulations of hard-dimers under confinement.

## 2.3 Experimental Section

### 2.3.1 Synthesis

The  $\alpha$ - $\text{Fe}_2\text{O}_3$  particles were synthesized using a gel-sol method (*i.e.*, goethite gel to hematite sol).<sup>45</sup> A 45 mL NaOH solution (5.625 M) was added to 50 mL  $\text{FeCl}_3$  solution (2 M, pre-filtered, Fisher) under vigorous magnetic stirring in a 100 mL bottle (G-45, VWR) for 5 min. A 5 mL  $\text{Na}_2\text{SO}_4$  solution (0.6 M) was mixed in and the bottle was agitated for 10 minutes. The solution was aged at 100 °C for 8 days in a pre-heated oven. Particles were recovered through vacuum filtration after at least three washing cycles of centrifugation and redispersion in DI water (18.2 M $\Omega$  cm, Millipore Direct-Q 3UV). Samples were dried overnight.

The particles were coated with rhodamine isothiocyanate (RITC) labeled silica using a sol-gel process.  $\alpha$ - $\text{Fe}_2\text{O}_3$  powder (0.5 g) was mixed with 4 mL deionized water and 12 mL of ammonia solution [27% (w/w), Mallinckrodt] in 104 mL of isopropyl alcohol medium. The process was done in a 100 mL round bottom flask placed in a dynalene bath at 30 °C under sonochemical conditions (immersion probe power 14 W, Sonics & Materials Inc.). Aliquots of sol-gel precursor—60  $\mu\text{L}$  of rhodamine dye

solution [1 mL ethanol, 90  $\mu$ L 3-(aminopropyl) triethoxysilane (Aldrich), 25 mg RITC powder (Sigma)] and 100  $\mu$ L of tetraethylorthosilicate (TEOS, Sigma-Aldrich)—were injected every two hours over two addition cycles. The particles were washed three times in isopropyl alcohol. To deposit an outer non-fluorescent silica layer, particles were added to deionized water, ammonia solution, and isopropyl alcohol in the quantities given above and underwent the sonochemical reaction with a single dose of 100  $\mu$ L TEOS for 2 h. The coated particles were washed in isopropyl alcohol twice and in DI water once.

The cores were removed with hydrochloric acid (18% in water, Sigma-Aldrich) at 45 °C for 2.5 hours. The hollow particles were washed in deionized water three times and redispersed into  $2.75 \times 10^{-6}$  M polyvinylpyrrolidone (PVP, MW 40 000; Sigma-Aldrich) aqueous solution.

### **2.3.2 Sample preparation**

Confinement cells were made using 22 mm  $\times$  50 mm coverslips with 2 in.  $\times$  3 in. microscope slides to provide mechanical support. Coverslips were cleaned in aqueous NaOH solution of pH 14 for at least 15 minutes and thoroughly washed in DI water. A coverslip was glued to the microscope slide with Norland UV adhesive. Two rows of spacer dots (cured UV adhesive) were deposited at the top and middle of the supported coverslip and another coverslip was overlaid. Pressure was applied by hand to create a zero height separation edge. This edge and two sides of the cell were sealed with UV adhesive, leaving an edge open for particle injection. The cell was primed with aqueous 50  $\mu$ L PVP solution ( $2.75 \times 10^{-6}$  M) to prevent particles from sticking. The water was evaporated in a vacuum oven (Sheldon Manufacturing, Model

1400E) at room temperature. Particle suspension was injected into the cell and the top edge was sealed with UV adhesive. Crystallization in the 2D and quasi 2D regions was examined using the Zeiss LSM 5 LIVE confocal microscope with 532 nm laser line excitation.

### 2.3.3 MC simulations

Crystal structures for each value of  $H^*$  were calculated using the method in ref. 46, which has proven to be an efficient method to predict crystalline solid structures for a large variety of systems. We found that systems comprised of  $N = 8$  and 10 particles were suitable to obtain reliable crystal structures. For each value of  $H^*$  an initial low-density configuration was generated at random. The fully isotropic system was first equilibrated at pressure  $P_t^* = 1$  using MC simulation in the  $NP_tT$  ensemble allowing the shape of the box to change, using the lattice reduction technique to prevent extreme distortions of the simulation box. The pressure was increased in steps of  $\Delta P_t^* = 1$  to the value  $P_t^* = 10$  and further increased by a factor of 10 up to the value of  $P_t^* = 10^6$ . The final configuration was expanded again down to the pressure  $P_t^* = 1$ . We performed 100 such cycles, and the final configuration in each cycle was saved for post-processing analysis. From the set of 100 final configurations, we chose those with highest density as the ‘perfect’ lattices to be used as the starting configurations for the next stage.

The equation of state (EoS) was obtained by performing expansion runs on the ‘perfect’ lattices beginning at a pressure  $P_t^* = 1000$  and expanding, sequentially, down to  $P_t^* = 0.5$ . For each system, approximately 200 particles per layer were used and  $5 \times 10^5$  MC cycles were performed for equilibration with an additional  $1 \times 10^6$  MC cycles

for collecting ensemble averages. The MC cycle is a collection of  $N$  moves that includes standard particle translations, rotations, and volume changes (calibrated to attain a 30–40% acceptance probability). A cluster move scheme (ESI Fig. 1) was also implemented similar to the one reported in ref. 13 to allow for fast reorientation of dimer bonds;  $N$  cluster moves were attempted every 20 MC standard cycles.

## 2.4 Results and Discussion

The anisotropic particle shape of the hollow silica shells and the fit with the hard symmetric-lobed dimer model is shown in Fig. 2.1. The average particle dimensions, as determined from measurements of at least 50 particles in scanning electron microscopy (SEM) images, were 2.09  $\mu\text{m}$  in lobe diameter and 3.76  $\mu\text{m}$  in length with the corresponding coefficients of variation (standard deviation divided by mean), 4.4% and 2.2%, respectively. Monodisperse sacrificial peanut-shaped hematite ( $\alpha\text{-Fe}_2\text{O}_3$ ) colloids were prepared from ferric chloride *via* ferric oxyhydroxide gel-sol synthesis. The external morphology of the particles is a result of an aggregation growth from acicular antiferromagnetic nanocrystals with preferred orientation parallel to the crystallographic  $c$ -axis in the hexagonal system. Silica and rhodamine functionalized-silica layers were deposited using base-catalyzed hydrolysis and condensation of alkoxide under sonochemical conditions. We dissolved the hematite cores because they support dipolar particle interactions and the focus for the present study is on competing entropic driving forces. The shell thickness of 110 nm was determined from the contrast of hollow particles in transmission electron microscopy (TEM) images. The colloidal dimers were sterically stabilized in amphiphilic polymer aqueous solution to ensure nearly hard body interactions.<sup>23–26</sup>

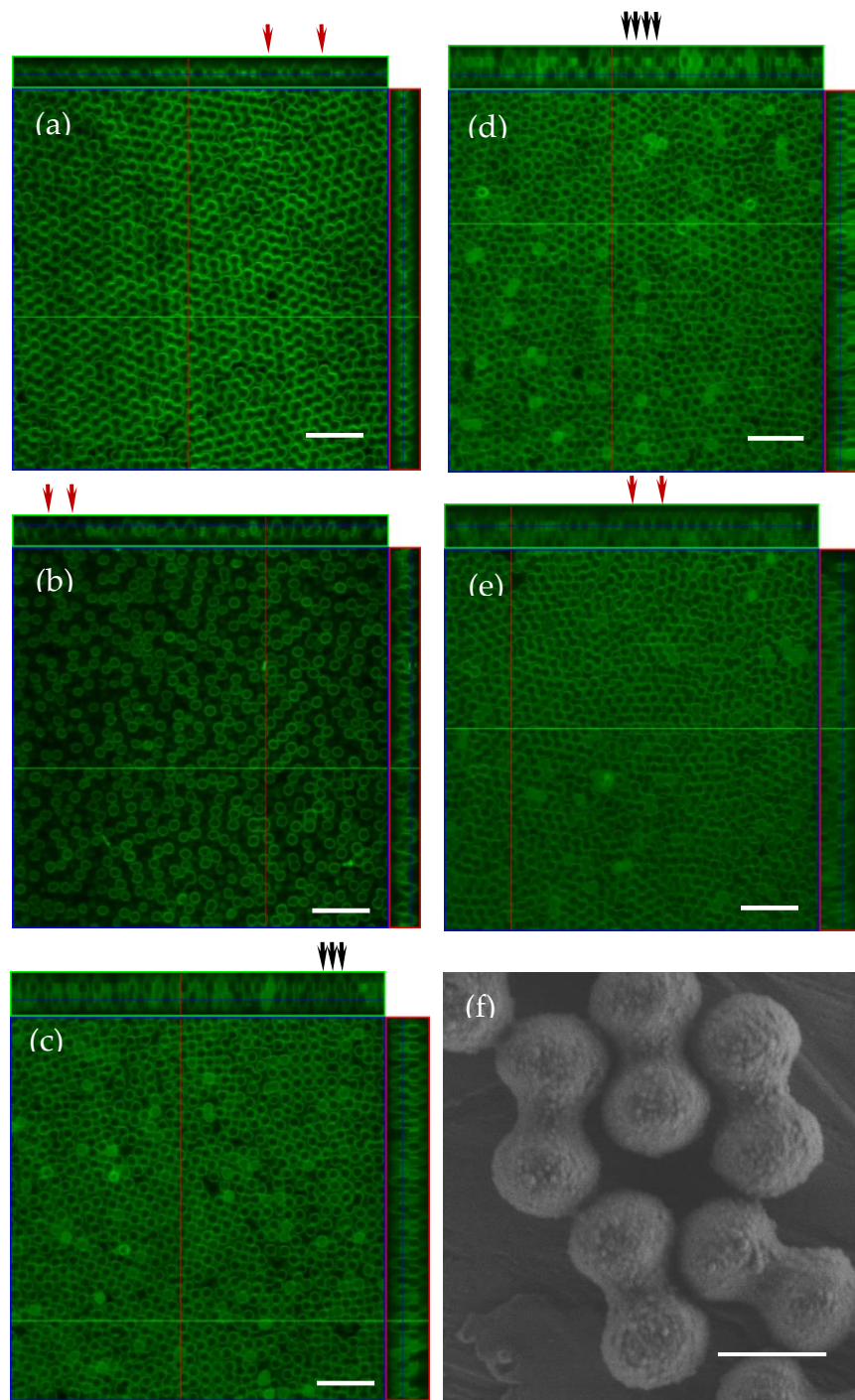


**Figure 2.1.** Self-assembly of peanut particles with increasing gap size in confinement wedge cell. Confocal microscopy images of degenerate crystal (a) hexagonal monolayer ( $1\Delta$ ), (b) buckled state ( $1B$ ), (c) bilayer square  $2\Box$ , (d) bilayer hexagonal type I ( $2\Delta_I$ ), (e) bilayer hexagonal type II ( $2\Delta_{II}$ ). Red and black arrows highlight dimer orientation and registry of dimer lobes, respectively. The area of each field is  $63.6 \mu\text{m} \times 63.6 \mu\text{m}$ . Scale bars represent  $10 \mu\text{m}$ . SEM image of the hollow dimer particles is inset (f). Scale bar represents  $2 \mu\text{m}$ .

The system density in the target gap region was controlled by setting the confinement cell at a mild incline ( $10^\circ$ ) so that the particles sediment over time into the areas systematically accommodating single monolayers and multilayers. The gap height gradient across the cell of  $\sim 1 \mu\text{m mm}^{-1}$  was achieved with cured adhesive droplet arrays as spacers between the confinement cell walls. Ordered domains formed within a week and structures could typically be followed through confocal fluorescence imaging at selected gap heights for up to three weeks with cell wall modification to avoid uncontrollable particle adhesion to surfaces.

Fig. 2.1a–e presents confocal images illustrating the series of high density configurations adopted by the colloidal dimers at increasing cell height. The  $z$ -slices (top views) capture the lobe-based symmetry of the 2D and quasi-2D crystals. The relative film thickness, dimer orientation and the lobe-registry between layers is discernable from the  $x$ - and  $y$ -slices (side views). Confocal video microscopy (*i.e.*,  $z$ -stacks of images at progressive focal planes throughout the colloidal film thickness) is provided for each phase in the ESI Videos 1–6. Fig. 2.1a displays the monolayer with dimers aligned in-plane. Any  $z$ -slice taken at a focal plane less than 18% of the monolayer thickness could not distinguish this assembly from a sphere close-packed lattice. Although, the lobe-based crystal exhibited six-fold symmetry (ESI Fig. 2.3a and e), each dimer major axis randomly assumed one of the three lattice vector orientations for a triangular lattice. The major axis orientation distributions are provided in Fig. 2.2. The arrangement is equivalent to the 2D degenerate crystals predicted by Monte Carlo simulation of hard dimers in 2D<sup>13</sup> and previously observed in experiments.<sup>23</sup>

The transition to the buckled state at larger cell height was marked by vigorous ‘lobe-swinging’ fluctuations in and out of the focal plane for single lobes or both lobes, alternately, within the dimers (ESI Video 2). The  $z$ -slice in Fig. 2.1b shows a labyrinth buckled state where, predominantly, dimer tilt defines the alternating chains of demoted lobes. Several corrugated substructures are apparent including linear and zig-zag<sup>22</sup> buckling with local rectangular symmetry as well as disordered bucking (*i.e.*, randomly raised lobes). Just as for spheres, dimer buckling can be attributed to geometric frustration for a confinement gap size incommensurate with an integral layer number.<sup>17,29,30</sup>

Fig. 2.1c depicts a bilayer square structure with respect to the dimer lobes. The  $2\Box$  geometry occupies less height than the more efficient  $2\Delta$  packing and is thus observed before it in the cascade of arrangements. The dimer lobes in the lower layer of the  $2\Box$  degenerate crystal lie in registry with the square interstices of the upper layer. Within a grain, the particle major axes align along the cubic  $\langle 111 \rangle$  diagonal directions at random (Fig. 2.2b). Occasionally, a single in-plane dimer contributes to a layer leaving a dimer vacancy in the other, or a dimer pair with in-plane orientations forms a crisscross to fit the square symmetry (ESI Fig. 2.3b and f) in both layers.

Fig. 2.1d shows the lower layer of the  $2\Delta_I$  structure at mid-plane where the six-fold symmetry of the dimer lobes is apparent but, in general, the dimer profile is not. Most particles slant out-of-plane to yield layer stacking with lobes below every other hexagonal interstice in the upper layer. The major axis orientations are mainly distributed among six modes (Fig. 2.2c). The same site tiling is also attained *via* in-

plane oriented dimers ( $2\Delta_{II}$ ) as shown in Fig. 2.1e, in which the dimer profiles at the mid-plane of the upper layer in the  $z$ -slice indicate in-plane particle alignment and the  $x$ - $y$  slices reveal the presence of a bilayer. The  $2\Delta_{II}$  dimer arrangement is equivalent to two close-packed layers of the  $1\Delta$  degenerate crystal and Fig. 2.2d shows three modes in the orientation distribution, accordingly.

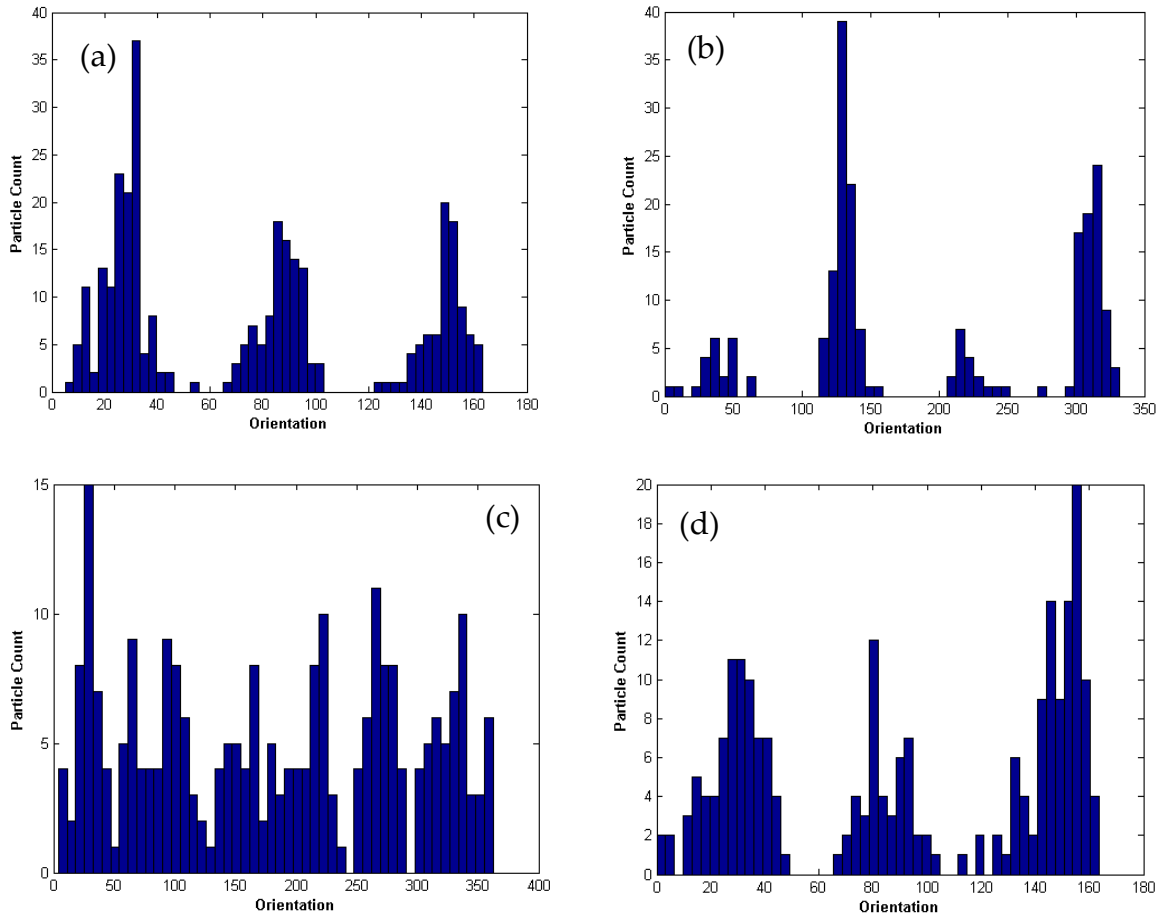


**Figure 2.2.** Histograms of dimer particle orientations from confocal microscopy experiments. 200-300 particles were measured for each structure. (a) hexagonal monolayer ( $1\Delta$ ), (b) bilayer square  $2\Box$ , (c) bilayer hexagonal type I ( $2\Delta_I$ ), (d) bilayer hexagonal type II ( $2\Delta_{II}$ ). For the  $2\Delta_{II}$  arrangement small grain size and measurements across multiple grains impacts the clarity of the six modes.

A comparison of experimental results with the cascade of structures as a function of height determined from simulations provides a simple limiting case and reference points that establish the degree to which the synthesis (*i.e.*, irregular aggregates, polydispersity) or processing issues (*i.e.*, hydrodynamic or gravitational effects, particle sticking to cell walls, *etc.*) drive the phases significantly away from the configurations that would be obtained under equilibrium conditions (dominated by Brownian motion). Specifically, we investigated the phase behavior using Monte Carlo simulations in the isothermal–isobaric and isothermal–isostress ensembles, where the number of particles  $N$ , temperature  $T$ , and the lateral pressure  $P_t$ , were kept constant. The peanut-shaped colloidal dimers were represented by two tangent hard spheres of diameter  $\sigma$ . Model particles were confined between two parallel hard walls, separated by a distance  $H^* = H/\sigma$  in reduced units.

Selected equation of state mappings of the system pressure *versus* particle density (*i.e.*, packing fraction,  $\phi$ ) are shown in Fig. 2.3 (line with circle markers). The discontinuity in density observed for the majority of the fluid–solid and solid–solid transitions suggests that these transitions are first order. A set of order parameters was used to detect phase transitions and for the characterization of the stable phases. The global order of the dimer lobes in the layers was analyzed using bond-orientational order parameters  $\Psi_4$ , and  $\Psi_6$ . These order parameters are defined by

$$\Psi_n = \frac{1}{N} \left| \sum_{j=1}^N \frac{1}{n_j} \sum_{k=1}^{n_j} \exp(in\theta_{jk}) \right|, \quad (1)$$

for  $n = 4, 6$ . In eqn (1),  $\theta_{jk}$  is the angle made by the bond between the spherical site  $j$  and its nearest neighbors with respect to an arbitrary axis, and  $n_j$  is the number

of nearest neighbors of particles  $j$ . Six-fold bond angular order in the layers is detected with  $\Psi_6$ , while four-fold bond angular order is detected with  $\Psi_4$ . For the buckled phase 1B, both  $\Psi_4$  and  $\Psi_6$  have moderate to high values (Fig. 2.3b). The fraction of particles oriented out-of-plane  $\alpha$  (Fig. 2.3, star markers) shows disjointed increases for the phase sequence with height,  $1\Delta \rightarrow 1B \rightarrow 2\Box$ . Within the  $2\Delta$  phase space, the  $\alpha$  parameter values distinguish a continuous  $2\Delta_I \rightarrow 2\Delta_{II}$  phase transformation since the particles major axes re-orient smoothly with the system density to align in-plane.

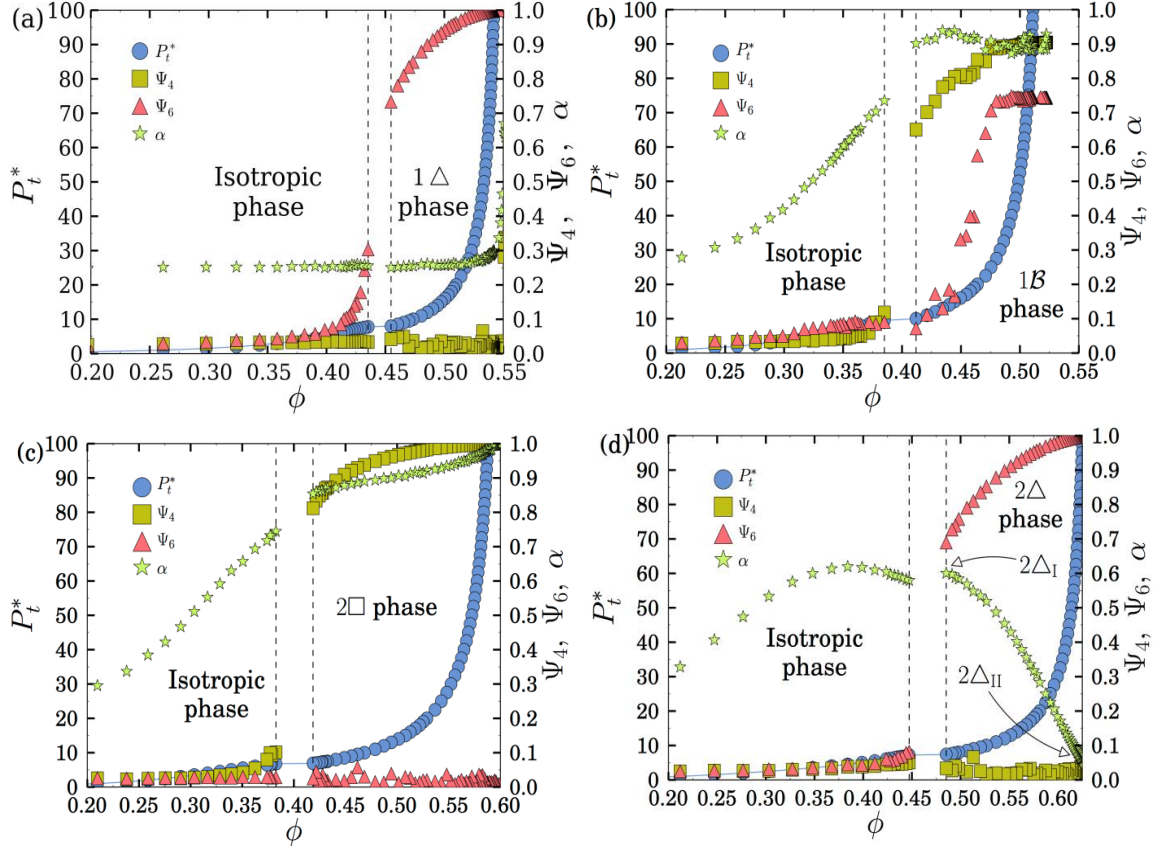


**Figure 2.3** Monte Carlo simulation results for the equation of state (EoS) for hard dimers under different confinements: (a)  $H^*=1.10$ , (b)  $H^*=1.60$ , (c)  $H^*=1.70$ , (d)  $H^*=1.90$ . Pressure,  $P_t^*$ ; bond orientational order parameters,  $\Psi_4$ , and  $\Psi_6$ ; and fraction of particles oriented out-of-plane,  $\alpha$ , as a function of the packing fraction  $\phi$ . Lateral pressure and packing fraction are represented in reduced units:  $P_t^*=P_t\sigma^3/(k_B T)$  and  $\phi=2N\pi/(6V)$  respectively, where  $k_B$  is Boltzmann's constant and  $V$  is the volume of the system.

The corresponding order parameters for the states in the wedge cell confinement experiments are provided in Table 1. The buckled phase from experiment was not analyzed quantitatively because of the variety of substructures.

**Table 2.1** Bond Orientational Order Parameters for Experimental Phases

Phase	$\psi_6$	$\psi_4$
1 $\Delta$	0.81	0.12
2 $\square$	0.35	0.66
2 $\Delta_I$	0.62	0.16
2 $\Delta_{II}$	0.72	0.15

The bond-orientational order in the experimental phases show significant deviations from the simulation values, however, the general trend in the parameter changes upon the structural transition with height is consistent with the simulations. Moreover, the experimental lobe pair correlation functions (*i.e.*, radial distribution function, descriptor of translational symmetry within a layer) agree well with the envelope of the simulated ones out to the sixth nearest neighbor peaks (Fig. 2.4). The correlation length in lobe positional order in the experiments is also limited, less than 20  $\mu\text{m}$ .

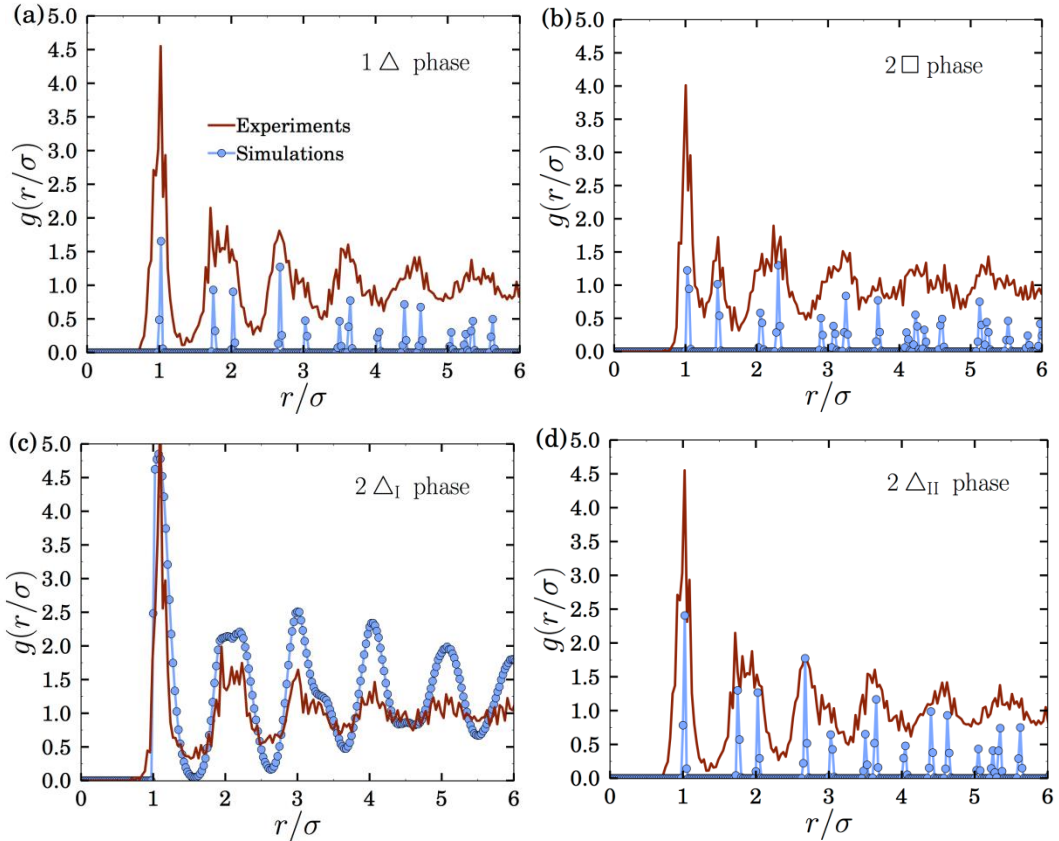


**Figure 2.4** Lobe pair correlation functions,  $g(r)$ , for monolayer and bilayer degenerate crystals. For convenience, the sharp peaks in the simulated curves in (a), (b), and (d) are rescaled in height to show them below the experimental curves. The simulation peaks in (c) are unscaled and their width is consistent with the structures factors presented in Supplemental Figure 2.

A number of defect pairs (5- and 7-nearest neighbors) and grain boundaries degrade the ordering as is evident in the Voronoi tessellations constructed from the confocal images (Fig. 2.5). There is less distortion for the monolayer because most irregular particle aggregates cannot fit within the restricted cell height for the region. To improve the crystal quality, the particle suspensions could be purified further post synthesis using density gradient centrifugation<sup>31</sup> or flow cytometry with population sorting based on forward- and side scattering characteristics.<sup>32</sup> Another practical limitation to the formation of ultralow defect DCs even from highly purified dimer

populations is the slow annealing of defects due to restricted dislocation dynamics (*i.e.*, specific particle orientations block dislocation glide) in DCs compared to crystals from spheres.<sup>33</sup>

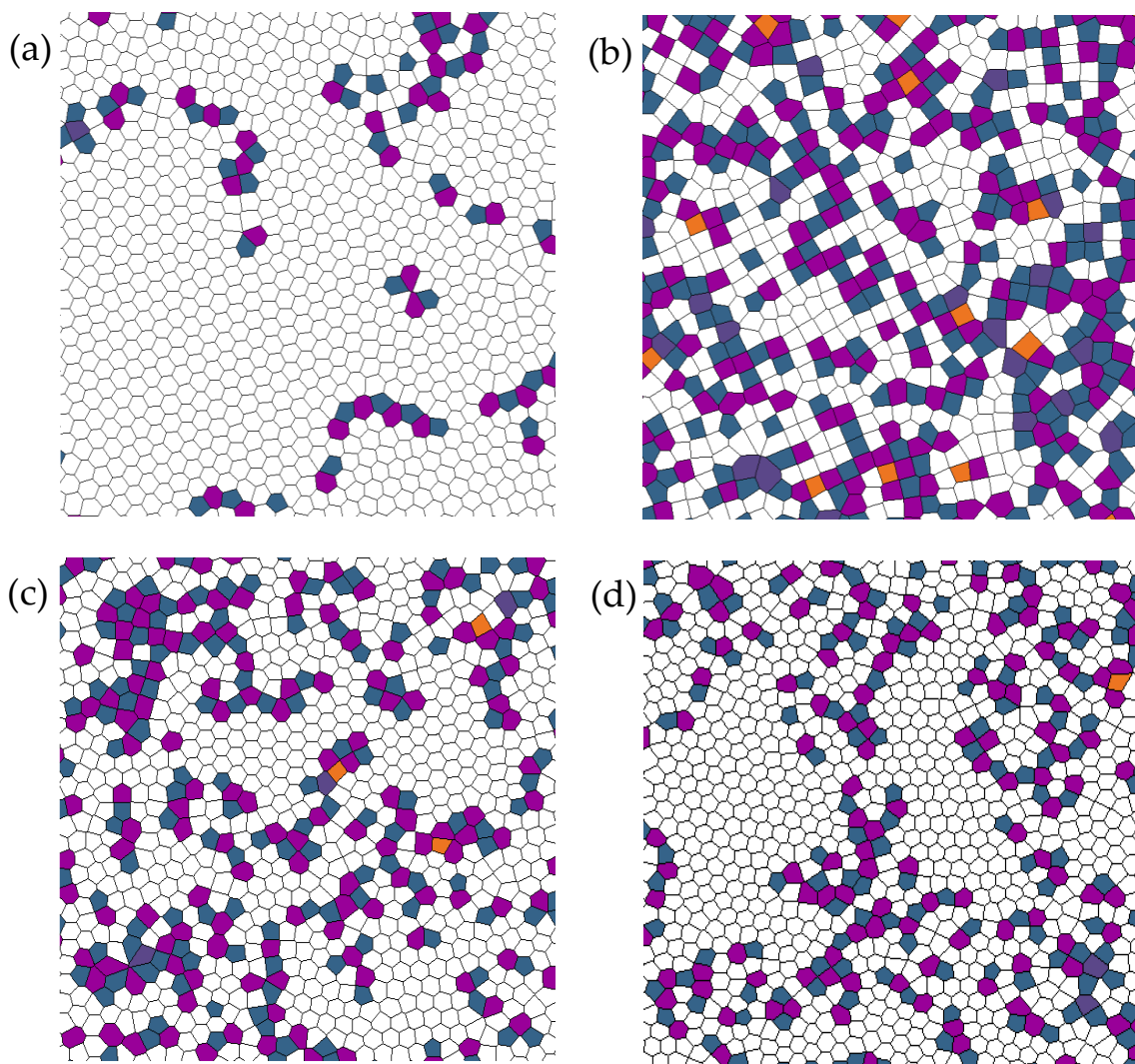


**Figure 2.5** Voronoi construction in the x-y plane for the experimental structures. (a) hexagonal monolayer ( $1\Delta$ ), (b) bilayer square  $2\Box$ , (c) bilayer hexagonal type I ( $2\Delta_I$ ), (d) bilayer hexagonal type II ( $2\Delta_{II}$ ). Color coding represents the number of nearest neighbor lobes as 4-orange, 5-blue, 6-white, 7-magenta, indigo $\geq 8$ .

The simulated phase diagram for dimer particles in the  $H^*-\phi$  plane is provided in Fig. 2.6. If we ignore that the particles are actually dimers and we only consider the spherical sites, the phase diagram and phase boundaries look very similar to those exhibited by hard spheres under confinement.<sup>17,29</sup> However, since dimers are low aspect ratio anisotropic particles having orientational degrees of freedom, out-of-plane re-orientations are also expected as demonstrated for spherocylinders<sup>34</sup> and cut-spheres.<sup>28,35</sup> The color map in the legend of Fig. 2.6 denotes the fraction of particles out-of-plane oriented.

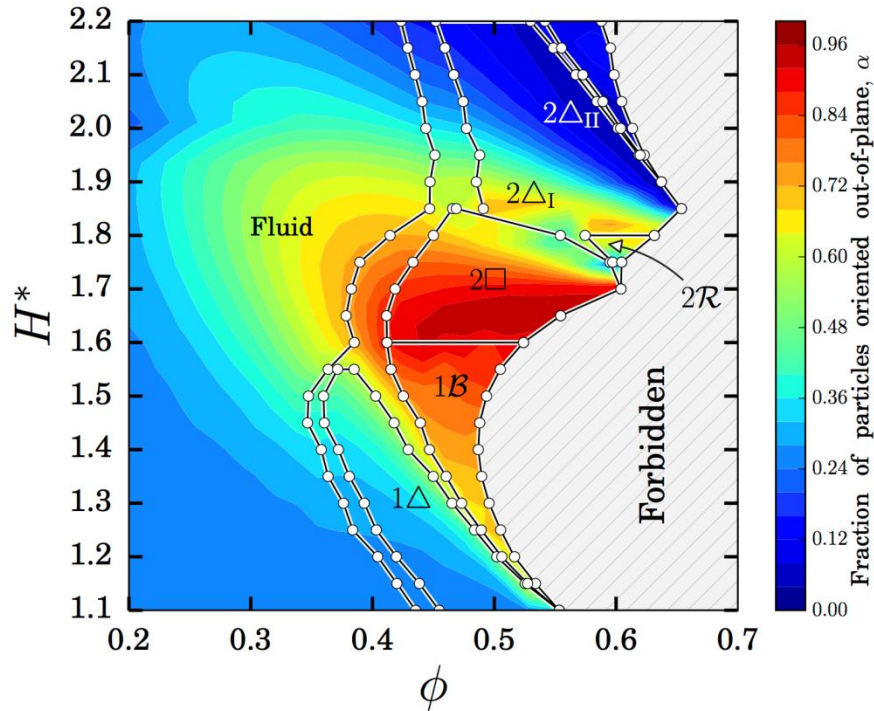


**Figure 2.6**  $H^*-\phi$  phase diagram of hard dimers (symmetric-lobed) under confinement obtained from Monte Carlo simulations. The color map represents the fraction of particles oriented out-of-plane. The forbidden region at the right of the phase diagram indicates parameters where the maximum packing fraction of hard dimers under confinement would be exceeded. This boundary of forbidden states corresponds to the densest crystal structures calculated using the method of Filion *et al.*<sup>43</sup>, at the reduced pressure of  $10^6$ .

A representative snapshot of the phase determined at the lowest gap height,  $H^* \leq 1.15$ , is shown in Fig. 2.7a and ESI Fig. 2.2. The ideal  $1\Delta$  phase is clearly the degenerate crystal predicted in the  $\phi-L^*$  phase diagram reported by Wojciechowski *et al.*,<sup>13</sup> with  $L^*$  being the reduced bond length (*i.e.*, center-to-center distance between lobes). The calculated structure factor (*i.e.* Fourier transform of the degenerate crystal) image has  $p6mm$  symmetry, though the dimer arrangement is aperiodic for the center of mass (ESI Fig. 2.2). The determination of a very narrow region where a hexatic-phase<sup>36</sup> may exist (*e.g.*, for  $H^* \rightarrow 1$ ) would necessitate a very large and focused computational effort; such a task lies beyond the scope of this work. The buckled phase was found at high densities for  $1.15 \leq H^* \leq 1.60$ . As anticipated, the 1B phase has large values for  $\alpha$  showing that the particles prefer not to be oriented parallel to the confining walls. Since, the buckled phase is an intermediary between the hexagonal and square layers, the arrangement of the dimers has some features from both states. The snapshot of a representative configuration for the 1B structure (Fig. 2.7b), illustrates that in the linear buckled phase each particle can have only four possible orientations (with the exception of possible inclusions of in-plane oriented particles) and that the azimuthal angles between dimers are  $0^\circ$  or  $120^\circ$ . The structure factor image has  $p2mm$  plane group symmetry (ESI Fig. 2.2b) clarifying that the dimer lobes localized in each sublayer are in a rectangular configuration. The red and blue coloring of the lobes indicates one lobe of each out-of-plane oriented dimer is on a vertex and the other is below (above) the centering site of the upper (lower) sublayer.

The  $2\Box$  phase exists over the gap height range  $1.60 \leq H^* \leq 1.85$ . The snapshot of degenerate crystal structure in Fig. 2.7c is exactly as we deduced from the confocal videos. The plane group symmetry of the structure factor image is  $p4mm$  (ESI Fig. 2.2c). Close to the boundary with the  $2\Delta$  region, the population of particles oriented in-plane for the  $2\Box$  phase tends to increase. An  $(n+1)\Box \rightarrow (n+1)\Delta$  intermediate phase with rhombic symmetry (2R) was predicted at high density. This pre-transitional rhombic structure for spherical colloids has been observed in both experiments<sup>19,21,37</sup> and simulations.<sup>17,29</sup>

For  $1.85 \leq H^* \leq 1.95$ , simulations reveal a continuous transformation between the  $2\Delta_I$  and  $2\Delta_{II}$  phases. For  $H^* < 1.85$  only the  $2\Delta_I$  phase was detected, while for  $H^* > 1.95$  only the  $2\Delta_{II}$  phase was identified. Representative snapshots of each bilayer hexagonal phase are shown in Fig. 2.7e and f. The  $p6mm$  plane group symmetry is clear in the structure factor images for both states (ESI Fig. 2.2d and e), however, the spots are not as sharp for the  $2\Delta_I$  case. Similarly, the Voronoi construction shows less regular hexagons for  $2\Delta_I$ . These differences reflect the greater fluctuations about the lobe lattice sites. The most efficient packing at high densities is obtained for in-plane particle orientations. However, for each MC expansion run the particles tend to reorganize on equilibration into a structure having more particles oriented out-of-plane, which facilitates the expansion of the layers.

Interestingly, for all values of  $H^*$  in the phase diagram, the fluid phase retains some memory of the out-of-plane orientation that the particles possessed in the ordered state. Such a memory (or correlation) is stronger near the melting point and gradually fades away as the concentration decreases (Fig. 2.6, color gradient within

fluid region). This is consistent with reports for confined spheres that the character of the solid phase can be anticipated from the structured fluctuations in the fluid precursor.<sup>37</sup> Another unique feature evident in Fig. 2.6 is that by changing  $H^*$  between, for example 1.7 and 2.0 while keeping  $\phi$  constant ( $\phi > 0.5$ ), dimers would not only arrange in a different bilayer structure ( $\square \leftrightarrow \Delta$ ), but also experience a drastic shift in the fraction of particles oriented out-of-plane (between nearly 1 to nearly 0!). Such changes would likely translate into large modulations of mechanical properties, suggesting potential uses for applications involving sensors and negative Poisson-ratio materials (*i.e.*, particles “stand up” against the compression direction).

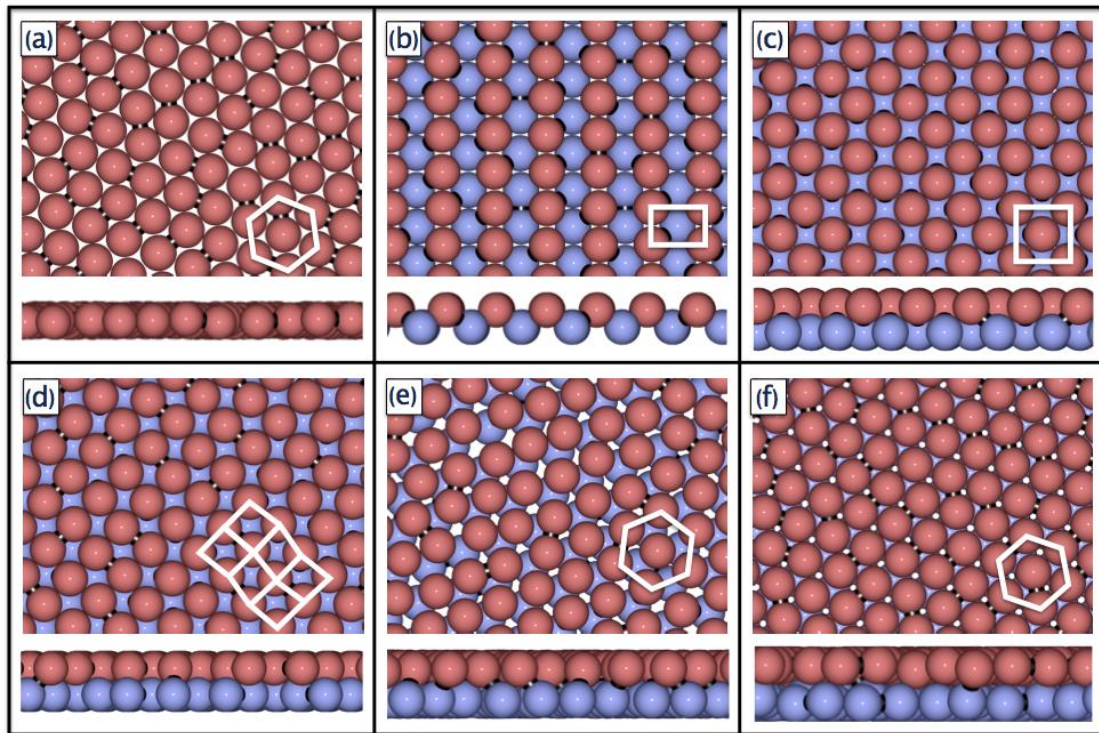


**Figure 2.7** Representative configurations of the stable phases observed in the phase diagram of hard dimers. (a) hexagonal monolayer ( $1\Delta$ ), (b) buckled state ( $1B$ ), (c) bilayer square  $2\square$ , (d) bilayer rhombic  $2R$  (e) bilayer hexagonal type I ( $2\Delta_I$ ), (f) bilayer hexagonal type II ( $2\Delta_{II}$ ). For each case panels shows a top view (top) and lateral view (bottom).

The experimental results here can only be qualitatively compared with the simulation phase diagram because the packing fraction in the colloidal systems is difficult to measure accurately from the confocal data. Estimates derived from the height and total volume in confocal video images are provided in ESI Table 2.1. In particular, the 1B packing density estimate lies outside the theoretical phase boundary, likely because of the partial order inherent in the experimental labyrinth configuration. As in previous confined systems,<sup>35</sup> the phases observed experimentally are the lowest-density ordered structures found in simulation for a given  $H^*$ , suggesting a kinetic limitation of our experiments to achieve the densest packing for some cases. In our estimates derived *via* particle tracking, there were no packing fractions above 0.57 associated with the experimental arrangements. Thus, Fig. 2.6 traces well the structural trends found experimentally for varying  $H^*$ , while the predicted 2R structure was not (and would not be) observed.

Several other particle morphologies in systems having high structural degeneracy would be of interest for further phase behavior studies as a function of gap height—heteronuclear dimers<sup>13</sup> with reduced bond length between 0.92 and 1, cyclic trimers,<sup>38</sup> rectangular prisms with 2 : 1 aspect ratio (*i.e.*, hard-cube dimers),<sup>39</sup> *etc.* Wedge cell experiments may be applied for any arbitrary particle geometry and all of these shapes have been prepared in sufficient quantities *via* direct synthesis or microfabrication.<sup>6</sup> In addition, the homonuclear silica dimers under confinement can be further investigated in refractive index matching fluid (*i.e.*, dimethylsulfoxide-water) up to reduced gap heights of seven. Such studies will establish whether degenerate tilings of the expected prismatic phases with square,

triangular or rhomboid base will be observed and what the mechanism for vicinal surface rearrangements<sup>20</sup> may be in such thin dimer films under confinement.

## 2.5 Conclusion

For the materials engineering of colloid-based photonic crystals, this work demonstrates the power of combining new colloidal building blocks with processing strategies to produce diverse symmetry breaking structures.<sup>40,41</sup> The field is ripe for establishing greater understanding of how photonic properties correlate with order descriptions analogous to those in molecular soft matter and molecular solids. The quasi-2D degenerate crystals here represent an uncharted class of photonic solid templates with well-defined partial orientational order. The structures could be inverted (*i.e.*, high refractive index matrix with air pores or *vice versa* for double inversion<sup>42,43</sup>) by physical vapor deposition or atomic layer deposition of semiconductors to obtain large refractive index modulations. The calculation of photonic properties for these colloid-based DCs is the subject of our continuing work. In particular, we expect enhanced photonic properties will be realized for  $\Delta$  and  $\square$  arrangements from the moderate to high Brillouin zone isotropy combined with symmetry reduction from the basis shape and random tiling of the underlying lattices. Promising properties for a few related partial order structures have already been determined. For example, pentagonal air holes randomly taking one of three orientations ( $0^\circ$ ,  $+24^\circ$ ,  $-24^\circ$ ) in a silicon slab with a single line defect waveguide configuration were shown to promote highly localized optical resonances and effective cavity quality factor up to 150,000.<sup>44</sup>

## REFERENCES

1. G. M. Whitesides and B. Grzybowski, *Science*, 2002, **29**, 2418.
2. S. C. Glotzer and M. J. Solomon, *Nature*, 2007, **6**, 557.
3. Q. Chen, S. C. Bae and S. Granick, *Nature*, 2011, **469**, 381.
4. C. J. Hernandez and T. G. Mason, *J. Phys. Chem. C Lett.*, 2007, **111**, 4477.
5. A. Yethiraj, *Soft Matter*, 2007, **3**, 1099.
6. S. M. Yang, S. H. Kim, J. M. Lim, G. R. Yi, *J. Mater. Chem.*, 2008, **18**, 2177.
7. U. Agarwal and F. Escobedo, *Nature Mater.*, 2011, **10**, 230.
8. Z. L. Zhang, A. S. Keys, T. Chen and S. C. Glotzer, *Langmuir* 2005, **21**, 11547.
9. N. Koneripalli, R. Levicky, F. S. Bates, J. Ankner, H. Kaiser and S.K. Satija, *Langmuir*, 1996, **12**, 6681.
10. Y. Wu, G. Cheng, K. Katsov, S. W. Sides, J. Wang, J. Tang, G. H. Fredrickson, M. Moskovits and G. D. Stucky, *Nature Mater.*, 2004, **3**, 816.
11. J. C. Tracy, *J. Chem. Phys.*, 1972, **56**, 2736-2747.
12. K. Takemura, S. Minomura, O. Shimomura, Y. Fujii and J. D. Axe, *Phys. Rev. B*, 1982, **26**, 998.
13. K. W. Wojciechowski, *Phys. Lett. A*, 1987, **122**, 377.
14. K. W. Wojciechowski, D. Frenkel and A. C. Branka, *Phys. Rev. Lett.*, 1991, **66**, 3168.
15. K. W. Wojciechowski, *Phys. Rev. B*, 1992, **46**, 26.
16. P. Pieranski, L. Strzelecki and B. Pansu, *Phys. Rev. Lett.*, 1983, **50**, 900-903.
17. A. Fortini and M. Dijkstra, *J. Phys. Condens. Matter*, 2006, **18**, L371-L378.
18. B. Pansu, Pi. Pieranski and Pa. Pieranski, *J. Phys. (Paris)*, 1984, **45**, 331.

19. S. Nesper, C. Bechinger, and P. Leiderer, *Phys. Rev. Lett.*, 1997, **79**, 2348.
20. F. Ramiro-Manzano, F. Meseguer, E. Bonet and I. Rodriguez, *Phys. Rev. Lett.*, 2006, **97**, 028304-1.
21. F. Ramiro-Manzano, E. Bonet, I. Rodriguez and F. Meseguer, *Soft Matter*, 2009, **5**, 4279.
22. Y. Han, Y. Shokef, A. M. Alsayed, P. Yunker, T. C. Lubensky, and A. G. Yodh, *Nature*, 2008, **456**, 898.
23. S. H. Lee, S. J. Gerbode, B. S. John, A. K. Wolfgang, F. A. Escobedo, I. Cohen, and C. M. Liddell, *J. Mater. Chem.*, 2008, **18**, 4912.
24. J. Henzie, M. Grünwald, A. Widmer-Cooper, P.L. Geissler and P. Yang, *Nature Mater.*, 2012, **11**, 131.
25. C.Graf, D.L.J. Vossen, A. Imhof and A. van Blaaderen, *Langmuir*, 2003, **19**, 6693.
26. D. Frenkel, *Soft condens. matter, Physica A*, 2002, **313**, 1.
27. A. B. Fontecha, and H. J. Schope, *Phys. Rev. E*, 2008, **77**, 061401-1.
28. E. K. Riley and C. M. Liddell, *Langmuir*, 2010, **26**, 11648.
29. M. Schmidt and H. Löwen, *Phys Rev. Lett.*, 1996, **76**, 4552.
30. R. Zangi and S. A. Rice, *Phys. Rev. E*, 2000, **61**, 671.
31. A. F. Demirors, P. M. Johnson, C. M. van Kats, A. van Blaaderen and I. Arnout, *Langmuir*, 2010, **26**, 14466.
32. O. Siiman, K. Gordon, A. Burshteyn, J. A. Maples and J. K. Whitsell, *Cytometry*, 2000, **41**, 298.
33. S. J. Gerbode, U. Agarwal, D. C. Ong, C. M. Liddell, F. Escobedo, and I. Cohen, *Phys. Rev. Lett.*, 2010, **105**, 078301-1.

34. P. Bolhuis and D. Frenkel, *J. Chem. Phys.*, 1997, **106**, 666.
35. C. Avendaño and F. A. Escobedo, *Soft. Matter*, 2012, **8**, 4675.
36. S. A. Rice, *Chem. Phys. Lett.*, 2009, **479**, 1.
37. S. Naser, T. Palberg, C. Bechinger and P. Leiderer, *Prog Coll Pol Sci S*, 1997, **104**, 194.
38. M. D. Weed, H. P. Seigneur and W. V. Schoenfeld, *Proc. SPIE* **7223**, 2009, 72230Q.
39. A. Donev, J. Burton, F. H. Stillinger and A. Torquato, *Phys. Rev. B*, 2006, **73**, 054109-1.
40. Y. Lu, Y. Yin, and Y. Xia, *Adv. Mater.*, 2001, **13**, 415.
41. M. Maldovan, E. L. Thomas, Wiley-VCH, Weinheim, 2009.
42. C. Lopez, *Adv. Mater.*, 2003, **15**, 1679.
43. T. Ruhl, P. Spahn, C. Hermann, C. Jamois and O. Hess, *Adv. Funct. Mater.*, 2006, **16**, 885.
44. J. Topolancik, F. Vollmer, B. Illic, *Appl. Phys. Lett.*, 2007, **91**, 201102-1.
45. T. Sugimoto, M. M. Khan and A. Muramatsu, *Colloids Surf. A*, 1993, **70**, 167.
46. L. Fillion, M. Marechal, B. van Oorschot, D. Pelt, F. Smalenburg, and M. Dijkstra, *Phys. Rev. Lett.*, 2009, **103**, 188302-1.

## CHAPTER 3

### Substitutionally Disordered Phases from Binary Sphere and Dimer Mixtures Under Confinement

#### 3.1 Abstract

Binary shape mixtures of spheres and peanut-shaped particles are self-organized into substitutionally disordered phases using wedge-cell confinement. Spheres and peanut-shaped particles are compatible with lobes sizes within ten percent of each other. Particle shape templates with core-shell morphology are sacrificed to obtain hollow silica shells. This design minimizes segregation between the two particle shape populations by reducing density mismatch. Wedge confinement allows the systematic observation of phase transitions as a function of height. Using fast confocal microscopy, five distinct phases are found between one and two integral layers following the progression  $1\Delta$ (hexagonal)  $\rightarrow$   $1\beta$ (buckled)  $\rightarrow$   $2\Box$ (square)  $\rightarrow$   $2\Delta_I$ (hexagonal)  $\rightarrow$   $2\Delta_{II}$ (hexagonal). This sequence is similar to that of hard spheres with the addition of major axis orientations for the dimers. The assemblies show substitutional disorder on the lattices and degeneracy in the dimer orientation. The substitutional disorder follows from the Hume-Rothery rules for atomic isomorphous phases. Monte Carlo simulations establish the ideal phases and the phase diagram for the shape mixtures.

---

\*To be published as: K. Muangnapoh, C. Avendano, F. A. Escobedo, C. M. L. Watson. "Substitutionally Disordered Phases from Binary Sphere and Dimer Mixtures Under Confinement," *Small*, submitted (2017.)

### 3.2 Introduction

The control of the self-assembly of colloidal particles using external fields has been the subject of intense research because of its importance from a fundamental point of view and the enabling applications such as security and anticounterfeiting, sensing and photonics.<sup>1-4</sup> Some examples of external fields used to control self-assembly are electric and magnetic fields, thermal gradients, gravitational field, shear flows and spatial confinement.<sup>5-13</sup> The effect of wedge confinement has been studied by experiments, and confirmed by molecular simulations,<sup>14</sup> for example, spherical polystyrene particles dispersed in water, lead to a simple sequence of ordered structures. In fact, for increasing separations between the repulsive surfaces, a sequence of layers with triangular ( $\triangle$ ) and square ( $\square$ ) symmetry has been observed:

$$1\triangle \rightarrow 2\square \rightarrow 2\triangle \rightarrow 3\square \rightarrow \dots \rightarrow n\triangle \rightarrow (n+1)\square \rightarrow (n+1)\triangle, \quad (1)$$

where  $n$  is the number of layers in the films. Similar structures were reported using direct real-space imaging and diffraction patterns.<sup>15</sup> The mechanisms of the transformations  $n\triangle \rightarrow (n+1)\square$  and  $(n+1)\square \rightarrow (n+1)\triangle$  have also been studied experimentally.<sup>14, 16-19</sup> It has been shown that instead of the abrupt transitions implied by Eq. (1), the transitions occur semi-continuously through the formation of intermediate structures. In the case of the transformation  $1\triangle \rightarrow 2\square$ , this intermediate structure is formed when in-plane lattice rows in the  $1\triangle$  lattice are displaced up and down to form a buckled phase ( $1\beta$ ).<sup>16, 20</sup> Similarly, it has been reported that the mechanism of the transformation  $2\square \rightarrow 2\triangle$  is through an intermediate rhombic (R) structure<sup>21</sup>. Some of the above experimental systems

are at a condition in which the particles interact as nearly hard-spheres. This model has proven to be useful in unraveling important questions in the phase behavior and dynamical properties of real systems.<sup>22-26</sup>

Several pioneering studies have established the promise of assembly in binary systems. For example, it is well known that size-binary mixtures of colloidal spheres form crystal structures determined by the size ratio and concentrations of large and small particles.<sup>27-29</sup> When the particle populations have small, opposite charges, a rich variety of phases (i.e., NaCl, CsCl, LS<sub>4</sub>, LS<sub>6</sub>, LS<sub>8</sub>, etc.) is predicted and some of these have been demonstrated experimentally.<sup>9</sup> Moreover, lattice-compatible shape-binary mixtures of regular polyhedra<sup>30</sup> and polygons<sup>31</sup> are predicted to form Archimedean tilings, stabilized by enthalpic shape-specific and edge-specific patches.<sup>31</sup> Binary mixtures of Fe<sub>3</sub>O<sub>4</sub> and Au nanoparticles,<sup>32</sup> dendritic polymer micelles,<sup>33</sup> and star-branched terpolymers<sup>34</sup> have all been shown to assemble into Archimedean tilings.

Shape-binary phases are sought after for promising photonics properties such as anomalous refraction, slow light and photonic bandgaps.<sup>35</sup> However, there are several challenges for the creation of shape-binary mixtures including the synthesis of compatible shapes and overcoming phase separation during assembly due to differences in density, size and shape of the particle populations. Recently, lock and key colloids have been prepared from colloidal particles with spherical cavity and complementary colloidal spheres resulting in site-specific and reversible assembly.<sup>36-37</sup> Mixtures of cubes and spheres were also co-assembled in microtubules and thermally switched between the isotropic and

ordered state.<sup>38</sup> The former studies did not observe the formation of ordered “macro phases” but only of shape-binary clusters and chains. Other studies have involved the binary assembly of nanoparticles (a size scale unsuitable for photonic applications); e.g., nanoparticles with tripod and rhombus building blocks self-organize into monolayers by face-to-face stacking.<sup>39</sup>

Here, we report on the assembly of shape-binary mixtures of peanut-shaped particles (peanuts) and spheres into films under wedge-cell confinement. Sacrificial particles are used as templates for the deposition of silica shells. The hollow morphology addresses the density mismatch between the template particles so that phase separation is minimized. The self-organized structures are substitutionally disordered which follows from the Hume-Rothery Rules for isomorphous phases.<sup>40</sup> Spheres and peanuts separately tile the same sequence of phases with gap height.<sup>22, 41</sup> For shape compatibility, the peanut lobe sizes were within ten percent of the sphere size. Fast confocal microscopy and image analysis revealed five distinct phases between 1 and 2 layers. The ideal phases are degenerate tilings<sup>42</sup> with respect to the positions of spheres and peanuts and to their orientations. The binary structures can be rationalized from closest packing arguments and are in agreement with our predictions from Monte Carlo (MC) simulations of sphere and peanut mixtures under confinement.

### **3.3 Experimental Method**

#### **3.3.1 Anisotropic particle synthesis**

The  $\alpha$ -Fe<sub>2</sub>O<sub>3</sub> peanuts were synthesized using gel-sol (i.e., goethite gel dissolves and precipitates hematite sol) method under hydrothermal conditions.<sup>59</sup> A 45 mL

NaOH solution (5.625 M) was added to 50 ml FeCl<sub>3</sub> solution (2M, pre-filtered, Fisher) under vigorous magnetic stirring in a 100 mL bottle (GL45, VWR) for 5 minutes. A 5 mL aliquot of Na<sub>2</sub>SO<sub>4</sub> solution (0.6 M) was added into the bottle and agitated for 10 minutes. The solution was aged at 100°C for 8 days in a pre-heated oven. The reaction was stopped by quenching under tap water and the particles were recovered through vacuum filtration after at least three cycles of centrifugation and redispersion in DI water (18.2 MΩ-cm, Millipore Direct-Q 3UV). Dry samples were collected after 1 day.

Rhodamine isothiocyanate (RITC) labeled silica was coated in layers on the core particles. Specifically, α-Fe<sub>2</sub>O<sub>3</sub> peanuts (0.5 g), 4 mL DI water and 12 mL of ammonia solution (27% w/w, Mallinckrodt) were dispersed in 74 mL of isopropyl alcohol medium in a round bottom flask. The reaction was done in a bath at 30°C under ultrasonication (probe power 14 w) applied by an immersion probe (Sonic & Materials Inc.) Aliquots of sol-gel precursor— 100 μL tetraethylorthosilicate (TEOS, Sigma-Aldrich) and 60 μL of the rhodamine dye solution [1 mL ethanol, 90 μL of 3-(aminopropyl) triethoxysilane (APS, Aldrich) and 25 mg RITC powder (Sigma)]— were injected every two hours for 2 addition cycles. To deposit an outer non-fluorescent silica layer, particles were added to deionized water, ammonia solution, and isopropyl alcohol in the quantities given above and underwent the sonochemical reaction with a single dose of 100 μL TEOS for 2 hrs. The particles were washed in isopropyl alcohol for 2 cycles and in DI water for 2 additional cycles.

The hematite cores were removed using hydrochloric acid (18% in water, Sigma-Aldrich) at 45 °C for 2.5 hours. The hollow particles were washed in DI water three times and redispersed into a  $2.75 \times 10^{-5}$  M polyvinylpyrrolidone (PVP, MW 40 000; Sigma-Aldrich) in DI water solution.

### **3.3.2 Spherical Particle Synthesis**

Polystyrene and silica hybrid particles were prepared in core-shell morphology by coating spherical polystyrene particles (1.5  $\mu\text{m}$  diameter, Polyscience, Inc.) with rhodamine-modified silica. Specifically, a silane coupling agent is applied by tumbling 60 mg of the spheres with 9.5 mL of absolute ethanol and 500  $\mu\text{L}$  of APS. Excess APS is removed by washing in IPA for 4 cycles. The sample was redispersed in a mixture of 86 mL IPA and 4 mL of ammonia solution in a round bottom flask. The reaction was done in a bath at 30° C under constant ultrasonication (12 W). Aliquot of 16.5  $\mu\text{L}$  TEOS and 10  $\mu\text{L}$  rhodamine dye were added every hour for a total of 3 additions. The reaction was continued overnight before the dye-coated particles were washed in IPA for two cycles. An additional plain silica layer was applied by adding 30  $\mu\text{L}$  TEOS to a mixture of the particles in 74 mL IPA, 4 mL DI water and 12 mL ammonia under continued ultrasonication for 3 hours at 30° C. The particles were then washed in IPA for 2 cycles and in DI water for 2 cycles.

To create hollow spherical shells, the core-shell particles were calcined using 2-step temperature profile. The sample was placed in an oven at 300° C for 2 hours and at 550° C for 5 hours to remove polystyrene cores. The hollow shells were coated with a fluorescently-labeled silica layer. The dry sample was

redispersed in a mixture of 86 ml IPA and 4 mL ammonia solution. An aliquot of 10  $\mu$ L of the rhodamine dye and 20  $\mu$ L of TEOS was injected into the sample under 4-5 W ultrasonication in a dynalene bath at 30° C. After 90 minutes, additional 20  $\mu$ L TEOS was injected into the sample and the sonication continued overnight. The sample was gently washed in IPA twice at 800 rpm for 15 mins to avoid breaking the silica shells. To enhance mechanical stability, the colloids were mixed with 5 ml DI water, 10 mL ammonia solution and 75 mL IPA. An addition of 20  $\mu$ L TEOS was injected under the same sonochemical conditions for 4 hours. The sample was washed in IPA for 2 cycles and in DI water for another cycle. The hollow particles were washed in deionized water three times and redispersed into  $2.75 \times 10^{-6}$  M polyvinylpyrrolidone aqueous solution.

### **3.3.3 Shape-binary assembly**

Self-assembly of shape-binary mixtures under wedge cell confinement was studied with confocal microscopy as a function of gap height. The wedge confinement cell was built between two 22 x 50 mm coverslips on a 2 in. x 3 in. base glass slide. The coverslips were soaked in a 1 M NaOH solution for 15 minutes and thoroughly washed in DI water. One coverslip was glued to the base slide with UV adhesive. Two rows of cured UV adhesive dots were deposited as spacer before the second coverslip which was placed on top. Pressure was applied to the top coverslip by hand to bond the two coverslips and create zero height separation. The sides of the cell were sealed with UV adhesive leaving the top edge open for particle injection. A solution of PVP in DI water was pipetted

into the confinement cell and evaporated in a vacuum desiccator (Sheldon Manufacturing, Model 1400E) to prevent sticking to the cell walls. Approximately 50  $\mu\text{L}$  of the particle suspension ( $\sim 3\%$  (v/v) peanut particles,  $\sim 3\%$  (v/v) spheres) was injected into the cell. The confinement cell was sealed with UV adhesive and was tilted at  $\sim 10^\circ$  to allow the particles to assemble. The 2D and quasi 2D regions were imaged after 3-4 days, using Zeiss LSM 5 LIVE confocal microscope with 532 nm laser line excitation.

### **3.3.4 Structure analysis**

The total number of spheres and dimers were counted manually from confocal images for the calculation of volume fraction. The gap size was approximated from the maximum observed angle of the dimers in each phase. Defects were not considered and this contributes to the experimental volume fractions being less than those calculated from Monte Carlo simulations. The positions of the particles were tracked for the calculations of order parameters and the radial distribution function.

### **3.3.5 Monte Carlo Simulation**

Crystals structures for each value of  $H^* = H/\sigma$  were determined using the variable-shape box (VSB) method.<sup>53</sup> Systems of  $N = 10$  particles, i.e.  $N_1 = 6$  and  $N_2 = 4$ , provided suitable results for the binary crystals and were used for all values of  $H^*$  in the range of  $1 < H^* < 2.1$ . In our implementation of the VSB method,<sup>53</sup> for each value of  $H^*$  a structure of low packing fraction  $\phi$  was generated at random. At this packing fraction, the system is in an isotropic state. The system was first

equilibrated at a pressure of  $P_t^* = P_t\sigma/(k_B T) = 1$ , where  $P_t$  is the lateral pressure  $T$  is the absolute temperature, and  $k_B$  is the Boltzmann's constant. The system is subsequently compressed using Monte Carlo (MC) simulations in the isobaric-isothermal ( $NP_tT$ ) ensemble allowing the shape of the box to change. The lattice reduction technique was used to prevent extreme distortions of the simulation box. The pressure was increased in steps of  $\Delta P_t^* = 1$  to the value  $P_t^* = 10$  and further increased by a factor of 10 up to the value of  $P_t^* = 10^6$ . This process is repeated many times and the structures obtained at  $P_t^* = 10^6$  were saved for post-processing analysis. The crystal structures for each value of  $H^*$  are taken as the close-packed structures.

The phase behavior and equation of state were obtained by replicating the crystal structures obtained using the VSB method and expanding the crystal structures sequentially from an initial pressure  $P_t^* = 500$  to a pressure  $P_t^* = 0.5$ . Approximately 200 particles per layer were used. A MC cycle is defined as a collection of  $N$  moves that are comprised of random changes of volume and shape of the system, as well as displacements and rotation of particles. The cycles also include a bias move to sample more efficiently the phase space and it entailed breaking a bond of a peanut and forming a new bond with a randomly chosen neighboring sphere. For each state point,  $5 \times 10^5$  cycles were used for equilibration, and additional  $10^6$  cycles for production (to obtain ensemble averages). The relative frequency of move types were set as 35 % for translations, 35 % for rotations of peanuts, 20 % for bias bond breaking-forming

moves, 5 % for volume change, and 5 % for box shape change. The maximum amplitude of the attempted changes for each type of move were set to attain 30-40 % acceptance probability.

Bond breaking-formation (or bond switch) moves were implemented using an algorithm similar to the one described in reference 58 and involves the following steps (Figure S2): (a) A peanut is first selected at random. (b) One of the sites of the peanut, say  $d1$ , is selected at random. (c) The spheres  $n_{b,old}$  close to site  $d1$  are identified. A sphere is considered to be a neighbor of site  $d1$  if their separation distance is less than  $R_c < 1.2 \sigma$ . If  $n_{b,old} = 0$  the move is automatically rejected. Otherwise continue to the next step. (d) One of the  $n_{b,old}$  spheres is selected at random. (e) A bond-breaking move is performed as shown in Figure S2. The bond between sites  $d1$  and  $d2$  of the peanut is broken, while a new bond between  $d1$  and  $s1$  is formed. The move is carried out in the form of a reflection operation along a plane that is most orthogonal to the vector joining site  $d2$  and sphere  $s1$ . (f) If overlaps are detected in the new configuration, the move is automatically rejected, otherwise the number of spheres  $n_{b,new}$  close to site  $d1$  in the new configuration are determined. (g) Finally, the move is accepted with a probability  $P_{acc}(n \rightarrow o) = \min(1, n_{b,old} / n_{b,new})$ . The algorithm described is fully reversible and is particularly efficient for configurations at high volume fractions, where the standard metropolis algorithm is not able to sample efficiently the phase space.

### 3.4 Result and discussion

Sacrificial hematite peanuts were synthesized using the gel-sol method, i.e., goethite gel dissolves and reprecipitates hematite acicular nanoparticles. Nanoparticle aggregation results in the mesoscale peanuts.<sup>43-44</sup> Rhodamine functionalized-silica layers were deposited onto hematite using base-catalyzed hydrolysis and condensation of alkoxide under sonochemical conditions. The iron oxide cores were removed using concentrated hydrochloric acid to obtain hollow peanuts.<sup>45</sup> Hollow silica spheres were synthesized by depositing rhodamine-labeled silica followed by removal of the sacrificial polystyrene spherical cores<sup>46</sup>. The hollow morphologies were selected because the core materials would encourage segregation between the two shape populations. Moreover, hematite has a magnetic dipole which leads to dipolar interactions in self-assembly<sup>47</sup>.

The average size of the peanuts was 2.0  $\mu\text{m}$  in lobe diameter and 3.7  $\mu\text{m}$  in length with coefficients of variation 5.2 % and 3.4 %, respectively. The spheres were 1.8  $\mu\text{m}$  in diameter with 3.3 % coefficient of variation. These dimensions were determined from measurements of at least 50 particles using scanning electron microscopy (SEM).

Shape-binary mixtures were self-assembled in a wedge-confinement cell with gap size varying systematically along the length of the cell. Confinement in a wedge region enables the facile study of phases that optimize the packing efficiency between two- and three dimensions. When the lattice spacing of bulk crystalline structures is incommensurate with the gaps imposed by the plate separations, particles form intermediate arrangements to maximize packing entropy.<sup>15, 16, 18-20, 23-24</sup> In the present case, binary mixtures were injected into

confinement cells with gap height gradient of approximately  $1 \mu\text{m} \cdot \text{mm}^{-1}$ . The ratio of peanuts and spheres injected into the cell was 1:1 by volume and the cells were set at a  $10^\circ$  incline to settle the particles into the target gap region. Ordered domains were observed with a confocal fluorescence microscope within a week and the structures could be observed for up to a month.

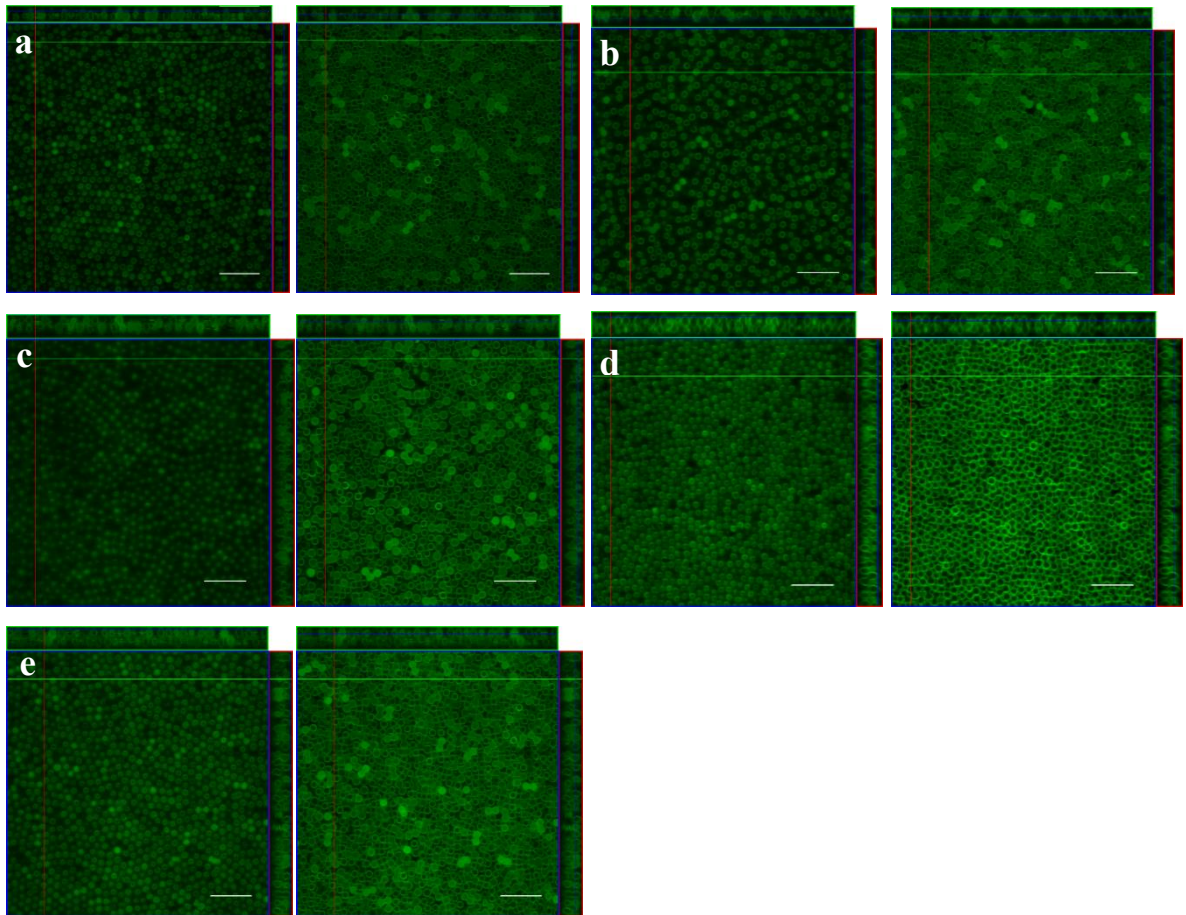


**Figure 3.1.** Confocal images for the binary self-assembly of spheres and peanuts in confinement cells. The structures observed with increasing gap height are (a) hexagonal monolayer ( $1\Delta$ ), (b) buckled state ( $1\beta$ ), (c) bilayer square  $2\square$ , (d) bilayer hexagonal type I ( $2\Delta_I$ ), (e) bilayer hexagonal type II ( $2\Delta_{II}$ ). Z-slides are taken at the tips of the particles for left images and the center for the right images. The area of each field is  $63.6 \mu\text{m} \times 63.6 \mu\text{m}$ . Scale bars represent  $10 \mu\text{m}$ .

Confocal images of binary assemblies of spheres and peanuts at high density are shown in Figure 3.1. The images show slices of five ordered structures in the x-y (center), x-z (top) and y-z (right) planes observed at increasing gap height. For each structure, z-slice images are taken at 20 % and 50 % of a layer height, where the tip and cross-section of the peanut shapes are apparent, respectively. The film thickness and orientation of the peanuts can be discerned from the x-z and y-z slices. The spheres and peanuts form phases characterized by isomorphous substitution. Specifically, the binary mixtures tile the same sequence of structures as observed in experiments for the individual morphologies.<sup>22,41</sup> Z-stack videos of the binary assembly in real time are provided in Supplemental Videos S1-5.

The lobe-based monolayer ( $1\Delta$ ) exhibited triangular symmetry; however, the spheres and peanut lobes randomly tiled the lattice as shown in Figure 3.1a. The shape mixtures form substitutionally random and show degeneracy in peanut orientations (i.e., the arrangements have high degeneracy entropy).<sup>48</sup> The peanut orientational distribution is not expected to show three distinct peaks because of the long range variation of bond angle due to the size mismatch between the spheres and peanuts. The ratio of spheres to peanuts decreases as the gap height increases (Table 3.1), in agreement with the dynamic shape factor modified Stokes' law.<sup>49</sup> The aspect ratio of the peanuts is approximately twice that of the sphere, resulting in higher drag forces so that peanuts settle at a slower rate.<sup>50</sup>

**Table 3.1.** Lobe-Based Order Parameters for Experimental Shape-Binary Phase.

Phase	Order Parameters			Spheres (%)	Peanuts (in-plane %)	Peanuts (out-of-plane %)	Gap Height (H*)	Volume fraction
	$\psi_6$	$\psi_4$	$\alpha$					
1 $\Delta$	0.74	0.35	—	63	37	—	1.35	0.37
1 $\beta$	—	—	0.60	62	15	23	1.6	0.34
2 $\square$	0.41	0.51	0.79	56	9	35	1.84	0.37
2 $\Delta_I$	0.60	0.39	0.54	57	20	23	1.98	0.50
2 $\Delta_{II}$	0.68	0.36	0.19	48	42	10	2.2	0.46

The buckled state (1 $\beta$ ) of the shape-binary system is displayed in Figure 3.1b and has a labyrinthine configuration.<sup>51</sup> Linear and zig-zag buckling (i.e., alternating chains of elevated and depressed lobes) were observed with local rectangular symmetry. This phase is marked by peanut lobes alternately swinging in and out of the focal plane and by spheres bouncing from layer to layer. A significant fraction of the particles was oriented out-of-plane ( $\alpha = 0.60$ ) as expected since 1 $\beta$  is the transition phase from 1 $\Delta \rightarrow$  2 $\square$ . This phase transition occurs because the confinement gap size is incommensurate with integral layers, just as in the single component systems. Several of the out-of-plane oriented peanuts are apparent in the confocal x-z and y-z slices.

The square bilayer structure (2 $\square$ ) for the shape-binary system is provided in Figure 3.1c. This phase shows local 4-fold symmetry for each layer. Lobes in the lower layer corresponded to the interstitial sites in the upper layer, leading to an increased angle of peanut tilt with respect to the substrate. The highest fraction of particles oriented out-of-plane was observed for the 2 $\square$  phase ( $\alpha = 0.79$ ). The tilted peanut cross-section is apparent in the z-stack video as the focal plane is

scanned through the layers (S1c). The  $2\Delta$  packing is more closely packed than the  $2\Box$ ; however, the latter phase occupies less height and is thus observed before the  $2\Delta$  phase in the sequence of structures on increasing gap size.

Two bilayer arrangements with lobe-based hexagonal symmetry,  $2\Delta_I$  and  $2\Delta_{II}$ , are presented in Figure 1d and 1e, respectively. The  $2\Delta_I$  state contains significantly more particles with tilt out-of-plane ( $\alpha = 0.54$ ) than the  $2\Delta_{II}$  phase ( $\alpha = 0.19$ ). The  $2\Delta_{II}$  binary phase is composed of two close-packed layers with the same lobe arrangement as the monolayer binary phase ( $1\Delta$ ). The reorientation of peanuts with height provides a semi-continuous transition from square to triangular symmetry.

The experimental phase behavior with gap height was compared with Monte Carlo simulation results to establish a more complete correlation between structure and external conditions by exploring parameter space more broadly. Additionally, the simulations provide a simple limiting case to gain insight into whether irregularities drive the phases significantly away from those that would be obtained under equilibrium conditions. Such irregularities in this system include minor particle size mismatch between the two shapes, size polydispersity, aggregates (i.e., synthesis imperfections), particles sticking to cell walls (i.e., processing imperfections), as well as hydrodynamic and gravitational effects. The simulation model consists of a binary mixture of  $N_1$  hard spheres of diameter  $\sigma$  and  $N_2$  peanuts formed by two tangent hard spheres also of diameter  $\sigma$ . In the simulations, the global composition of spheres to peanuts by number is

fixed at 60:40, which should be compared with the average composition of 58:42 in the experiments (Table 1). The particles are confined between two parallel hard walls separated at a distance  $H^* = H/\sigma$ . A discontinuity in the equation of state mapping (Fig. 3.2, circle markers) with density suggests a first order phase transition. Selected order parameters were used to detect and characterize the stable binary phases. The global bond-orientational order parameters for square and hexagonal symmetries ( $\Psi_4, \Psi_6$ ) are defined in Equation 2—

$$\Psi_n = \frac{1}{N} \left| \sum_{j=1}^N \frac{1}{n_j} \sum_{k=1}^{n_j} \exp(in\theta_{jk}) \right| \quad (2)$$

where,  $\theta_{jk}$  is the angle made by the bond between the spherical site  $j$  and its nearest neighbors with respect to an arbitrary axis, and  $n_j$  is the number of nearest neighbors of particles  $j$ . The phases with 6-fold symmetry ( $n = 6$ ) showed high values of  $\Psi_6$  (Fig. 3.2a, b and d). Similarly, the phases with 4-fold symmetry displayed high values of  $\Psi_4$  (Fig. 3.2c). Moderate to high values of  $\Psi_6$  and  $\Psi_4$  are apparent for the buckled phase (Fig. 3.2b). The experimental  $1\beta$  state was not quantitatively characterized because of its labyrinthine ordering.

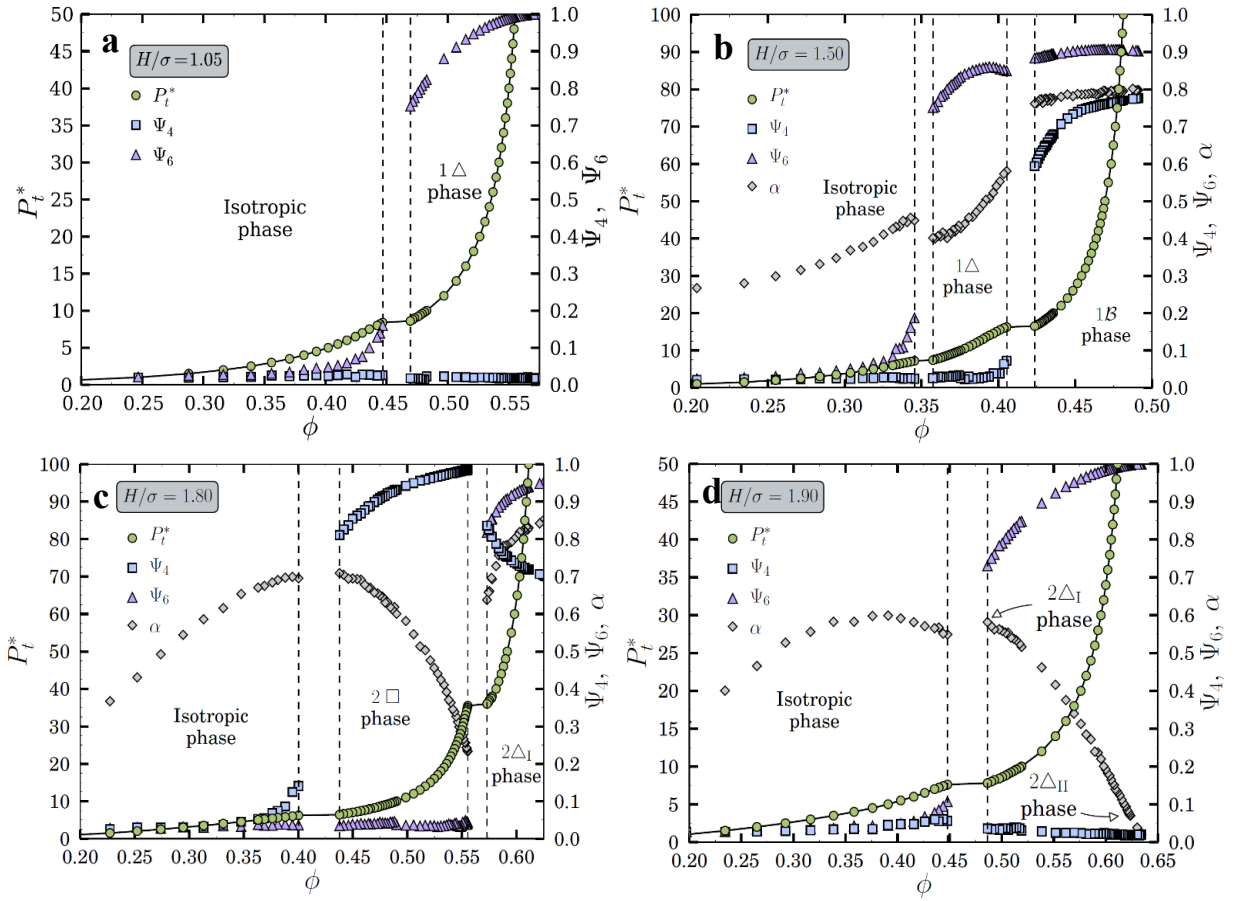


**Figure 3.2.** Monte Carlo simulation results for the equation of state (EoS) for hard peanuts and spheres confined between parallel hard walls at a distance of  $H/\sigma$ : (a)  $H/\sigma = 1.05$ , (b)  $H/\sigma = 1.50$ , (c)  $H/\sigma = 1.80$ , (d)  $H/\sigma = 1.90$ . Pressure,  $P_t^*$ ; bond orientational order parameters,  $\Psi_4$ , and  $\Psi_6$ ; and fraction of particles oriented out-of-plane,  $\alpha$ , as a function of the packing fraction,  $\phi$ . Lateral pressure and packing fraction are represented in reduced units:  $P_t^* = P_t \sigma^3 / (k_B T)$  and  $\phi = 2N\pi / (6V)$  respectively, where  $k_B$  is Boltzmann's constant and  $V$  is the volume of the system.

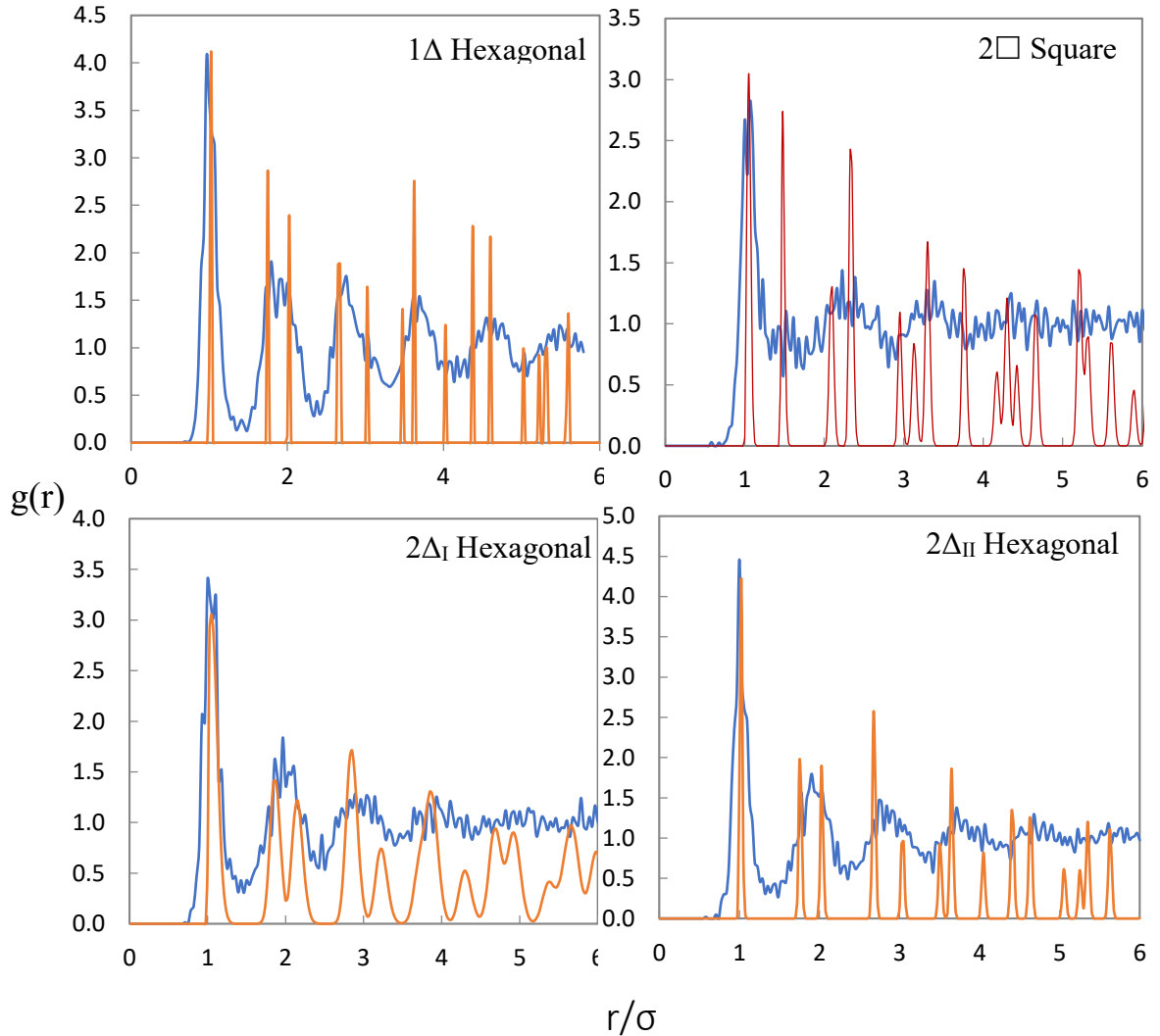


**Figure 3.3.** Lobe-based pair distribution functions,  $g(r)$ , for shape-binary structures. The abscissa values are normalized by the lobe diameter  $\sigma$ . Experimental and simulated plots are shown in blue and red, respectively.

A comparison of the experimental and simulated radial distribution functions is provided in Figure 3.3. There is general agreement out to 4-6 nearest neighbors (first six peaks) for the phases with hexagonal symmetry. Three distinct peaks are apparent for the experimental  $2\Box$  structure, although the second peak has lower  $g(r)$  values than expected. The experimental bond

orientational order parameters (Table 3.1) qualitatively follow the trends, illustrated by the simulated order parameters, with height. As expected, the  $1\Delta$  phase was found to have a high value of  $\Psi_6$  and a low value of  $\Psi_4$ . The experimental bilayer phases with hexagonal symmetry had lower  $\Psi_6$  values as compared to the simulations presumably because more particle aggregates can fit into this higher gap height region of the cell. The experimental  $2\square$  structure had a  $\Psi_4$  value that was 46% higher than that of the  $1\Delta$  phase.

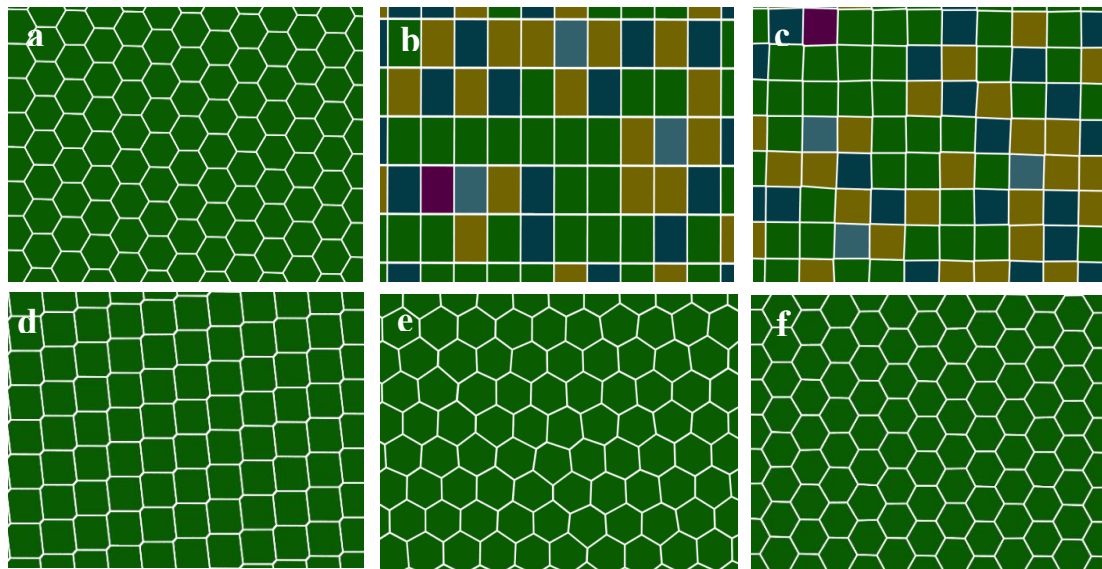


**Figure 3.4.** Simulated Voronoi constructions for the binary system of hard peanuts and spheres. (a) hexagonal monolayer ( $1\Delta$ ), (b) buckled state ( $1\beta$ ), (c) bilayer square  $2\square$ , (d) bilayer hexagonal type I ( $2\Delta_I$ ), (e) bilayer hexagonal type II ( $2\Delta_{II}$ ). Color coding represents the number of nearest neighbor lobes.

The simulated Voronoi constructions (Fig. 3.4) depict the ideal number of nearest neighbors by the number of polygon edges and the structural order by the regularity of the polygon shape. The 5 and 7 sided pairs of polygons in the experimental Voronoi diagrams (Fig. 3.5) indicate dislocations and chains of these signify grain boundaries.

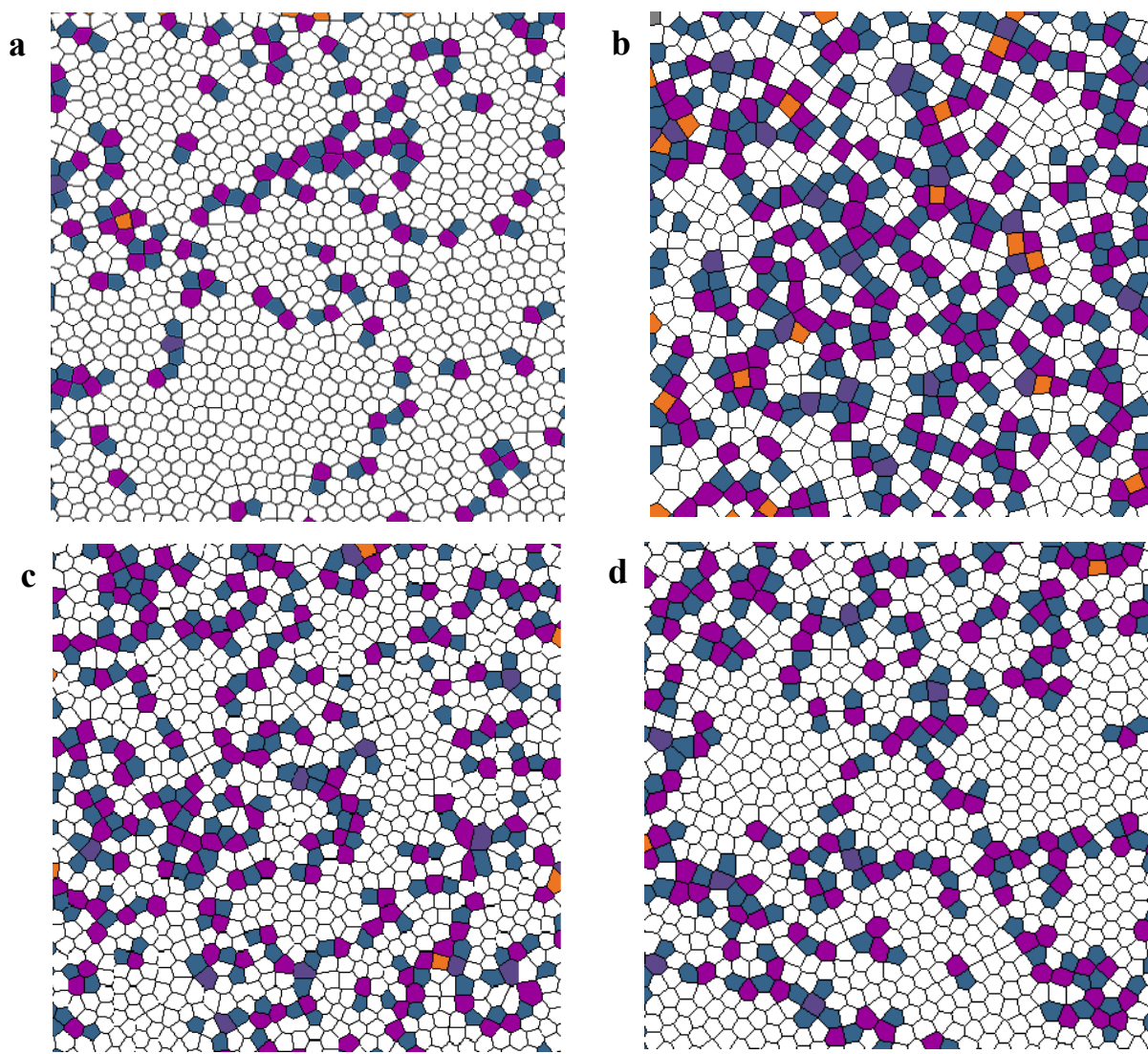


**Figure 3.5.** Voronoi constructions for the shape-binary structures. (a) hexagonal monolayer ( $1\Delta$ ), (b) bilayer square  $2\square$ , (c) bilayer hexagonal type I ( $2\Delta_I$ ), (d) bilayer hexagonal type II ( $2\Delta_{II}$ ). Color coding represents the number of nearest neighbor lobes as 4-orange, 5-blue, 6-white, 7-magenta,  $\geq 8$ -indigo.

The experimental  $1\Delta$  phase shows the largest grains in the tessellation in agreement with the longer correlation lengths of the radial distribution function. The structure with square symmetry is decorated with many higher order Voronoi cells due to local deviation of the particles from the lattice sites.<sup>52</sup> The

simulated phase diagram  $H^*$ -  $\phi$  for binary assemblies of spheres and peanuts as a function of the confinement height is shown in Fig. 3.6.

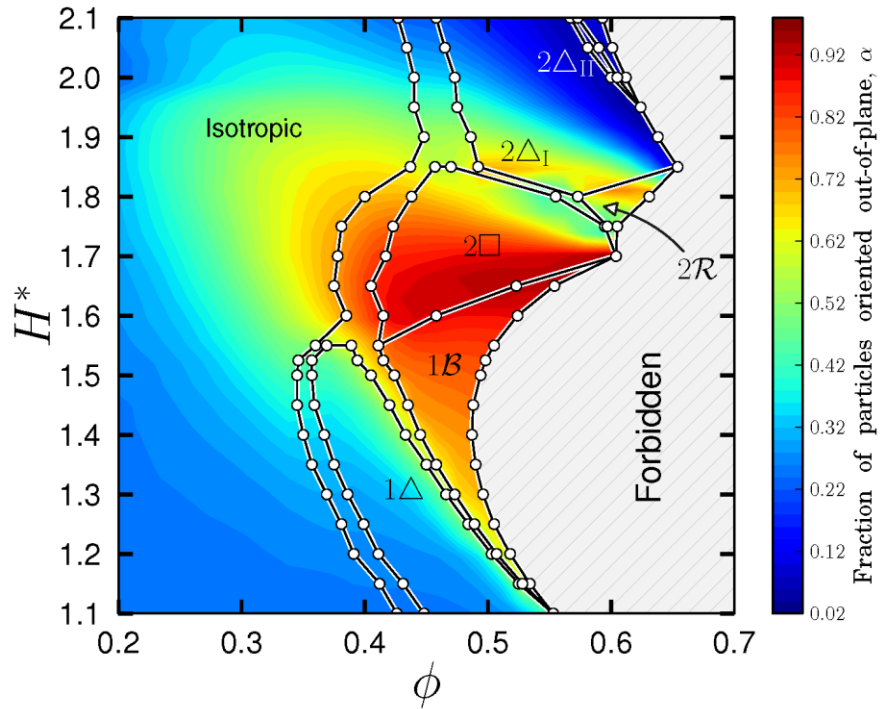


**Figure 3.6.**  $H^*$ - $\phi$  Phase diagram of binary hard peanuts and sphere from Monte Carlo simulations. The color map represents the fraction of peanuts oriented out-of-plane. The forbidden region indicates parameters where the maximum packing fraction of hard dimers under confinement is exceeded. The densest crystal structures correspond to the boundary of forbidden states calculated using the method of Fillion et al.<sup>53</sup> at the reduced pressure of  $10^6$ .

The phase diagram and phase boundaries look very similar to those exhibited by hard spheres<sup>22-23</sup> and hard peanuts<sup>41</sup>. This sloped phase boundary indicates that the 2 $\square$  can have lower density than the 1 $\beta$  phase at certain heights.

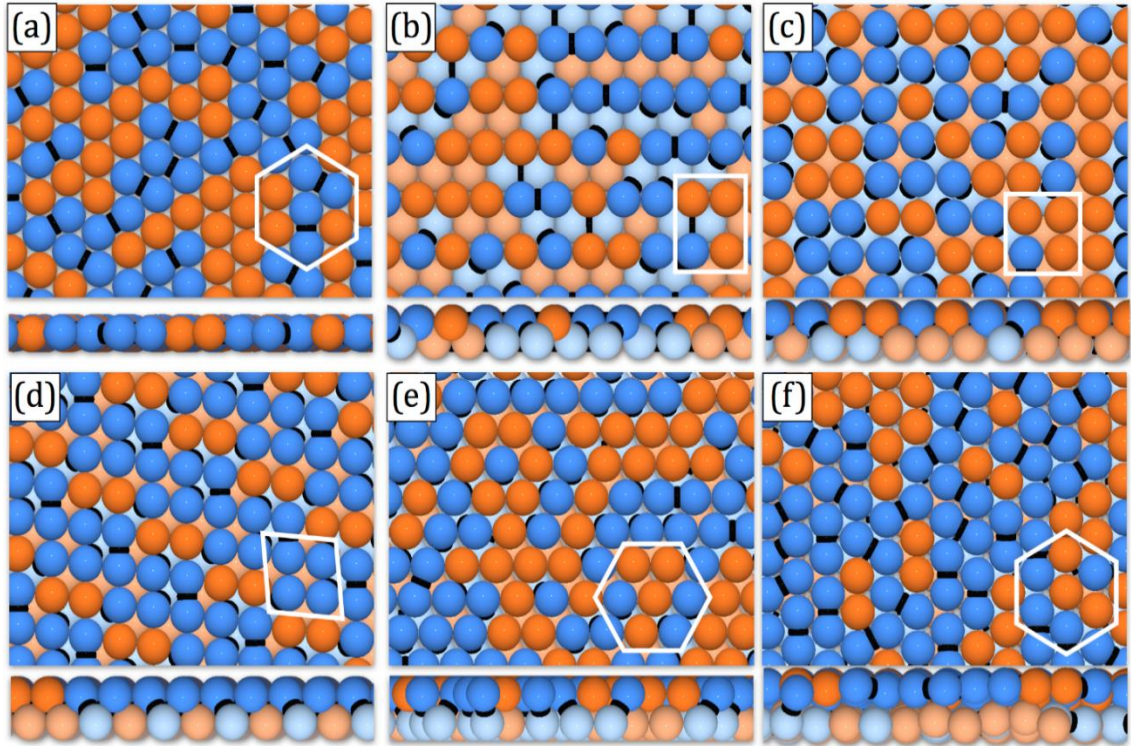


**Figure 3.7.** Representative areas of stable phase configurations observed in the phase diagram for the binary system of hard peanuts and spheres. (a) hexagonal monolayer ( $1\Delta$ ), (b) buckled state ( $1\beta$ ), (c) bilayer square  $2\square$ , (d) bilayer hexagonal type I ( $2\Delta_I$ ), (e) bilayer hexagonal type II ( $2\Delta_{II}$ ). Each panel shows x-y view (top) and x-z view (bottom). Lightly shaded lobes lie in the bottom layer. Peanuts are colored in blue while spheres are colored in orange. Spherical lobes in the upper layer are denoted with a darker hue.

The  $1\Delta$  structure is observed for values of  $1.05 \leq H^* \leq 1.55$  and is described by the arrangement of the spheres and dimer lobes on a triangular lattice, but with the dimers' center of mass randomly distributed (Fig. 3.7a). The major axis of each peanut is oriented along three directions of the underlying triangular lattice. The FFT (fast Fourier transform) in Fig. 3.8a is consistent with the plane group  $p6mm$ . The  $1\beta$  phase with linear buckling is observed at high densities and for values of  $1.10 \leq H^* \leq 1.70$ . The color map shown in the phase diagram of Fig. 3.6 denotes the fraction  $\alpha$  of particles oriented out-of-plane. The  $1\beta$  phase has plane group symmetry  $p2mm$  and is characterized by large values of  $\alpha$ , indicating that

the particles reorient out-of-plane as the gap height is increased (Fig. 3.7b). The snapshot of the ideal  $1\beta$  phase illustrates that each peanut particle can only have four possible orientations (not taking into account particles in-plane oriented). These possible orientations correspond to the cases in which one of the peanut lobes is located on the rectangular lattice, while the other lobe is in the interstitial site in the plane above (or below), similar to the  $2\square$  phase with a square lattice. The  $2\square$  phase was observed in the gap height range  $1.55 \leq H^* \leq 1.85$ , and has plane group symmetry  $p4mm$ . Close to the boundary with the  $2\Delta$  region the population of peanuts oriented in-plane increases substantially. The rhombic phase ( $2R$ ) is predicted at high density as an intermediate phase between  $2\square$  and  $2\Delta$ . This rhombic structure has been observed experimentally in the assembly of hard spheres,<sup>53</sup> but was not found for the mixture of peanuts and spheres because the ability to achieve such dense packings is likely precluded by kinetic restrictions. Bilayer hexagonal structures are observed for  $H^* \geq 1.80$ , with the  $2\Delta_I$  and  $2\Delta_{II}$  phases being identifiable for  $H^* < 1.85$  and  $H^* > 1.95$ , respectively. The transition between bilayer hexagonal phases is marked by the smooth reorientation of peanuts to align in-plane as indicated by the changes in  $\alpha$  parameter (Fig. 3.6). The snapshots of the ideal  $2\Delta_I$  and  $2\Delta_{II}$  phases are shown in Fig. 3.7e, f and their  $p6mm$  plane group symmetry is confirmed in the structure factor images in Fig. 3.8. The imperfections of the  $2\Delta_I$  phase structure can be visualized by its Voronoi construction (Fig. 3.5e), which shows irregular polygons having slight departures from hexagonal edges.

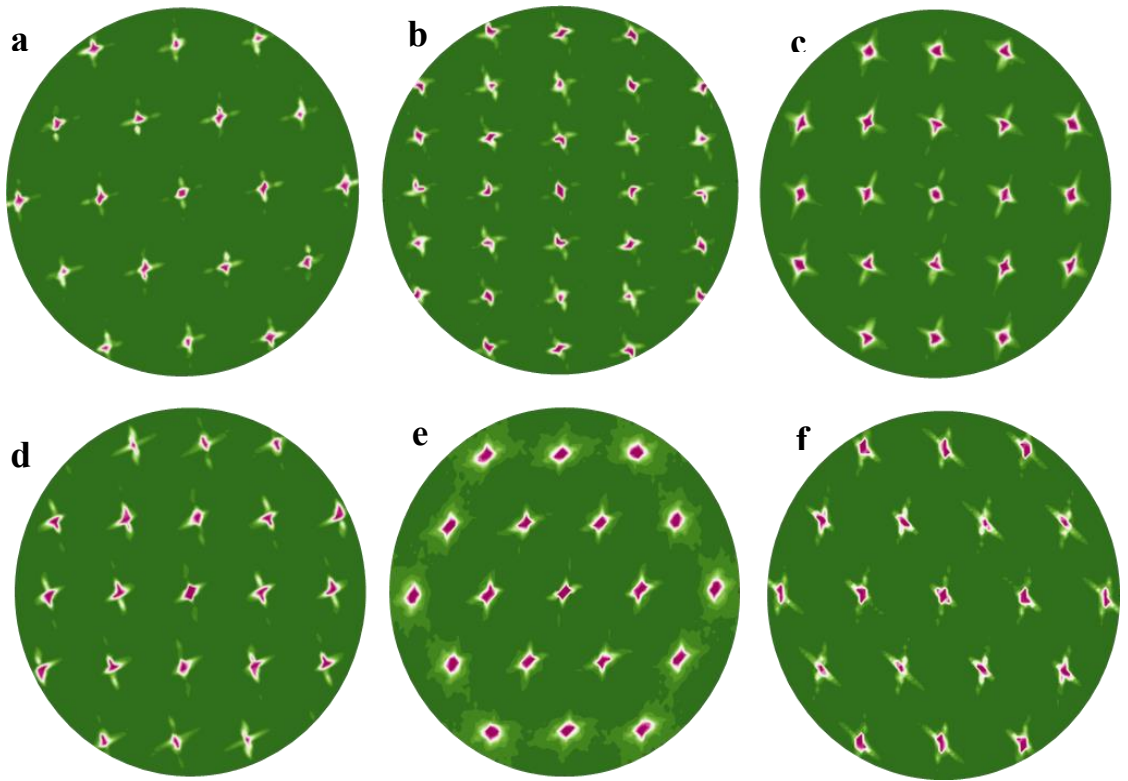


**Figure 3.8.** Simulated structure factors for the binary system of peanuts and spheres. (a) hexagonal monolayer ( $1\Delta$ ), (b) buckled state ( $1\beta$ ), (c) bilayer square  $2\Box$ , (d) bilayer hexagonal type I ( $2\Delta_I$ ), (e) bilayer hexagonal type II ( $2\Delta_{II}$ ).

Whether there was a difference in the orientation behavior of the peanuts due to the presence of spheres is explored in Figure 3.9. The phase diagram is plotted with a color map that reflects the difference between the fraction of dimers out-of-plane in the mixture and the fraction of dimers out-of-plane in the single component dimer system. The differences are essentially negligible between the two, which indicates that the spheres do not influence the orientation behavior. The boundaries of the pure dimer system are essentially the same as those in the mixture (i.e., the spheres do not have an effect on the phase boundaries).

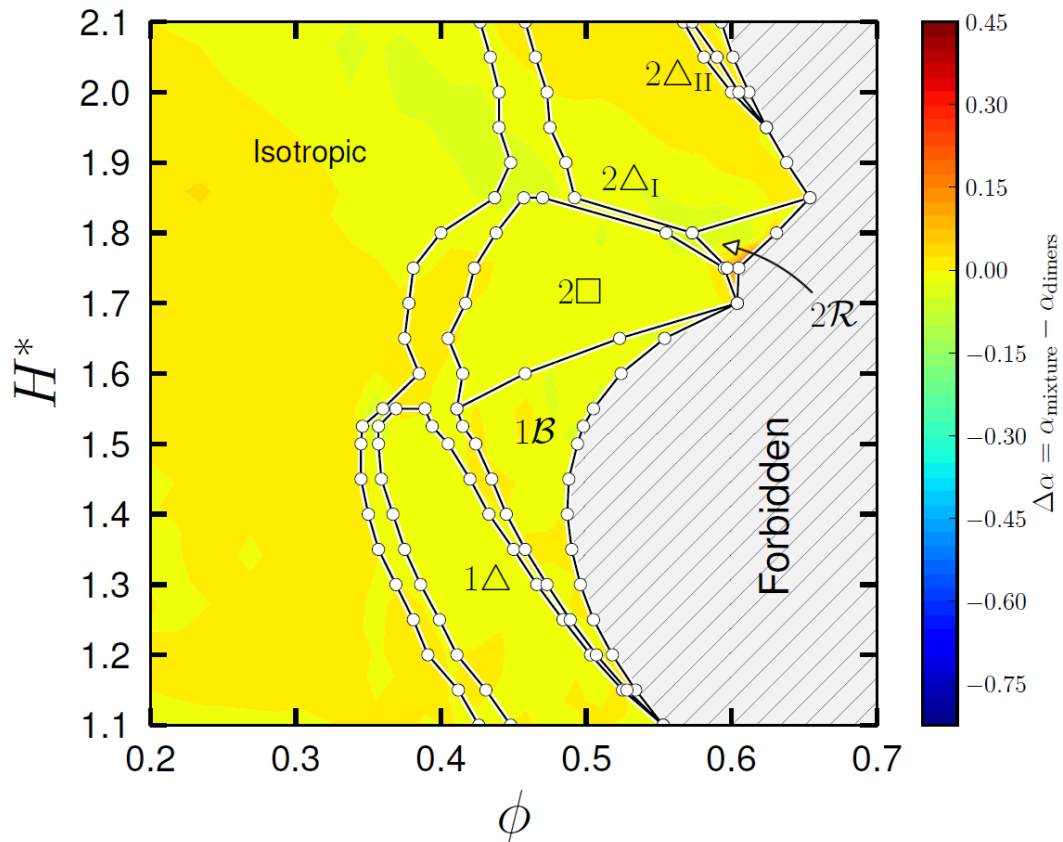


**Figure 3.9.**  $H^*$ - $\phi$  Phase diagram of binary hard peanuts and sphere from Monte Carlo simulations. The color map represents the difference in the fraction of peanuts oriented out-of-plane for the mixture and pure dimers systems.

To confirm quantitatively that the binary phases are substitutionally disordered, we measured the average local composition of spheres which are nearest neighbors of a sphere and compared this value to the global composition. In the case of the simulations these values are essentially the same irrespective of the degree of confinement and phase. The percent difference between local and global compositions for the spheres was 15%. For the experimental phases, the largest percent difference is 13% and taken together the results suggest nearly ideal mixing.

### **3.5 Conclusion**

Binary mixtures of lattice-compatible shapes were allowed to self-organize in mono- and bi-layers using wedge cell confinement. Spheres and peanuts of the same material and with hollow morphology were prepared so that the particles remained well-mixed during assembly. Five distinct phases were experimentally observed between the monolayer and bilayer arrangements. The ordered phases observed for increasing gap height followed the sequence  $1\Delta \rightarrow 1\beta \rightarrow 2\Box \rightarrow 2\Delta_I \rightarrow 2\Delta_{II}$ . This progression is similar to that of hard spheres with the added feature of now having a distribution of orientations for the major axis of the dimers. The binary assemblies show substitutional disorder on the lattices defining their lobe positions and degeneracy in dimer orientations. Monte Carlo simulations of perfectly shaped mixtures were performed to establish the equilibrium phases and the phase diagram as a function of system density and degree of confinement. While the phases found experimentally are consistent with the

phase diagram found via simulation, the high density rhombic phase present in the latter was not observed experimentally due to kinetic frustration.

Recent synthesis developments have produced a rich library of anisotropic particles that are promising for the formation of substitutionally disordered colloidal phases including spheres and cut-spheres, hexagonal prisms and hexagonal rods, and cubes and tetragonal parallelepipeds. Such substitutionally disordered phases satisfy the structure factor criterion for bandgap formation, that  $S(k)$  tends toward zero as  $|k|$  approaches zero. This criterion reveals that certain types of structural disorder support photonic properties rather than prohibit them. In addition, it provides an overarching rationale for photonic properties in hyperuniform disordered structures,<sup>54-55</sup> icosahedral quasicrystals,<sup>57</sup> and rotator mesophases.<sup>58</sup> Substitutionally disordered phases lie at the forefront of manipulating disorder for colloid-based photonics.

## REFERENCES

1. D. Graham-Rowe, *Nat. Photonics*, 2008, **2**, 204.
2. A. Arsenault, G. A. Ozin, G. Von Freymann, US Pat. 2014. 8676016.
3. A. C. Arsenault, D. P. Puzzo, I. Manners, G. A. Ozin, *Nat. Photonics*, 2007, **1**, 468.
4. G. von Freymann, V. Kitaev, B. V. Lotsch, G. A. Ozin, *Chem. Soc. Rev.*, 2013, **42**, 2528.
5. A. M. Kalsin, M. Fialkowski, M. Paszewski, S. K. Smoukov, K. J. Bishop, B. A. Grzybowski, *Science*, 2006, **312**, 420.
6. K. J. Bishop, C. E. Wilmer, S. Soh, B. A. Grzybowski, *Small*, 2009, **5**, 1600.
7. K. P. Herlihy, J. Nunes, J. M. DeSimone, *Langmuir*, 2008, **24**, 8421.
8. A. Yethiraj, A. van Blaaderen, *Nature*, 2003, **421**, 513.
9. M. E. Leunissen, C. G. Christova, A. P. Hynninen, C. P. Royall, A. I. Campbell, A. Imhof, M. Dijkstra, R. van Roij, A. Van Blaaderen, *Nature*, 2005, **437**, 235.
10. J. Ge, Y. Hu, T. Zhang, Y. Yin, *J. Am. Chem. Soc.*, 2007, **129**, 8974.
11. T. Ding, K. Song, K. Clays, C. H. Tung, *Adv. Mater.*, 2009, **21**, 1936.
12. X. Cheng, J. H. McCoy, J. N. Israelachvili, I. Cohen, *Science*, 2011, **333**, 1276.
13. K. Zhao, T. G. Mason, *Phys. Rev. Lett.*, 2008, **101**, 148301.
14. P. Pieranski, L. Strzelecki, B. Pansu, *Phys. Rev. Lett.*, 1983, **50**, 900.
15. A. B. Fontecha, T. Palberg, H.J. Schöpe, *Phys. Rev. E*, 2007, **76**, 050402.
16. S. Naser, C. Bechinger, P. Leiderer, T. Palberg, *Phys. Rev. Lett.*, 1997, **79**, 2348.
17. B. Pansu, P. Pieranski, P. Pieranski, *J. Phys.*, 1984, **45**, 331.

18. F. Ramiro-Manzano, F. Meseguer, E. Bonet, I. Rodriguez, *Phys. Rev. Lett.*, 2006, **97**, 028304.
19. F. Ramiro-Manzano, E. Bonet, I. Rodriguez, F. Meseguer, *Soft Matter*, 2009, **5**, 4279.
20. Y. Han, Y. Shokef, A. M. Alsayed, P. Yunker, T. C. Lubensky, A. G. Yodh, *Nature*, 2008, **456**, 898.
21. S. Naser, T. Palberg, C. Bechinger, P. Leiderer, *Optical Methods and Physics of Colloidal Dispersions*, 1997, 194.
22. A. Fortini, M. Dijkstra, *J. Phys.: Condens. Matter.*, 2006, **18**, L371.
23. M. Schmidt, H. Löwen, *Phys. Rev. Lett.*, 1996, **76**, 4552.
24. M. Schmidt, H. Löwen, *Phys. Rev. E*, 1997, **55**, 7228.
25. R. Zangi, S. A. Rice, *Phys Rev. E*, 2000, **61**, 660.
26. R. Zangi, S. A. Rice, *Phys. Rev. E*, 2000, **61**, 671.
27. M. H. Kim, S. H. Im, O. O. Park, *Adv. Mater.*, 2005, **17**, 2501.
28. K. P. Velikov, C. G. Christova, R. P. Dullens, A. van Blaaderen, *Science*, 2002, **296**, 106.
29. N. Hunt, R. Jardine, P. Bartlett, *Phys. Rev. E*, 2000, **62**, 900.
30. M. Khaldikar, F.A. Escobedo, *J. Chem. Phys.*, 2012, **137**, 194907.
31. J. A. Millan, D. Ortiz, G. van Anders, S. C. Glotzer, *ACS nano*. 2014, **8**, 2918.
32. D. V. Talapin, E. V. Shevchenko, M. I. Bodnarchuk, X. Ye, J. Chen, C. B. Murray, *Nature*, 2009, **461**, 964.

33. X. Zeng, G. Ungar, Y. Liu, V. Percec, A. E. Dulcey, J. K. Hobbs, *Nature*, 2004, **428**, 157.
34. A. Takano, W. Kawashima, A. Noro, Y. Isono, N. Tanaka, T. Dotera, Y. Matsushita, *J. Polym. Sci., Part B: Polym. Phys.*, 2005, **43**, 2427.
35. A. C. Stelson, W. A. Britton, C. M. Liddell Watson, *J. Appl. Phys.*, 2017, **121**, 023101.
36. S. Sacanna, W. T. M. Irvine, P. M. Chaikin, D. J. Pine, *Nature*, 2010, **464**, 575.
37. Y. Wang, Y. Wang, X. Zheng, G. R. Yi, S. Sacanna, D. J. Pine, M. Weck, *J. Am. Chem. Soc.*, 2014, **136**, 6866.
38. J. W. J. de Folter, P. Liu, L. Jiang, A. Kuijk, H. E. Bakker, A. Imhof, A. Van Blaaderen, J. Huang, W. K. Kegel, A. P. Philipse, A. V. Petukhov, *Part. Part. Syst. Charact.*, 2015, **32**, 313.
39. T. Paik, C. B. Murray, *Nano Lett.*, 2013, **13**, 2952.
40. W. Hume-Rothery, H. M. Powell, *Zeitschrift für Kristallographie-Crystalline Materials*, 1935, **91**, 23.
41. K. Muangnapoh, C. Avendaño, F. A. Escobedo, C. M. L. Watson, *Soft matter*, 2014, **10**, 9729.
42. K. W. Wojciechowski, *Phys. Rev B*, 1992, **46**, 26.
43. D. Shindo, G. S. Park, Y. Waseda, T. Sugimoto, *J. Colloid Interface Sci.*, 1994, **168**, 478.
44. N. Sasaki, Y. Murakami, D. Shindo, T. Sugimoto, *J. Colloid Interface Sci.*, 1999, **213**, 121.

45. S. H. Lee, S. J. Gerbode, B. S. John, A. K. Wolfgang, F. A. Escobedo, I. Cohen, C. M. Liddell, *J. Mater. Chem.*, 2008, **18**, 4912.
46. R. A. Caruso, A. Susha, F. Caruso, *Chem. Mater.*, 2001, **13**, 400.
47. S. H. Lee, C. M. Liddell, *Small*, 2009, **5**, 1957.
48. K. W. Wojciechowski, *Phys. Lett. A*, 1987, **122**, 377.
49. D. Leith, *Aerosol Sci. Technol.*, 1987, **6**, 153.
50. J. S. McNown, J. Malaika, *Eos, Trans. Am. Geophys. Union*, 1950, **31**, 74.
51. Y. Han, Y. Shokef, A. M. Alsayed, P. Yunker, T. C. Lubensky, A. G. Yodh, *Nature*, 2008, **456**, 898.
52. I. V. Schweigert, V. A. Schweigert, F. M. Peeters, *Phys. Rev. B*, 1999, **60**, 14665.
53. L. Filion, M. Marechal, B. van Oorschot, D. Pelt, F. Smalenburg, M. Dijkstra, *Phys. Rev. Lett.*, 2009, **103**, 188302.
54. W. Man, M. Florescu, E. P. Williamson, Y. He, S. R. Hashemizad, B. Y. C. Leung, D. R. Liner, S. Torquato, P. M. Chaikin, P. J. Steinhardt, *Proc. Natl. Acad. Sci.*, 2013, **110**, 15886.
55. W. Man, M. Florescu, K. Matsuyama, P. Yadak, G. Nahal, S. Hashemizad, E. Williamson, P. Steinhardt, S. Torquato, P. Chaikin, *Opt. Express*, 2013, **21**, 19972.
56. W. Man, M. Megens, P. J. Steinhardt, P. M. Chaikin, *Nature*, 2005, **436**, 993.
57. A. C. Stelson, C. Avendano, C. M. Liddell Watson, *J. Appl. Phys.*, 2016, **119**, 23110.
58. M. Marechal, M. Dijkstra, *Phys. Rev. E*, 2008, **77**, 061405.
59. T. Sugimoto, M. M. Khan, A. Muramatsu, *Colloids and Surf., A*, 1993, **70**, 167.

## CHAPTER 4

### SUBSTITUTIONALLY DISORDERED PHASES FROM BINARY SPHERE AND CUT- SPHERE MIXTURES UNDER CONFINEMENT

#### 4.1 Abstract

Binary mixtures of spheres and cut-spheres are assembled into substitutionally disordered phases using wedge-cell confinement. The studies are motivated by our recent photonic band calculations for sphere and cut sphere motifs, which show isotropic photonic band gaps for rotator phases with substitutional disorder. Sacrificial particles are used to template the growth of dye-labeled silica shells. The hollow morphology and complementary feature sizes mitigate density and size mismatch between the particle populations so that phase separation is minimized. Wedge confinement allows the systematic observation of phase transitions as a function of height and density. Using confocal microscopy, eight distinct phases are found between one and two integral layers following the progression  $1\Delta_r(\text{hexagonal}) \rightarrow 1S_I(\text{side}) \rightarrow 1S_{II}(\text{rotator}) \rightarrow 1B(\text{buckled}) \rightarrow 2\Box(\text{square}) \rightarrow 2\Delta_r(\text{hexagonal}) \rightarrow 2S_I(\text{side}) \rightarrow 2S_{II}(\text{rotator})$ . This descriptive sequence is similar to that of pure cut-spheres with the addition of substitutional disorder on the lattices. The substitutional disorder is rationalized by the Hume-Rothery rules for atomic systems and compounds. These studies are motivated by our recent photonic band calculations for sphere and cut sphere motifs, which show isotropic photonic band gaps for rotator phases with substitutional disorder.

---

To be published as: K. Muangnapoh, C. Avendano, F. A. Escobedo, C. M. L. Watson.  
*J. Mater. Chem.*, submitted (2017.)

## 4.2 Introduction

An emerging theme in colloid science is applying complex particles in synthetic materials for photonic properties such as photonic band gaps, negative refraction, slow light (i.e., low group velocity), light confinement, etc. There has been much progress in the synthesis and microfabrication of particles with anisotropic shapes, interacting patches, amphiphilicity and magnetic anisotropy.<sup>1-</sup>

8

Binary colloidal mixtures have also been the subject of great interest, since they spontaneously undergo complex ordering at the mesoscale and have the potential to vastly increase the range of structures that can be self-assembled<sup>9-13</sup>. Several studies have established the promise of assembly in binary systems. For example, it is well known that size-binary mixtures of colloidal spheres form crystal structures determined by the size ratio, concentrations of large (L) and small (S) particles and the total packing fraction.<sup>13</sup> When the particle populations have small, opposite charges, a rich variety of phases is predicted including, NaCl, CsCl, LS<sub>8</sub>, LS<sub>6</sub>, LS<sub>4</sub> etc. and some of these have been demonstrated experimentally.<sup>14-15</sup> Other size-binary phases have been prepared using confined convective assembly<sup>16</sup> and layer-by-layer vertical deposition<sup>17</sup>. For these approaches, a layer of large particles is deposited which guides the subsequent layer of small particles into the template. The packing of the large and small spheres is additionally controlled by the drying rate or substrate withdrawal rate and the templating effect.

Shape-binary colloidal mixtures of regular polygons are predicted to form Archimedean tilings, stabilized by enthalpic shape-specific and edge-specific patches.<sup>18-19</sup> These structures can support isotropic photonic bandgaps because of high rotational symmetry and also have promising refraction properties.<sup>20-22</sup> However, challenges for the fabrication of shape-binary mixtures include the synthesis of lattice-compatible shapes and overcoming phase separation due to differences in density, size and shape of the particle populations. Recently, lock and key colloids have been prepared from colloidal particles with spherical cavity and complementary spheres resulting in site-specific assembly via depletion interactions.<sup>23</sup> Mixtures of cubes and spheres were assembled using 1D confinement in microtubules and thermal switching between the isotropic and ordered state was demonstrated.<sup>24</sup> The former studies did not observe the formation of self-organized films, but only of clusters and chains. Other studies have involved the binary assembly of nanoparticles; for instance, tripod and rhombus building blocks assemble into monolayers through face-to-face stacking.<sup>25</sup> However, these structures have a scale that is unsuitable for photonic applications.

Most studies of binary mixtures have focused on the assembly of crystalline solids. Recently, new concepts have emerged for predicting structures that may support photonic band gaps, namely the arrangements should have a structure factor  $S(k)$  tending toward zero as  $|k|$  approaches zero. This criteria is met by diverse arrangements such as hyperuniform disordered structures,<sup>26-27</sup> continuous random networks,<sup>28</sup> icosahedral quasicrystals,<sup>29</sup> and Archimedean

tilings.<sup>30-31</sup> Therefore, periodicity is not required for the formation of strong photonic properties. Recently, isotropic band gaps have been reported for rotator mesophases of cut-spheres. Such band gaps are desirable for free-form waveguides,<sup>32</sup> flexible cavity designs,<sup>33</sup> and out-coupling across all incident angles from LEDs.<sup>34</sup>

Here, we investigate the self-assembly of substitutionally disordered phases from shape-binary building blocks. These studies are motivated by our recent 2D photonic band calculations for sphere and cut sphere motifs, which show isotropic photonic band gaps for rotator phases with substitutional disorder (Figure 4.1). In the current report, sacrificial particles are used to template the growth of dye-labeled silica shells.<sup>35</sup> The hollow morphology and complementary feature sizes mitigate density and size mismatch between the particle populations so that phase separation is minimized. The hollow shells also make the particles suitable for fluorescent imaging using confocal laser scanning microscopy and reduce scattering from the core-shell interfaces. The shape binary mixtures are assembled under wedge-cell confinement, where phase transformations are driven entropically as a function of volume fraction and cell height.<sup>36</sup> The spheres and cut spheres (cut-fraction,  $\chi = 0.75$ ) used in this study are lattice-compatible, analogous to atomic systems, as described by the Hume-Rothery rules for isomorphous phases. In particular, the size mismatch between the shape populations is less than 15%, the particle interactions are similar (i.e., hard sphere and hard cut sphere), and spheres and cut spheres tile many of the same phases with gap height. Confocal microscopy and image analysis revealed

eight distinct phases between 1 and 2 integral layers. Specifically, the arrangements are substitutionally disordered tilings of the corresponding cut-sphere structure<sup>37</sup> along the descriptive sequence  $1\Delta_r \rightarrow 1S_I \rightarrow 1S_{II} \rightarrow 1B \rightarrow 2\Box \rightarrow 2\Delta_r \rightarrow 2S_I \rightarrow 2S_{II}$ , where the subscript r represents random cut-sphere orientations ‘face up’ and ‘face down’. For  $1S_I$  and  $2S_I$  states, the cut-sphere axis of spherical symmetry reorients parallel rather than perpendicular to the plane of the substrate, while for the  $1S_{II}$  and  $2S_{II}$  states the cut-spheres freely rotate.

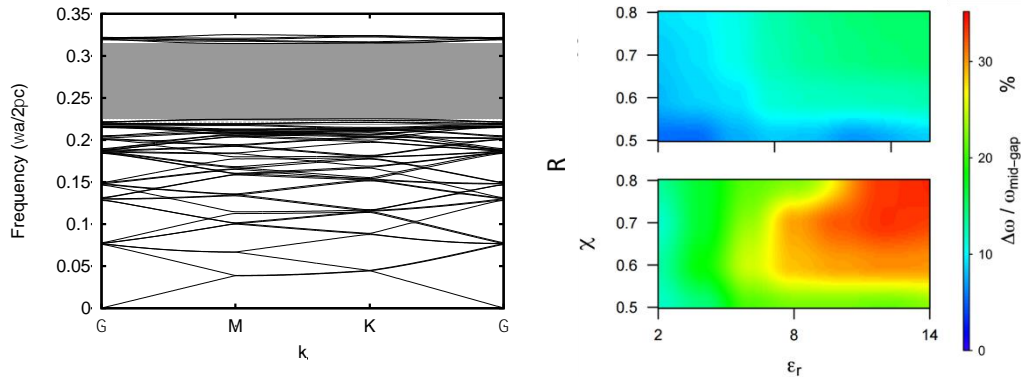


**Figure 4.1.** a) Transverse magnetic (TM) photonic bandgaps in systems of random binary mixtures of circular rods and cut-rods decorating a hexagonal lattice. b) Contour plot of the TM band gap size as a function of cut-fraction,<sup>45</sup> basis spacing and dielectric constant of the rods and cut-rods. We generated supercells of rotator crystals of cut-rods, and substituted a Gaussian distribution (mean 50% cut-rods) of randomly selected sites with rods of equivalent radius. Large (maximum gap-to-midgap ratio of 34.5%), isotropic photonic bandgaps were found to be insensitive to the spatial distribution of rods. A wide range of dielectric contrasts support these photonic bandgaps (2-14).

## 4.3 Method

### 4.3.1 Particle synthesis

Cut-sphere particles were prepared using a two-stage seeded polymerization. Polystyrene seed particles  $\sim 0.5 \mu\text{m}$  in size (5% CV, coefficient of variation) were synthesized using emulsion polymerization. In brief, 146 mg sodium dodecyl

sulfate (Fisher Biotech) emulsifier and 133 mg potassium persulfate (Sigma Aldrich) initiator were dissolved in a medium of 100 mL absolute ethanol and 40 mL deionized (DI) water via stirring in a 250 mL glass bottle. 6 mL of the monomers [styrene (99%, Sigma-Aldrich) and 0.18 mL divinylbenzene (55%, Aldrich)] were injected into the system. The reaction vessels were sealed and contents were stirred at 70°C (350 rpm) overnight on a magnetic stirrer. The resulting product was cooled in a running water bath and used without further purification.

The seed particles were swollen with monomer and polymerized to prepare cut-spheres. A 0.5 g amount of seed particles in suspension was centrifuged to obtain a pellet. The compact was resuspended via sonication with 5 mg hydroquinone (99%, Acros) in 2 mL polyvinyl alcohol (PVA, 87–89% hydrolyzed, Sigma-Aldrich) solution of concentration 1% w/v in DI water. In a 50 mL beaker, 75 mg 2,20-azobis(2.4-dimethyl valeronitrile) (V-65, Wako) initiator was dissolved in 2.5 mL of monomer (30% (v/v) DVB/styrene). 5 mL of PVA solution was added and the combination was homogenized for 1 minute. The homogenized mixture, modified suspension of seed particles, and an additional 5 mL PVA solution were agitated in a 50 mL centrifuge tube overnight on a tumbling rack to swell the particles. The contents were transferred to 25 mL reaction bottles, purged with nitrogen gas for 1 minute and were capped prior to polymerization overnight in a shaker bath at 70°C and 120 rpm.

Polystyrene spheres with diameter 1.5  $\mu\text{m}$  were obtained from Polysciences, Inc. Silica coatings were applied to the cut-spheres and spheres. 110 mg of the cut sphere particles (60 mg of the spheres) were mixed with 9.5 mL of absolute ethanol and 500  $\mu\text{L}$  of 3-(aminopropyl)triethoxysilane. The mixture was tumbled overnight before washing in isopropyl alcohol (IPA.) The sample was redispersed in a mixture of 86 mL IPA and 4 mL of ammonia solution in a round bottom flask. The flask was held a bath at 30° C under 12 W ultrasonication. An aliquot of 30  $\mu\text{L}$  (20  $\mu\text{m}$ ) tetraethylorthosilicate (TEOS) were added every two hours for a total of three additions. The reaction was continued for another 14 hours and then washed in IPA. An additional silica layer was applied by adding 75  $\mu\text{L}$  of TEOS to the mixture in 74 mL IPA, 4 mL DI water and 12 mL ammonia under ultrasonication for 5 hours at 30° C. The mixture was washed in IPA followed by in DI water.

#### **4.3.2 Deposition of rhodamine-dyed hollow silica shells**

To obtain hollow cut-spheres and spheres, the core-shell particles were calcined using a 2-step temperature profile to prevent broken shells. The sample was placed in an oven at 300 °C for 2 hours and at 550 °C for 5 hours to remove the polystyrene cores. The hollow shells were coated with a dye-labeled silica layer. The dry sample was redispersed in a mixture of 86 ml IPA and 4 mL ammonia solution. An aliquot of 10  $\mu\text{L}$  of Rhodamine B isothiocyanate (Where from) and 20  $\mu\text{L}$  of TEOS was injected into the sample under 4-5 W ultrasonication in a bath at 30° C. After 2 hours, an additional 20  $\mu\text{L}$  TEOS was

injected into the sample and sonication continued overnight. The sample was washed in IPA and DI water and redispersed into  $2.75 \times 10^{-6}$  M polyvinylpyrrolidone (PVP, MW 40000; Sigma-Aldrich) aqueous solution.

#### **4.3.3 Particle assembly**

The wedge confinement cell is comprised of two 22 x 50 mm coverslips on a glass slide. The coverslips were soaked in a 1 M NaOH solution for 15 minutes and washed in DI water. Two rows of cured UV adhesive dots were deposited as spacer between the two coverslips. Pressure was applied to the top coverslip by hand to bond the two coverslips and create zero height separation. The sides of the cell were sealed with UV adhesive leaving the top edge open for particle injection. A solution of PVP in DI water was pipetted into the confinement cell and evaporated in a vacuum desiccator (Sheldon Manufacturing, Model 1400E) to prevent particle sticking to the cell walls. Approximately 50  $\mu$ L of the particle suspension ( $\sim 3\%$ (v/v) cut-sphere particles,  $\sim 3\%$ (v/v) spheres) were injected and the cell was tilted at  $\sim 10^\circ$  to allow the particles to assemble. The regions of interest were imaged after 3-4 days using Zeiss LSM 5 LIVE confocal microscope with 532 nm laser line excitation. Particular phases were observed over a period of time to capture lower density phases. Relative concentrations of spheres and cut-spheres were approximated from the top layer of the assembly.

#### **4.3.4 Photonic simulation**

The photonic band structure for the binary mixture of circular rods and cut-rods was simulated using the MIT Photonic Bands (MPB) software package. A

supercell of the mixture was used for calculating the band diagrams due to the lack of orientational order for the cut-rods after Stelson et. al.<sup>44</sup>

#### 4.4 Result and Discussion

The cut-sphere core particles were synthesized using seeded emulsion polymerization with the dynamic controls of swelling solvent and crosslinking agent (Figure 4.2).<sup>38</sup> Colloidal spheres were purchased from Polysciences. Dye functionalized silica was coated on to the core particles using based-catalyzed hydrolysis of alkoxide. The sacrificial cores were removed using calcination to yield hollow shells. The average size of the cut-spheres was 1.9  $\mu\text{m}$  (major axis) and 1.43  $\mu\text{m}$  (minor axis) with coefficients of variation 6 % and 10 %, respectively. The spheres were 1.69  $\mu\text{m}$  in diameter with 4 % coefficient of variation. he These feature sizes were determined from the measurement of at least 50 hollow particles using scanning electron microscopy.

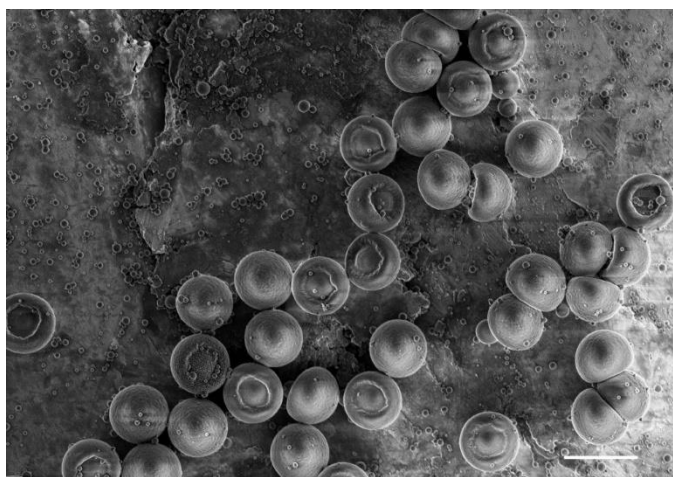


**Figure 4.2.** Scanning Electron Microscopy images of cut-spheres cores prepared by using dynamic controls in seeded emulsion polymerization.<sup>38</sup> Scale bars represent 2  $\mu\text{m}$ .

Cut-spheres and spheres were self-assembled under wedge cell confinement and mesophase formation occurred after a few days. Confocal microscopy z-slices for the binary assemblies are shown for increasing gap height in Figure 4.3. The images are taken at 20 % and 50 % of the layer height, where the tip and cross-section of the particles are apparent, respectively. Time series and z-stack confocal videos are provided in the Supplementary Information. The relative particle populations and the cut-sphere orientations for each phase are shown in Table 4.1.

**Table 4.1. Shape-Binary Phase Composition and Bond-Orientational Order Parameters**

Phase	Gap Height (H*)	Order Parameters		Spheres (%)	Cut-sphere in plane (%)	Cut-sphere out of plane (%)
		$\psi_6$	$\psi_4$			
1 $\Delta_r$	1.08	0.81	0.3	76	23	1
1S <sub>I</sub>	1.12	0.77	0.3	66	3	31
1S <sub>II</sub>	1.36	0.69	0.3	31	-	-
1B	1.63	-	-	81	8	11
2 $\square$	1.80	0.34	0.6	82	12	6
2 $\Delta_r$	2.09	0.68	0.3	34	36	30
2S <sub>I</sub>	2.14	0.62	0.3	40	9	51
2S <sub>II</sub>	2.15	0.62	0.3	20	-	-

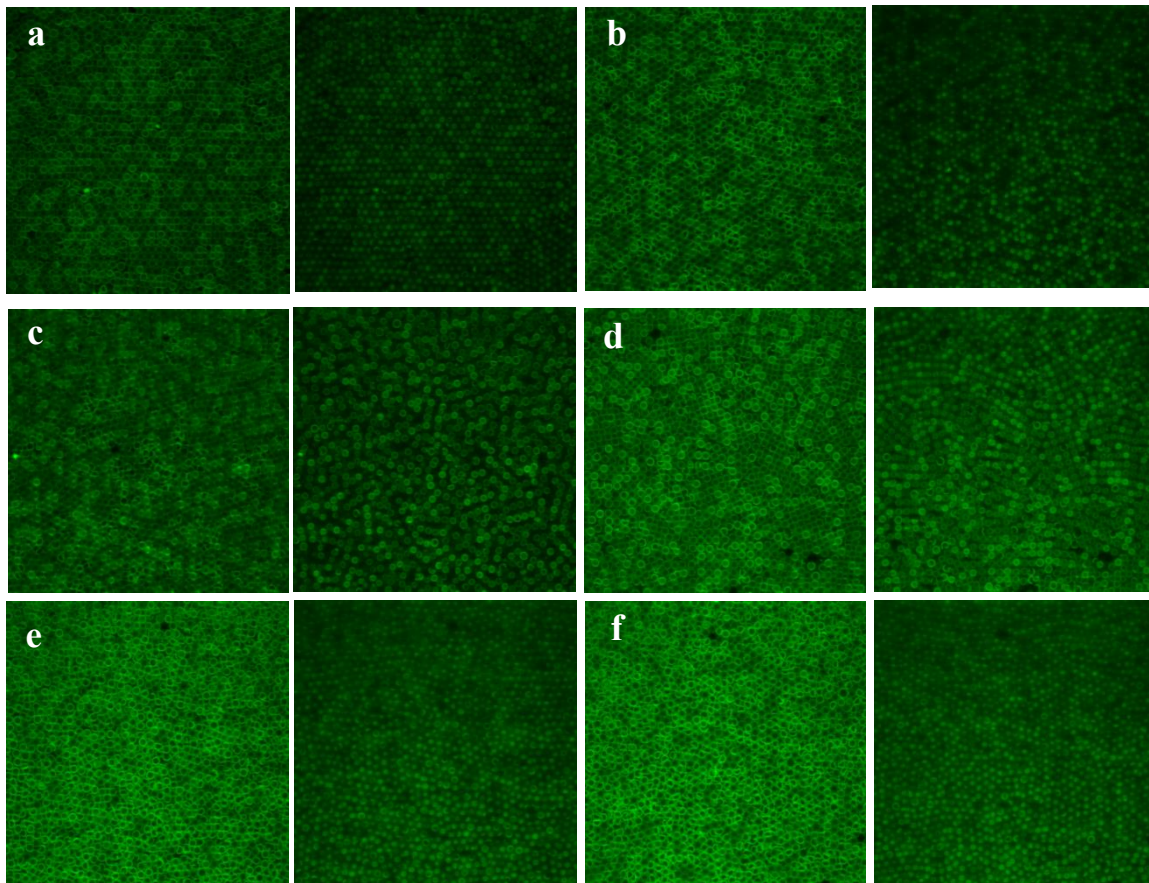


**Figure 4.3.** Confocal Microscopy images for the binary self-assembly of spheres and cut-spheres in confinement cells. The structures observed with increasing gap height are a)  $1\Delta_r$  hexagonal monolayer b)  $1S_f$  hexagonal side monolayer c) 1B buckled state d)  $2\Box$  square bilayer e)  $2\Delta_r$  hexagonal bilayer f)  $2S_f$  hexagonal side bilayer

Figure 4.3 presents confocal images illustrating the series of high density configurations adopted by the shape-binary mixture at increasing cell height. Figure 4.3a shows spheres and cut-spheres in a hexagonal monolayer, where the cut-spheres randomly lay ‘face up’ or ‘face down’. This phase is denoted  $1\Delta_r$ . In general, the Supplemental Video SV1 looks similar to a monolayer of hard spheres since the cross-section of the cut-spheres is circular. The spheres can be distinguished from the cut-spheres by the ‘dimple’ on the cut-sphere particles and by the z-slices, i.e., spheres are the last particles visible as the optical slices go

out of focus at the bottom of the layer. The  $1\Delta_r$  phase is the binary phase observed at the lowest gap height. However, a single phase of cut-spheres was found at even lower gap heights due to the minor axis of the cut-spheres being smaller than the diameter of the spheres.

When the lattice spacing of bulk crystalline structures is incommensurate with gaps imposed by plate separations, particles form intermediate arrangements.<sup>39</sup> Figure 1b presents the  $1S_I$  hexagonal side phase which has characteristic reorientation of the cut-sphere axis of symmetry perpendicular to the substrate. The profiles of the cut spheres in a hindered rotator arrangement are apparent in the z-slice confocal images at  $\sim 50\%$  layer height. Side and buckled phases are intermediates that allow the semi-continuous transitions,  $1\Delta_r \rightarrow 2\Box$  and  $2\Delta_r \rightarrow 3\Box$ . The single component phase of cut-spheres has an oblique lattice, but the  $1S_I$  side phase has local hexagonal symmetry because spheres are the majority population. An additional hexagonal side phase ( $1S_{II}$ ) was observed at lower system density with freely rotating cut-spheres. This rotator mesophase is presented in Supplemental Video SV2.

Figure 4.3c shows the buckled state of spheres and cut-spheres with labyrinthine configuration. The transition from the  $1S_I$  hexagonal side monolayer to the 1B buckled state is marked by the random fluctuations of particles in and out of the focal plane (Supplemental Time Series Video SV3). Buckling of the layers is due to geometric frustration<sup>40</sup> because the gap height is insufficient for the bulk spacing. The 1B structure contains alternating chains of elevated and

depressed lobes with local rectangular symmetry. The ratio of cut-spheres oriented out of plane (Table 4.1) lies between the values for that of the  $1S_I$  and the  $2\Box$ .

The bilayer phase of spheres and cut-spheres with mosaic square symmetry is provided in Figure 4.3d. The  $2\Box$  phase is observed in the cascade of structures before the  $2\Delta_r$  phase because it occupies less height although the  $2\Delta_r$  phase is packed more efficiently. The registry of the layers for the binary system is the same as reported for the single phase systems<sup>37,41</sup>, i.e., particles in the upper layer lie in the interstices of the lower layer.

The  $2\Delta_r$  (Figure 4.3e),  $2S_I$  (Figure 4.3f) and  $2S_{II}$  (Supplemental Video S4) are bilayer phases with hexagonal symmetry. The  $2\Delta_r$  phase has a high percentage of cut-spheres with out-of-plane orientation as compared to the monolayer hexagonal phase. Whether the cut-spheres have in-plane or out-of-plane orientations depends on the fit of the particles with various orientations and composition in the gap height. In  $2S_I$  phase the vast majority of cut-spheres have out-of-plane orientation (side phase). In contrast, the  $2S_{II}$  phase has lower volume fraction and contains freely rotating cut-spheres (rotator phase), similar to the  $1S_{II}$  phase. The registry of the layers is the same as described for the square bilayer phase.

The quality of binary phase order and symmetry were evaluated using bond orientational order parameters, pair-distribution functions (PDFs), Voronoi constructions, fast Fourier Transforms (FFTs) and autocorrelations. The global

bond orientational order parameters for square and hexagonal symmetries ( $\Psi_4$ ,  $\Psi_6$ ) are given by the following:

$$\Psi_n = \frac{1}{N} \left| \sum_{j=1}^N \frac{1}{n_j} \sum_{k=1}^{n_j} \exp(in\theta_{jk}) \right|$$

where,  $\theta_{jk}$  is the angle made by the bond between the spherical site  $j$  and its nearest neighbors with respect to an arbitrary axis and  $n_j$  is the number of nearest neighbors of particles  $j$ . The phases with 6-fold (4-fold) symmetry will have high values of  $\Psi_6$  ( $\Psi_4$ ). The PDF is a measure of the extent of positional order or the correlation distance. The distribution of defects in the binary phases is indicated by the irregularity of the Voronoi polyhedra. Five-sided and seven-sided pairs of polygons signify dislocations and chains of these reveal grain boundaries. FFTs and autocorrelations (Figure 4.4) show spot patterns used to evaluate the symmetry of the binary phases. The buckled state was not characterized quantitatively due to the variety of substructures in the labyrinthine arrangement.

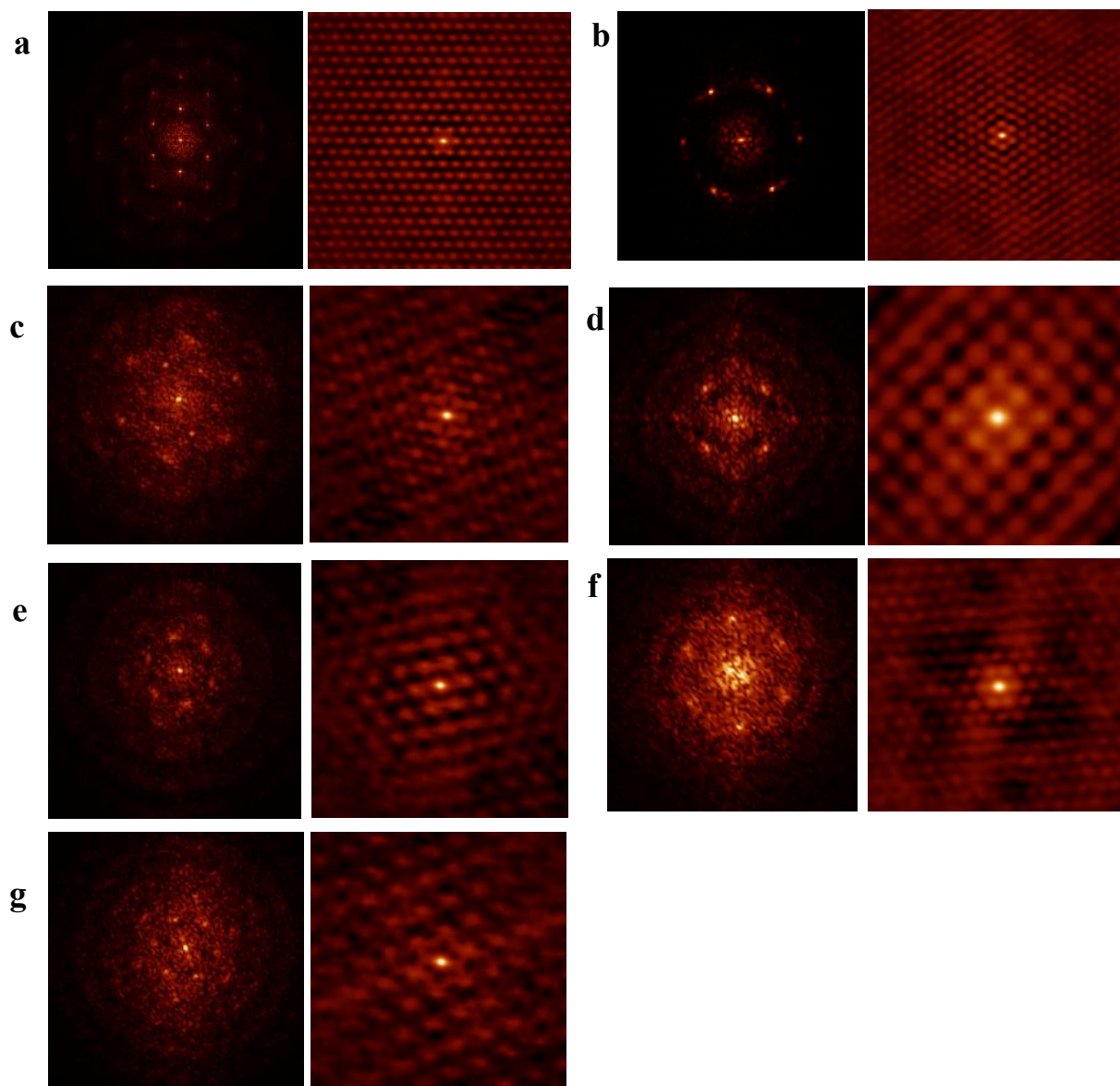


**Figure 4.4.** Fast Fourier Transforms (FFTs) and autocorrelation images showing the symmetry of the binary phases. a)  $1\Delta_r$  hexagonal monolayer b)  $1S_I$  hexagonal side monolayer c)  $1S_{II}$  hexagonal side monolayer d)  $2\Box$  square bilayer e)  $2\Delta_r$  hexagonal bilayer f)  $2S_I$  hexagonal side bilayer g)  $2S_{II}$  hexagonal side bilayer.

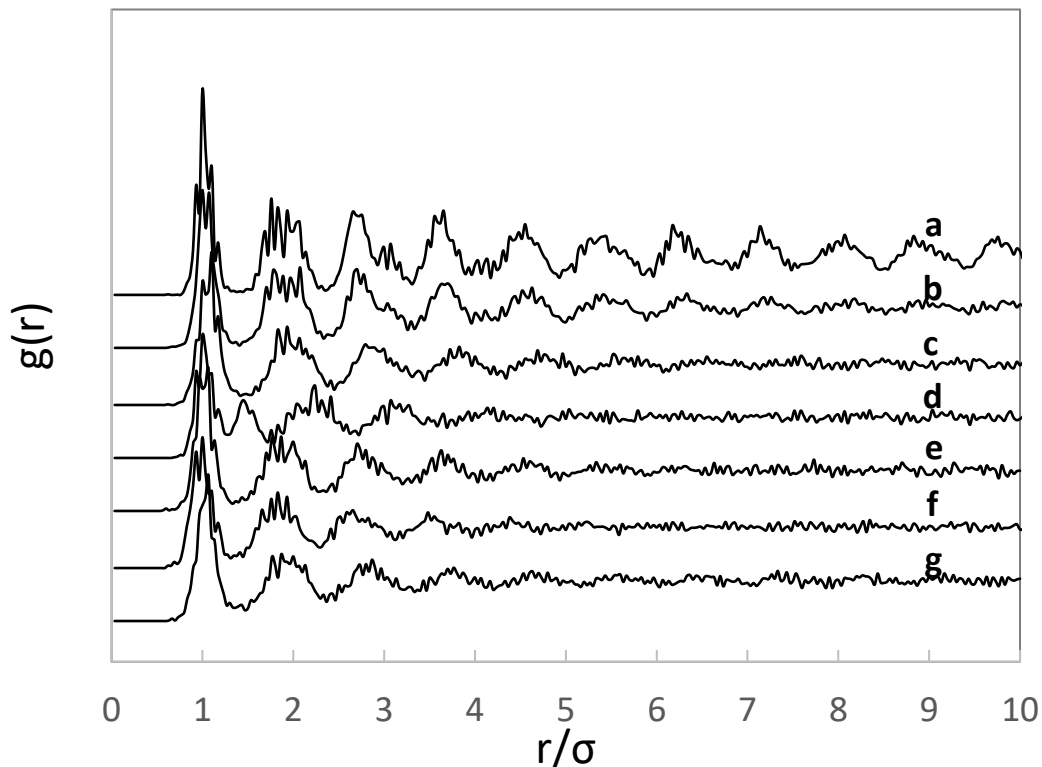


**Figure 4.5.** Pair Distribution Functions for shape-binary phases indicating the correlation distance of positional order. a)  $1\Delta_r$  hexagonal monolayer b)  $1S_I$  hexagonal side monolayer c)  $1S_{II}$  hexagonal side monolayer d)  $2\Box$  square bilayer e)  $2\Delta_r$  hexagonal bilayer f)  $2S_I$  hexagonal side bilayer g)  $2S_{II}$  hexagonal side bilayer

The hexagonal bond orientation order parameter for the  $1\Delta_r$  binary phase ( $\Psi_6 = 0.81$ ) reported in Table 1 compares favorably to the monolayer hexagonal phase of the single component cut-sphere system ( $\Psi_6 = 0.82$ )<sup>38</sup> and single component sphere system ( $\Psi_6 = 0.95$ ).<sup>42</sup> The PDF showed a large correlation length of more than 17 distinct nearest neighbor peaks (Figure 4.5a), suggesting long range positional order. This positional order is corroborated by the large grain sizes present in the Voronoi construction (Figure 4.6a). The FFT and autocorrelation further confirm the hexagonal symmetry and positional order of the phase.

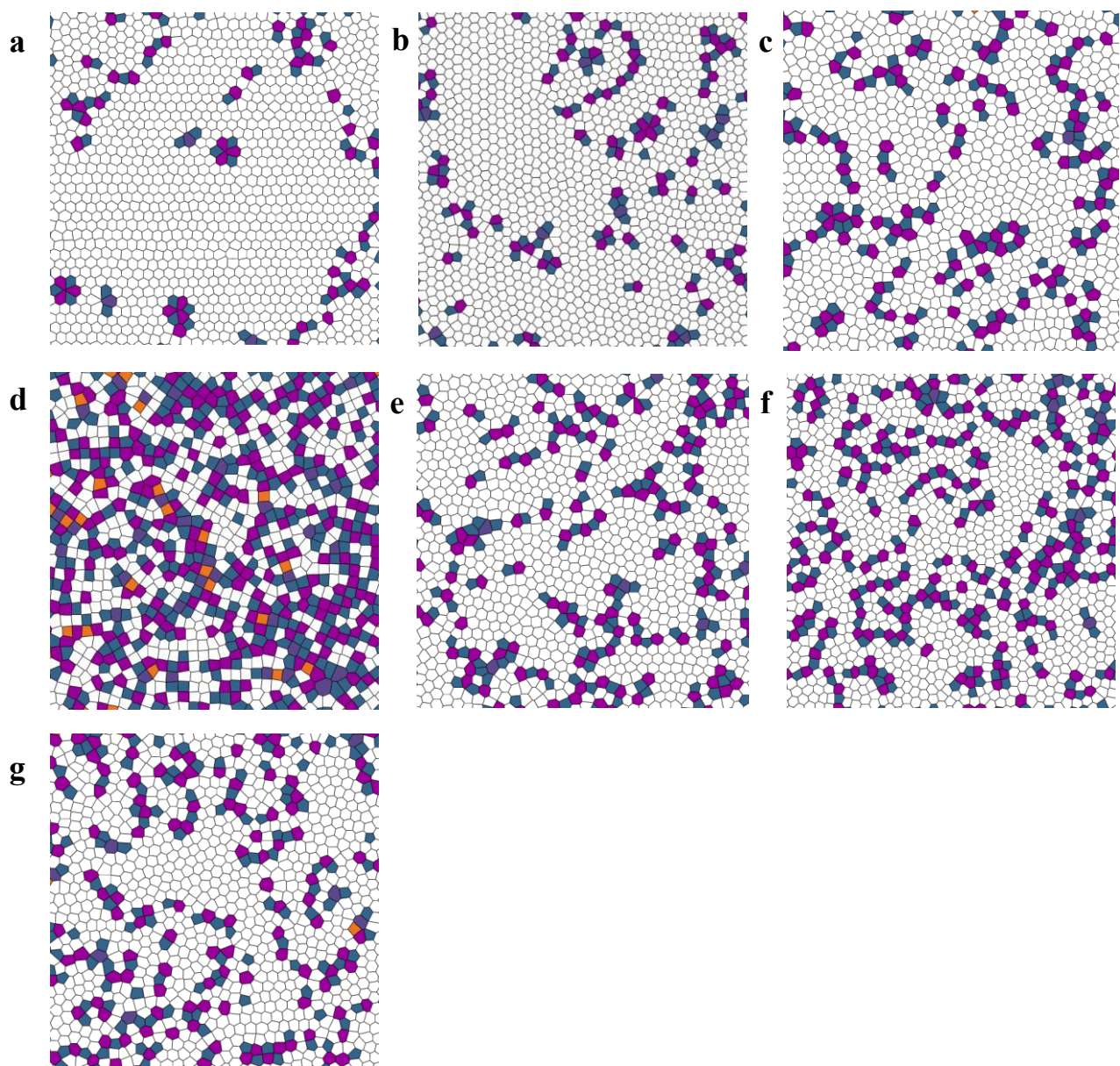


**Figure 4.6.** Voronoi constructions for shape-binary phases of spheres and cut-spheres. a)  $1\Delta_r$  hexagonal monolayer b)  $1S_I$  hexagonal side monolayer c)  $1S_{II}$  hexagonal side monolayer d)  $2\Box$  square bilayer e)  $2\Delta_r$  hexagonal bilayer f)  $2S_I$  hexagonal side bilayer g)  $2S_{II}$  hexagonal side bilayer. Color coding represents the number of nearest neighbor lobes as 4-orange, 5-blue, 6-white, 7-magenta,  $\geq 8$ -indigo.

The monolayer side phases ( $1S_I, 1S_{II}$ ) maintained high hexagonal bond orientational order. In contrast, the reorientation of the cut-spheres out-of-plane in the single component system distorts the lattice from hexagonal to oblique.<sup>37</sup>

The order metrics for the side phase with freely rotating cut-spheres ( $1S_{II}$ ) show decreased bond order and correlation length as compared to the  $1S_I$  phase. This is possibly because the measurements were made on snapshots showing the instantaneous position and orientation of the particles, which varied more for the cut-spheres in the rotator phase.

The  $2\Box$  phase showed characteristic high  $\Psi_4$  bond orientational order parameter (Table 4.1) and four-fold symmetry of the autocorrelation and FFT. The PDF and Voronoi constructions indicated that the correlations in position span a much smaller range for the binary structure than for the single component cut-sphere structure.<sup>37</sup> Additionally, the order metrics show that the bilayer hexagonal phases ( $2\Delta_r, 2S_I, 2S_{II}$ ) are less positionally ordered than the monolayer hexagonal phases. Combinations of spheres and cut-spheres with different orientations being able to fit in similar gap heights allow less regular arrangements for the bilayers.

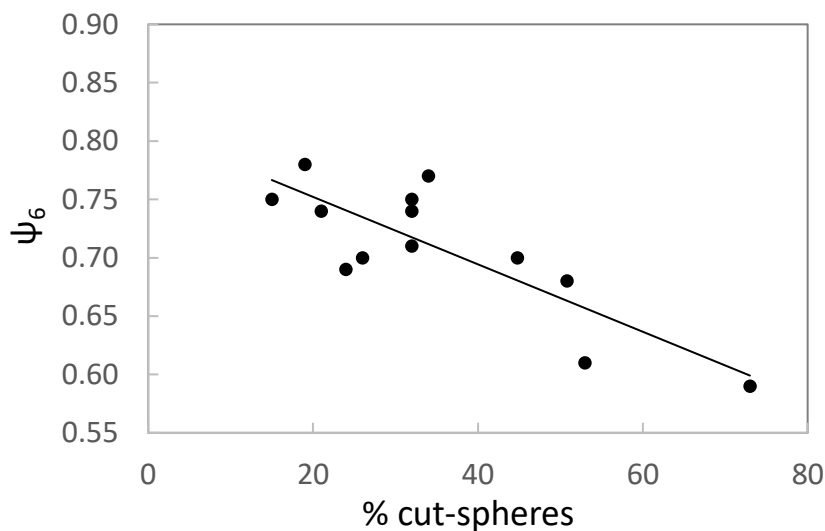


**Figure 4.7.** Hexagonal bond orientational order parameter as a function of composition for the side monolayer phase  $1S_I$ .

The hexagonal bond-orientational order was plotted versus composition (Figure 4.7) to illustrate the effect of system composition on positional order and symmetry. In particular, this study is relevant for side phases, where the assemblies of single component spheres have hexagonal order and those of the single component cut-spheres have oblique order at similar gap heights. As expected, the bond orientational order decreased as the composition of cut-spheres in the binary system increased over the range studied. Approaching the pure cut-sphere system it is possible that the order parameter values will again increase because the oblique and hexagonal structures are related by distortion in the bond angle. The bond-orientational order parameter for simulated pure cut-spheres in the monolayer side phase was 0.63.<sup>43</sup>

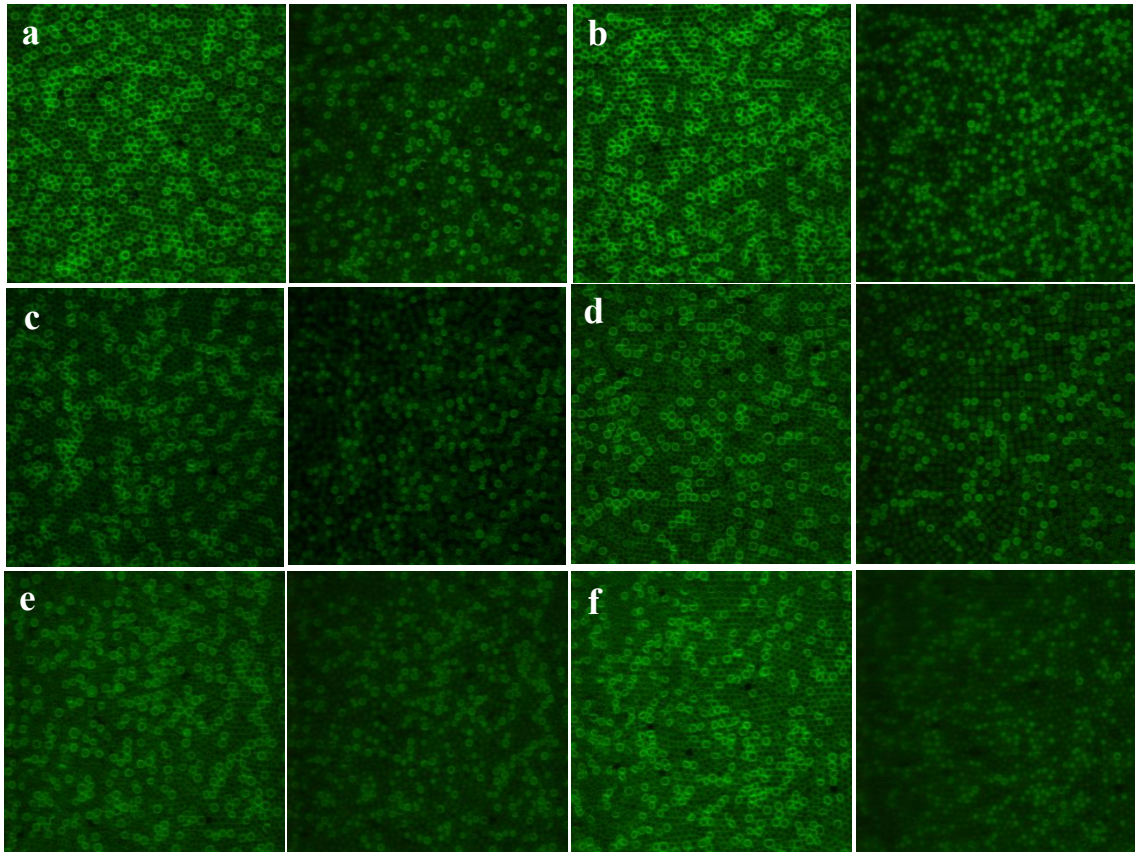


**Figure 4.8.** Confocal images for binary phases of spheres and cut-spheres with larger size mismatch. The structures observed with increasing gap height are a)  $1\Delta_r$  hexagonal monolayer b)  $1S_l$  hexagonal side monolayer c) 1B buckled state d)  $2\Box$  square bilayer e)  $2\Delta_r$  hexagonal bilayer f)  $2S_l$  hexagonal side bilayer

In order to explore the effect of size mismatch between the particle populations, confinement assembly was performed on the binary system with cut-sphere size of  $2\ \mu\text{m}$  (major axis) and  $1.5\ \mu\text{m}$  (minor axis) with coefficients of variation 8 % and 3 %, respectively. The spheres were  $1.65\ \mu\text{m}$  in diameter with a 3 % coefficient of variation. Table 4.2 provides a listing of the binary phases as a function of gap height.

**Table 4.2. Shape-Binary Phase Composition and Bond-Orientational Order Parameters**

Phase	Order Parameters		Spheres (%)	Cut-sphere in plane (%)	Cut-sphere out of plane (%)
	$\psi_6$	$\psi_4$			
1 $\Delta_r$	0.63	0.35	67	28	5
1S <sub>i</sub>	0.62	0.36	66	4	30
1B	-	-	77	1	22
2 $\square$	0.34	0.65	74	22	4
2 $\Delta_r$	0.57	0.39	71	24	5
2S <sub>i</sub>	0.65	0.35	74	6	20

The confocal images in Figure 7 show phase separation of the populations was present, as predicted by the Hume-Rothery rules for size mismatch in building blocks greater than 15 %. Moreover, the 1B phase was composed on spheres in a buckled arrangement and cut-spheres in a side state (Supplemental Video SV4). Vacancies and dislocations decorate the phases at greater number and in general, the bond-orientational order parameters (Table 2) are decreased due to the increased size mismatch (Figure 4.9). Comparing to the previous system (Table 1), the orientations of cut-spheres exhibited an 18 % increase in the in-plane oriented particles for the 2 $\square$  phase and a 27 % increase in the same for the 2 $\Delta_r$  phase. The out-of-plane cut-sphere orientation is restricted because the bilayer of cut-spheres with this orientation takes up significantly more height than the spheres.

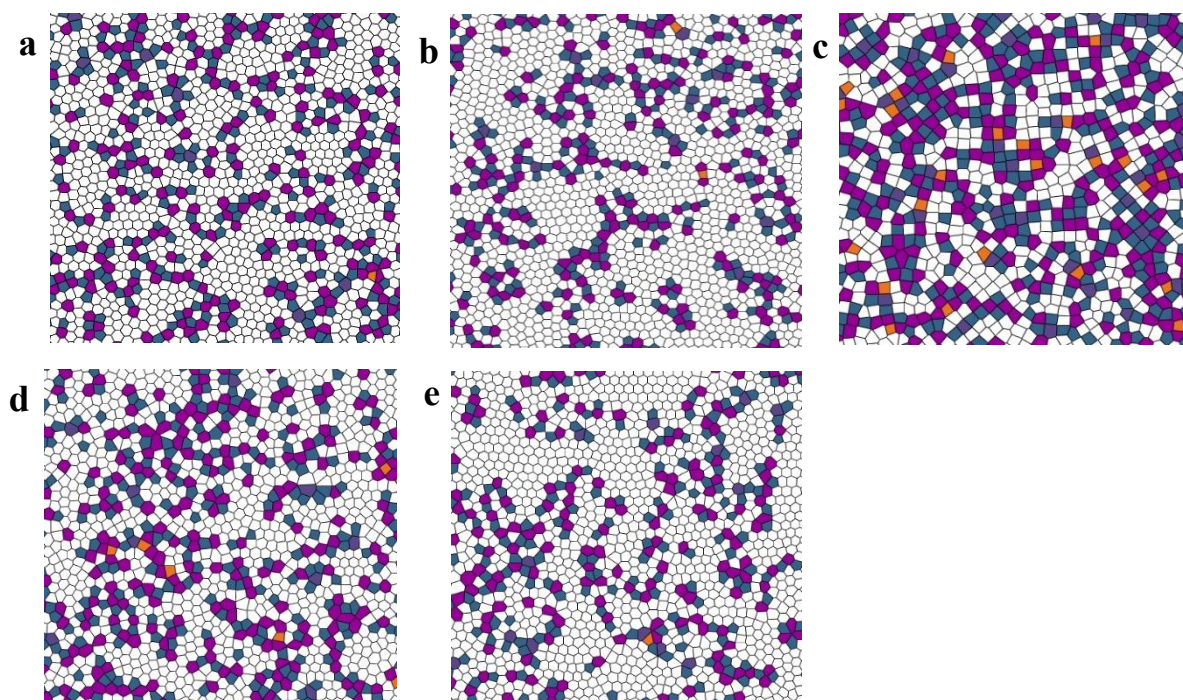


**Figure 4.9.** Voronoi constructions for shape-binary phases of spheres and cut-spheres with larger size mismatch a)  $1\Delta_r$ , hexagonal monolayer b)  $1S_r$ , hexagonal side monolayer c)  $2\square$  square bilayer e)  $2\Delta_r$ , hexagonal bilayer f)  $2S_r$ , hexagonal side bilayer. Color coding represents the number of nearest neighbor lobes as 4-orange, 5-blue, 6-white, 7-magenta,  $\geq 8$ -indigo.

## 4.5 Conclusion

Binary mixtures of spheres and cut-spheres are self-organized using a wedge-cell confinement method. The feature sizes and hollow morphology of the particles is designed to maximize lattice compatibility and reduce phase separation. The assembly is driven by entropic forces associated with hard particles confined between hard walls. When the lattice spacing of bulk crystalline structures is incommensurate with gaps imposed by the plate separations, particles form alternate arrangements. Eight distinct binary phases were observed between 1 and 2 integral layers as a function of gap height and

system density using laser scanning confocal microscopy,  $1\Delta_r \rightarrow 1S_I \rightarrow 1S_{II} \rightarrow 1B \rightarrow 2\Box \rightarrow 2\Delta_r \rightarrow 2S_I \rightarrow 2S_{II}$ . This progression is similar to that of pure cut-spheres with the added feature of now having substitutional disorder on the lattices. This study provides a colloidal analog for the isomorphous behavior in atomic systems as predicted by the Hume-Rothery rules. Specifically, the size mismatch between the shape populations is less than 15%, the particle interactions are similar, and spheres and cut spheres tile many of the same phases with gap height. For size mismatch greater than 15%, we found phase separation and decreased order metrics, as expected.

Other morphologies would be of interest for phase behavior studies of lattice-compatible particle mixtures, for example, cubes and rectangular prisms with 2:1 aspect ratio. Study of the photonic properties of the binary phases also presents an opportunity at the forefront of disordered photonics. In particular, photonic slab simulations which take into account the three-dimensional shape of the building blocks would be of interest for the square bilayer and side rotator phases. Slab simulations for the square bilayer phase of pure cut-spheres predict a complete photonic band gap with 10.2 % gap size.

## REFERENCES

1. A. B. Pawar and I. Kretzschmar, *Macromol. Rapid Commun*, 2010, **31**, 150-168.
2. Z. Zhang and S. C. Glotzer, *Nano Lett.*, 2004, **4**, 1407-1413.
3. S. H. Lee, and C. M. Liddell, *Small*, 2009, **5**, 1957-1962.
4. T. Ding, K. Song, K. Clays and C. H. Tung, *Adv. Mater.*, 2009, **21**, 1936-1940.
5. S. C. Glotzer, and M. J. Solomon, *Nat. Mater.*, 2007, **6**, 557-562.
6. U. Agarwal and F. A. Escobedo. *Nat. Mater.*, 2011, **10**, 230-235.
7. D. Dendukuri, T. A. Hatton and P. S. Doyle, *Langmuir*, 2007, **23**, 4669-4674.
8. S. Jiang, Q. Chen, M. Tripathy, E. Luijten, K. S. Schweizer and S. Granick, *Adv. Mater.*, 2010, **22**, 1060-1071.
9. S. Yoshimura and S. Hachisu, *Prog. Colloid Polym. Sci.*, 1983, **68**, 59-70.
10. P. Bartlett, R. H. Ottewill and P. N. Pusey, *Phys. Rev. Lett.*, 1992, **68**, 3801.
11. M. D. Eldridge, P. A. Madden and D. Frenkel, *Nature*, 1993, **365**, 35-37.
12. M. D. Eldridge, P. A. Madden, P. N. Pusey and P. Bartlett, *Mol. Phys.*, 1995, **84**, 395-420.
13. N. Hunt, R. Jardine and P. Bartlett, *Phys. Rev. E.*, 2000, **62**, 900.
14. M. E. Leunissen, C. G. Christova, A. P. Hynninen, C. P. Royall, A. I. Campbell, V. Roij and A. van. Blaaderen, *Nature*, 2005, **437**, 235-240.
15. A. Hynninen, C. G. Christova, R. Roij, A. van Blaaderen and M. Dijkstra, *Phys. Rev. Lett.*, 2006, **96**, 138308.
16. M. H. Kim, S. H. Im and O. O. Park, *Adv. Mater.*, 2005, **17**, 2501-2505.

17. K. P. Velikov, C. G. Christova, R. P. Dullens and A. van Blaaderen, *Science*, 2002, **296**, 106-109.
18. M. Khaldikar and F.A. Escobedo, *J. Chem. Phys.* 2012, **137**, 194907.
19. J. A. Millan, D. Ortiz, G. van Anders and S. C. Glotzer, *ACS nano*, 2014, **8**, 2918-2928.
20. W. Man, M. Megens, P. J. Steinhardt, and P. M. Chaikin, *Nature*, 2005, **436**, 993-996.
21. S. David, A. Chelnokov, and J. M. Lourtioz, *IEEE J. Quantum Electron.* 2001, **37**, 1427-1434.
22. D. Jovanovic', R. Gajic', and K. Hingerl, *Opt. Express*, 2008, **16**, 4048-4058.
23. S. Sacanna, W. T. M. Irvine, P. M. Chaikin and D. J. Pine. *Nature*, 2010, **464**, 575-578.
24. J. W. J. de Folter, P. Liu, L. Jiang, A. Kuijk, H. E. Bakker, A. Imhof, A. Van Blaaderen, J. Huang, W. K. Kegel, A. P. Philipse and A. V. Petukhov, *Part. Part. Syst. Charact.*, 2015, **32**, 313-320.
25. T. Paik and C. B. Murray, *Nano Lett.*, 2013, **13**, 2952-2956.
26. M. Florescu, S. Torquato, and P. J. Steinhardt, *Proc. Natl. Acad. Sci. U. S. A.* 2009, **106**, 20658.
27. W. Man, M. Florescu, K. Matsuyama, P. Yadak, S. Torquato, P. Steinhardt, and P. Chaikin, *Lasers Electro Optics CLEO Quan. Electron. Laser Sci. Conf. QELS 2010 Conf.* 2010, 1-2.
28. K. Edagawa, S. Kanoko, and M. Notomi, *Phys. Rev. Lett.*, 2008, **100**, 013901.
29. S. David, A. Chelnokov, and J. M. Lourtioz, *Opt. Lett.*, 2000, **25**, 1001-1003.

30. W. Man, M. Florescu, E. P. Williamson, Y. He, S. R. Hashemizad, B. Y. C. Leung, D. R. Liner, S. Torquato, P. M. Chaikin, and P. J. Steinhardt, *Proc. Natl. Acad. Sci.*, 2013, **110**, 15886-15891.
31. S. Tsitrin, Y. He, S. Hewatt, B. Leung, W. Man, M. Florescu, P. J. Steinhardt, S. Torquato, and P. Chaikin, in *Frontiers in Optics 2012/Laser Science XXVIII*, OSA Technical Digest (Optical Society of America, 2012), paper FTh3F.4.
32. A. David, T. Fujii, E. Matioli, R. Sharma, S. Nakamura, S. P. DenBaars, C. Weisbuch, and H. Benisty, *Appl. Phys. Lett.* 2006, **88**, 073510.
33. F. Caruso, R. A. Caruso and H. Möhwald, *Science*, 1998, **282**, 1111-1114.
34. K. Muangnapoh, C. Avendaño, F. A. Escobedo, and C. M. L. Watson, *Soft matter*, 2014, **10**, 9729-9738.
35. E. K. Riley and C. M. Liddell, *Langmuir*, 2010, **26**, 11648-11656
36. A. C. Stelson, C. Avendano, C. M. L. Watson, *J. Appl. Phys.*, 2016, **119**, 023110.
37. E. Y. K. Fung, K. Muangnapoh and C. M. L. Watson, *J. Mater. Chem.*, 2012, **22**, 10507-10513.
38. S. Naser, T. Palberg, C. Bechinger and P. Leiderer, *Optical Methods and Physics of Colloidal Dispersions*, 1997, 194-197.
39. Y. Han, Y. Shokef, A. M. Alsayed, P. Yunker, T. C. Lubensky and A. G. Yodh, *Nature*, 2008, **456**, 898-903.
40. A. Fortini and M. Dijkstra, *J. Phys.: Condens. Matter*, 2006, **18**, L371.
41. R. P. A. Dullens, M. C. D. Mourad, D. G. A. Aarts, J. P. Hoogenboom, W. K. Kegel, *Phys. Rev. Lett.*, 2006, **96**, 028304.

42. C. Avendano, C. M. L. Watson and F. A. Escobedo, *Soft Matter*, 2013, **9**, 9153-9166.